
A Laser Source for the Generation of Intense Attosecond Pulses and its First Applications

Hans Wolfgang Schweinberger



München 2014

A Laser Source for the Generation of Intense Attosecond Pulses and its First Applications

Hans Wolfgang Schweinberger

Dissertation
an der Fakultät für Physik
der Ludwig–Maximilians–Universität
München

angefertigt am
Max-Planck-Institut für Quantenoptik

vorgelegt von
Hans Wolfgang Schweinberger
aus München, Deutschland

München, den 11.08.2014

Erstgutachter: Prof. Dr. Ferenc Krausz

Zweitgutachter: Prof. Dr. Jörg Schreiber

Tag der mündlichen Prüfung: 23.10.2014

Contents

List of Figures	viii
1 Introduction	4
2 Fundamentals of Ultrashort Pulses and Attosecond Tech.	7
2.1 Ultrashort Pulses and Nonlinear Effects	8
2.2 Isolated Attosecond Pulses	11
2.3 Streaking Metrology	17
3 Laser Development	20
3.1 Description of a Common Laser Source for HHG	22
3.2 Design Considerations	24
3.3 Two-Stage Amplifier with Glass Compressor	24
3.3.1 Amplification	26
3.3.2 White Light Generation	30
3.3.3 Compression and CE-Phase Stabilization	37
3.3.4 Challenges of this Setup	45
3.4 Two-Stage Amplifier with Transmission Grating Compressor	50
3.4.1 Amplification & Compression	54
3.4.2 Spectral Broadening	55
3.4.3 Compression and Characterization	56
3.5 One-Stage Amplifier with Transmission Grating Compressor	57
3.6 Summary, Discussion and Further Development	59
4 First Applications	61
4.1 Experimental HHG	61
4.1.1 Results	64
4.1.2 Pulse Characterization by Attosecond Streaking	72

Contents

4.2	Giant Resonance of Xenon Probed by Broadband XUV-Pulses	76
4.2.1	Simulation of the Giant Resonance Response	76
4.2.2	Experimental Setup	78
4.3	Nonlinear Propagation in SiO ₂	84
5	Future Development	89
5.1	Intense sub-3 fs Pulses	89
5.2	Attosecond Experiments	91
6	Conclusion	93
	Bibliography	95
A	Setups	106
B	Glass Block Data	113
C	Dielectric Chirped Mirrors	119

List of Figures

2.1	Spectral Gating for Isolated Attosecond Pulses	16
2.2	Attosecond Streaking	19
3.1	System setup, negative dispersion	25
3.2	Grism and Glass Block setup	26
3.3	Beam profiles Booster	27
3.4	Spectral comparison of neg. and pos. dispersion setup	28
3.5	SH-FROG pulse characterization	30
3.6	Static pressure setup	32
3.7	Differentially pumped setup	35
3.8	Pressure dependent HCF output beam profiles	36
3.9	Carrier envelope phase	39
3.10	CEP in Oscillator	41
3.11	CEP measurement spectrum	42
3.12	CEP measurement after HCF	43
3.13	CEP measurement before HCF	44
3.14	Cooling issues	46
3.15	CVI mirrors	47
3.16	Tracking source for beam profile distortions I	48
3.17	Tracking source for beam profile distortions II	49
3.18	Transmission Grating	51
3.19	New components of the laser system	52
3.20	Beam-profiles each pass in 2nd amplifier stage	53
3.21	Phase feedback compresssion	54
3.22	Broadened spectra	56
3.23	Pulse characterization of one-stage amplifier	58
4.1	Metal XUV filters	63

List of Figures

4.2	Broadband XUV pulses	65
4.3	Helium High-Harmonics	66
4.4	HHG in Helium & Neon Comparison	67
4.5	HHG-flux	68
4.6	Ionization gating	70
4.7	Double XUV pulse streaking	73
4.8	HHG by chirped pulses	74
4.9	Shape-resonance and 130 eV mirror	78
4.10	Comparing reconstructions of neon and xenon	80
4.11	Measured photoelectron spectra in xenon without lens	81
4.12	Nonlinear propagation effects in SiO ₂ I	85
4.13	Nonlinear propagation effects in SiO ₂ II	86
4.14	Intensity dependent imaged laser beam profile	88
A.1	Femtopower & Grism	106
A.2	Schematic two-staged laser setup with transmission gratings	107
A.3	AS-2 beam-line setup for broadband XUV-pulses	108
A.4	AS-2 beam-line setup with SiO ₂ in the intermediate focus	109
A.5	Thales' setup of the second stage amplifier	110
A.6	New setup of the second stage amplifier	111
A.7	Crystal Holders of Second Stage	112
C.1	Two chirped mirror designs used	120

Zusammenfassung

Die beständige Entwicklung und Verbesserung der verfügbaren Laserquellen hat die Anzahl ihrer Anwendungen stetig wachsen lassen und darüber hinaus insbesondere Hochpräzisionsmessungen in vielen Bereichen dramatisch verbessert. Das Ziel dieser Doktorarbeit ist die Verbesserung der gängigsten Laserquelle zur Erzeugung von isolierten extrem-ultravioletten (XUV) Pulsen, welche im letzten Jahrzehnt das Studium von Elektronen-Dynamiken im sub-femtosekunden Bereich ($1 \text{ fs} = 10^{-15} \text{ s}$) ermöglicht hat und zu vielerlei Erkenntnissen der Elektronendynamik in Atomen, Molekülen und Festkörpern beigetragen hat.

Mittels der Verwendung einer zusätzlichen Verstärkerstufe, zu dem üblichen einstufigen Verstärkersystem mit gestreckten Laserpulsen, gelang es die auf weniger als 5 fs komprimierte Laserpulsenergie auf 1,5 mJ zu verdreifachen. Dafür wurden zwei unterschiedliche Konzepte für die Kompression der verstärkten Pulse miteinander verglichen. Mit dieser erhöhten Pulsenergie ist es möglich sowohl den Photonenfluss in den erzeugten, isolierten Attosekundenpulsen als auch deren Photonenenergie zu erhöhen. Betrieben bei vier Kilohertz Wiederholrate, erlaubt das Lasersystem die Durchführung integrativer Messung mit zwei-Zyklen-Laserpulsen mit deutlich höherer Geschwindigkeit als die meisten anderen Laserquellen in diesem Energiebereich.

Diese Laserpulse werden zur Erzeugung höherer Harmonischer eingesetzt und wurden mittels Attosekundenstreakingspektroskopie (Attosekunden-Schlierenspektroskopie) charakterisiert wobei zugleich die hervorragende Stabilität und die Qualität der XUV-pulse nachgewiesen wurde.

Die so erzeugten XUV-Pulse wurden zur Durchführung erster Experimente herangezogen, zum einen zur breitbandigen, zeitlichen Charakterisierung der Photoemission der "Riesenresonanz" der Xenon-4d Schale bei 100 eV und zum anderen bei der Untersuchung der induzierten nichtlinearen Propagation in Quarzglas. Deren Einfluss auf die elektrischen Wellenform der ultrakurzen Laserpulse im sichtbaren, nah-

List of Figures

infraroten Spektralbereich wurde mittels Attosekunden-Streaking charakterisiert. Die höheren Pulsenergien des Lasersystems werden sich als besonders nützlich erweisen sobald weitere nichtlineare Effekte Teil des Anregungs-Abfrage-Aufbaus sind, wie z.B. bei der Erzeugung von ultrakurzen UV-Pulsen zur Anregung und der XUV-Pulse zur zeitlichen Abfrage, da die Intensität beider Pulse mit der Pulsenergie des fundamentalen Pulses ansteigt.

Abstract

The continuous development and improvement of laser sources has steadily increased the number of applications and pushed the limit of high precision measurements in various fields. The goal of the work presented in this thesis is to improve the spectrally broadened Ti:sapphire laser system used for isolated extreme ultraviolet (XUV) pulse generation, which has, in the last decade, allowed the study of electron dynamics on a sub-femtosecond ($1 \text{ fs} = 10^{-15} \text{ s}$) level and delivered new insights into ultrafast dynamics of electrons in atoms, molecules and solids.

By adding a second stage amplifier to the commonly used one-stage chirped pulse amplification laser system the compressed output power of a sub-5 fs laser system has been tripled to 1.5 mJ. A crucial part for achieving this result is the comparison of two different efficient compressor setups in order to optimize the compression. With these higher pulse energies, it is possible to increase the generated photon flux in an isolated attosecond (10^{-18} s) pulse and to push the XUV photon energy higher. Run at 4 kHz repetition rate, integrative measurements with sub-2 cycle laser pulses can be conducted much faster than with most laser sources in this energy range.

The resulting pulses are used for high-harmonic generation (HHG) and characterized via attosecond streaking, demonstrating excellent stability and quality of the whole laser system.

First experiments with these pulses were conducted by probing the temporal behavior of the photo-emission of the giant resonance of 4d electrons in xenon with broadband XUV-pulses at 100 eV and inducing and measuring the nonlinear propagation in fused silica at high intensities via its effect on the waveform of the ultra-short visible-near-infrared pulse measured by means of attosecond streaking.

The higher pulse energy of the driving laser field will also prove to be very useful as soon as nonlinear effects besides HHG contribute to the pump and probe setup e.g. an ultrashort UV-pulse is used to pump electron dynamics which are subsequently probed with high temporal resolution by the XUV-pulse.

Chapter 1

Introduction

With the invention of attosecond science ($1 \text{ as} = 10^{-18} \text{ s}$) about one decade ago it became possible to put the subtleties of light-matter interaction under test in an unprecedented way. Several experimental studies [1, 2, 3, 4] provided experimental observations that allowed to benchmark high-level theories and triggered the development of novel theoretical frameworks to model the detailed characteristics of the system under scrutiny after its interaction with light. Of particular interest for these studies has been the photoelectric effect introduced by Einstein in 1905 describing the release of an initially bound electron into the ionization continuum upon the absorption of one high-energetic or several low-energetic photons and the electronic response of atomic [5], molecular [6] and solid systems [7] to strong electromagnetic fields.

Many aspects of the nonlinear response of matter to intense light are rooted in the collective interplay of several electrons bound in the ground state of the system giving rise to a wealth of phenomena including excitation resonances in atoms, dissociation pathways in molecules or characteristic decay channels governed by intrinsic electronic correlations e.g. observed in the Auger decay mechanism. Due to the lack of direct access to many of the experimental signatures of these electronic correlations theory described them generally in single-active particle approximations and only nowadays the toolbox of attosecond technology allows us to explore the boundaries of these treatments. However, due to the notoriously low photon flux and restricted spectral range of attosecond experiments, investigations have to be carried out at sample systems that are carefully selected to provide sufficient signal levels. To overcome these limitations and allow for attosecond time resolved studies in hitherto inaccessible systems, regarding photon flux and spectral range,

a source for isolated attosecond pulses with enhanced flux has been developed and a set of experiments proves its capability to grasp multi-electron dynamics in gases and solids. A first experiment investigates the origin of the xenon giant resonance whose origin remained disputed in the past due to the lack of experimental access to the phase of the outgoing electronic wave-packet [8]. A second experiment is introduced targeted at the exploration of the time resolved response of the nonlinear interaction of transparent medium with ultrastrong few-cycle laser pulses.

Outline of the Thesis

After this brief introduction, chapter 2 provides a short deduction of the self-action effects of self-focusing and self-phase modulation which are important when working with strong ultrashort pulses followed by an introduction to the generation of isolated attosecond extreme ultraviolet (XUV) pulses and their characterization via attosecond streaking. Chapter 3 presents an overview of a widely-used laser system for generating high harmonics and isolated attosecond pulses. This system is used as a base for the two different two-stage laser setups described thereafter to enhance the pulse energy. First, a negatively chirped setup with a very efficient glass-compressor is discussed. After presenting the concept and the realized performance, the system is analyzed in view of possible further improvements and is followed by the second setup featuring a transmission-grating compressor and glass as the stretcher. The results achieved with the second setup are followed up by a description of the one-stage laser system utilizing the same compression scheme. The chapter finishes with a comparison of the two systems and an outlook of the next steps of this developed laser system.

To demonstrate the capabilities of the laser system, first experiments with attosecond pulses were conducted and are described in chapter 4. The generation and characterization of high harmonics with the new laser system and a comparison of the HHG-spectra of helium and neon are presented. Next, broadband isolated attosecond pulses generated in neon were used to study the photo-emission of xenon 4d. Subsequently, attosecond streaking is used to measure the changes of an ultrashort pulse induced by its propagation through fused silica just below damage threshold. Some possible means to improve the laser system even further and attosecond experiments facilitated by it will be presented in chapter 5 and a summary of the results will be given in the final chapter 6.

Author's Publications Directly Related to the Thesis

- **W. Schweinberger**, A. Sommer, E. Bothschafter, J. Li, F. Krausz, R. Kienberger, and M. Schultze. *Waveform-controlled near-single-cycle milli-joule laser pulses generate sub-10 nm extreme ultraviolet continua*. Optics Letters, vol. **37**, no. 17, pp. 3373–3575, Sep 2012

Further Publications of the Author

- M. Schultze, E. M. Bothschafter, A. Sommer, S. Holzner, **W. Schweinberger**, M. Fieß, M. Hofstetter, R. Kienberger, V. Apalkov, V. S. Yakovlev, M. I. Stockman and F. Krausz. *Controlling dielectrics with the electric field of light*. Nature, vol. **493**, no. 7430, pp. 75–78, 2013
- F. Reiter, U. Graf, M. Schultze, **W. Schweinberger**, H. Schröder, N. Karpowicz, A. M. Azzeer, R. Kienberger, F. Krausz, and E. Goulielmakis. *Generation of sub-3 fs pulses in the deep ultraviolet*. Optics Letters, vol. **35**, no. 13, pp. 2248–2250, 2010
- F. Reiter, U. Graf, E. E. Serebrynnikov, **W. Schweinberger**, M. Fieß, A. M. Azzeer, R. Kienberger, F. Krausz, A. M. Zheltikov, and E. Goulielmakis. *Route to Attosecond Nonlinear Spectroscopy*. Physical Review Letters, vol. **105**, pp. 243902, 2010
- W. Helml, A. R. Maier, **W. Schweinberger**, I. Grguraš, P. Radcliffe, G. Doumy, C. Roedig, J. Gagnon, M. Messerschmidt, S. Schorb, C. Boestedt, F. Grüner, L. F. DiMauro, D. Cubaynes, J. D. Bozek, Th. Tschentscher, J. T. Costello and M. Meyer, R. Coffee, S. Düsterer, and R. Kienberger. *Measuring the temporal structure of few-femtosecond FEL-X-ray pulses directly in the time domain*. accepted Nat. Phot.

Chapter 2

Fundamentals of Ultrashort Pulses and Attosecond Technology

After the realization of the first optical sources using light amplification by stimulated emission of radiation (LASER) in 1960 by Maiman [9] the development of mode-locked lasers [10] led to ever shorter pulses and higher peak intensities. Using strong, ultrashort pulses from a titanium doped sapphire crystal to generate pulses short enough to observe the fastest dynamics studied in a time-resolved manner so far is part of this work.

In this chapter basic concepts that are important for the observations described later will be presented. Starting with a short review of field induced polarization in a medium, the self-action nonlinear effects of self-focusing and self-phase modulation (SPM) will be described. Both are important to generate sub-5 fs at the millijoule level. The basic concepts of high-harmonic generation (HHG) and isolated attosecond pulse generation will follow and a description of the most common method to characterize these short pulses as well as a decent tool to study the photo-emission process itself is given in the form of attosecond streaking spectroscopy.

2.1 Ultrashort Pulses and Nonlinear Effects

For the mathematical description of light waves we start from Maxwell's Equations

$$\nabla \cdot \mathbf{D} = \rho, \quad (2.1)$$

$$\nabla \cdot \mathbf{B} = 0, \quad (2.2)$$

$$\nabla \times \mathbf{E} = -\frac{\partial \mathbf{B}}{\partial t}, \quad (2.3)$$

$$\nabla \times \mathbf{H} = \frac{\partial \mathbf{D}}{\partial t} + \mathbf{J} \quad (2.4)$$

and derive the optical wave equation by using the curl of Eq. (2.3) without any free charge or currents $\rho = 0$ and $\mathbf{J} = 0$. Assuming the medium is nonmagnetic and using the other Maxwell's equations the optical wave equation is given by

$$\nabla \times \nabla \times \mathbf{E} = -\frac{1}{c^2} \frac{\partial^2 \mathbf{E}}{\partial t^2} - \mu_0 \frac{\partial^2 \mathbf{P}}{\partial t^2}, \quad (2.5)$$

where \mathbf{P} is the induced electric polarization of the material. This polarization can be split into a linear and a nonlinear part.

$$\mathbf{P}(\mathbf{r}, t) = \mathbf{P}_L(\mathbf{r}, t) + \mathbf{P}_{NL}(\mathbf{r}, t) \quad (2.6)$$

Assuming the response of the material to be instantaneous the nonlinear polarization can be expanded in a power series. All even order coefficients are zero as long as the material has inversion symmetry. By neglecting all but the leading term the nonlinear polarization in gas can be written as

$$\mathbf{P}_{NL}(\mathbf{r}, t) = \varepsilon_0 \chi^{(3)} : \mathbf{E}(\mathbf{r}, t) \mathbf{E}(\mathbf{r}, t) \mathbf{E}(\mathbf{r}, t), \quad (2.7)$$

where ε_0 is the vacuum permittivity and $\chi^{(3)}$ is the third order susceptibility. With this third order nonlinearity the refractive index becomes intensity dependent with

$$\tilde{n} = n + n_2 |E|^2 = n + n_2 I, \quad (2.8)$$

for an isotropic medium where the nonlinear refractive index n_2 is given by

$$n_2 = \frac{3}{4n} \text{Re}(\chi^{(3)}). \quad (2.9)$$

2.1. Ultrashort Pulses and Nonlinear Effects

This nonlinear behavior of the refractive index acts on the beam like a lens. For $n_2 > 0$ and a Gaussian laser beam with the power

$$P_{cr} = \frac{\pi(0.61)^2 \lambda_0^2}{8n_0 n_2} \quad (2.10)$$

the laser beam converges to a small size and can propagate without diverging granted there are no losses [11]. At this power the self-focusing effect is exactly as strong as the divergence of the beam without the effect. This equilibrium state, also known as filamentation plays an important role in the white light generation in a gas filled hollow core fiber and in most cases when the laser is able to ionize atoms.

So far the medium has been lossless and dispersionless. By introducing the frequency dependent complex dielectric tensor $\epsilon^{(1)}$ and the relationship

$$\mathbf{D}_n^{(1)}(\mathbf{r}) = \epsilon_0 \epsilon^{(1)}(\omega_n) \cdot \mathbf{E}_n(\mathbf{r}) \quad (2.11)$$

for the optical wave equation (2.5) and with the derivative relation

$$\nabla \times \nabla \times \mathbf{E} = \nabla(\nabla \cdot \mathbf{E}) - \nabla^2 \mathbf{E} \quad (2.12)$$

in combination with the slowly varying amplitude approximation which allows to neglect the first term on the right side the Nonlinear Schrödinger Equation becomes

$$\nabla^2 \mathbf{E}_n(\mathbf{r}) + \frac{\omega_n^2}{c^2} \epsilon^{(1)}(\omega_n) \cdot \mathbf{E}_n = -\frac{\omega_n^2}{\epsilon_0 c^2} \mathbf{P}_n^{NL}(\mathbf{r}) \quad (2.13)$$

where c is speed of light in vacuum.

The time dependent electric field of a pulse can be written as

$$E(t) = A(t) e^{i(\omega_0 t + \Phi(t) + \varphi)} \quad (2.14)$$

where $A(t)$ is the slowly varying field envelope and ω_0 is the central or carrier frequency of the electric field. The relative position of the fast oscillating field and the envelope is given by φ , the carrier-envelope phase (CEP). Measuring and controlling the CEP becomes increasingly important with shorter pulses. With three-cycle pulses or less the slowly varying amplitude approximation becomes questionable [12] and different CEP values cause different physical results as shown in Fig. 2.1. The means to how the CEP can be measured and controlled will be described later in Sec. 3.3.3.

The time dependent phase $\Phi(t)$ in Eq. (2.14) can also be regarded as a time dependent frequency shift of the fast oscillating field. The instantaneous frequency is given by

$$\omega(t) = \omega_0 + \frac{d\Phi(t)}{dt} = \omega_0 + \dot{\Phi}(t) \quad (2.15)$$

and $\Phi(t)$ is usually expressed as a power series

$$\Phi(t) = \sum_{j=0}^{\infty} \beta_j t^{j+1}. \quad (2.16)$$

This change in instantaneous frequency is also referred to as chirp of the pulse. While β_0 corresponds to a frequency up or down shift the next terms are associated with linear and quadratic chirp according to their time dependent change of the instantaneous frequency of the pulse.

Self-Phase Modulation

The intensity dependent change of the refractive index given by Eq. 2.8 causes also a chirp of the pulse. Considering the pulse written as

$$E(z, t) = A(z, t)e^{i(k_0 z - \omega_0 t)} + c.c. \quad (2.17)$$

propagating in z-direction defined by the wavenumber k_0 in said direction. The time dependent intensity is then given by

$$I(t) = 2n_0 \varepsilon_0 c |A(z, t)|^2. \quad (2.18)$$

Assuming a thin nonlinear medium, and thus neglecting other effects like dispersion, the propagating pulse will accumulate a nonlinear phase given by

$$\Phi_{nl}(t) = -n_2 I(t) \omega_0 L / c, \quad (2.19)$$

where L is the length of the medium. Similar to Eq. 2.15 this phase change corresponds to a change of the instantaneous frequency

$$\omega(t) = \omega_0 + \delta\omega(t) = \omega_0 + \frac{d}{dt} \Phi_{nl}. \quad (2.20)$$

While propagating through the nonlinear medium the intensity envelope of the pulse didn't change but its spectrum did. This effect is called self-phase modulation (SPM). The newly, by SPM, generated frequencies are shifted to lower frequencies at the front and to higher frequencies at the trailing edge of the pulse as long as n_2 is positive which is usually the case. This effect is used to broaden the spectrum of the pulse resulting in a spectrum which can support even shorter pulses which is the main contribution to white light generation (Sec. 3.3.2) used to generate millijoule two-cycle pulses with the laser system built and used in this thesis.

2.2 Isolated Attosecond Pulses

Most of the efforts to develop a more powerful laser source in the context of this work aims at producing more intense isolated attosecond pulses and consequently expanding the available XUV photon-energy range to higher energies. Thus an introduction to the generation of isolated attosecond pulses will be given next starting with the generation process of XUV photons.

High-Harmonic Generation

In general, high-harmonic generation (HHG) means that the laser energy is converted to much higher frequencies, beyond the scope of perturbative processes like second harmonic generation or wave mixing in general described by a nonlinear susceptibility χ . Also HHG is fundamentally different, and has been shown in gases and in high density plasmas generated from solids. HHG with solids requires relativistic intensities (10^{18} W/cm² and more) and although the scaling behavior is quite promising, using this source for experiments especially time resolved ones needs further development [13].

Gas high-harmonics on the other hand have been used successfully for time resolved measurements over a decade now [1]. Typical applications of these harmonics are attosecond streaking of atomic levels [5, 7], high-harmonic spectroscopy [14, 15] and transient absorption spectroscopy [16]. With the improvement of the driving laser sources more and more experiments become feasible. Increased high-harmonic flux and access to higher photon energies are the main goals of this development. For a better understanding, a description of the theoretical basics of HHG in gases will be presented next.

Theory of HHG

High-harmonic generation is the result of strong field laser interaction with atoms. To fully describe this process solving the Schrödinger equation of this system would be necessary, but a quasi-static semi-classical approach introduced by Corkum [17] explains the general features to very good agreement.

In the so-called three-step model the process is divided into laser field driven tunnel ionization, acceleration of the free electron in the electric field and recombination with the parent ion emitting the kinetic energy as high harmonic radiation.

Laser Field Ionization

The first step of HHG is ionization. To ionize an atom or molecule the ionization potential I_p has to be overcome. Typical values are from a few electron volts (eV) up to 24.6 eV for Helium. The photon energy is typically much lower around 1-2 eV for visible to near infrared lasers. In order to ionize an atom with ionization potential I_p n photons are needed $n \geq I_p/(\hbar\omega)$. This multi-photon ionization (MPI) is described best by perturbation theory of n -th order. For these lasers ionization starts at intensities around 10^{12} W/cm² and the ionization rate is $\Gamma \propto I^n$. For higher intensities the probability for photon absorption greater n increases which allows starting kinetic energies for the electrons higher than the photon energy. In fact, for a narrow band laser the kinetic energy spectrum of the electrons consists of peaks spaced by the photon energy. (This so-called above threshold ionization; ATI e.g. forms the noise background for attosecond streaking.) For broadband or even octave spanning laser spectra the kinetic energy of ATI electrons forms a continuum. If the intensity is increased further until the electric field of the laser field becomes similar in strength to the binding potential of the atoms the ionization mechanism changes. In the superposition of atomic and laser potential the electron is not strictly bound anymore but can tunnel through the potential barrier. At even higher intensities the potential barrier is completely suppressed by the electric field of the laser.

To estimate which mechanism is dominant Keldysh [18] introduced his adiabaticity parameter γ fifty years ago.

$$\gamma = \frac{\omega_L \sqrt{2m_e I_p}}{eE_0} = \sqrt{\frac{I_p}{2U_p}}$$

Here ω_L is the angular laser frequency, m_e the electron mass and e its charge, E_0 is the amplitude of the continuous laser wave or for pulses the peak electric field and U_p is the ponderomotive energy, defined by the cycle-averaged kinetic energy of a free electron in the laser field. For $\gamma \gg 1$ MPI dominates and for $\gamma \ll 1$ tunnel-ionization is the dominating process. For lasers in the visible or near-infrared spectral range $\gamma \ll 1$ leads to very high ionization rates. The most common model to calculate the ionization rate for such strong fields was derived by Ammosov, Delone and Krainov (ADK-theory) [19]

$$\Gamma \propto \exp\left(-\frac{4\sqrt{2m_e}I_p^3}{3\hbar cE_0}\right).$$

Given that the 'tunneling time' is shorter than the half laser period, meaning the statistical distribution of the tunneled electrons is confined to a time shorter than the half laser period, the theory seems to be in good agreement with experiments. Direct tunnel-ionization is usually strongly temporally confined to the peaks of an oscillating electric field.

For $\gamma \sim 1$ and especially for short laser pulses Yudin and Ivanov [20] use a more appropriate formalism as they include the varying intensity envelope of the electric field.

For high-harmonic generation electron wave packets generated via tunnel ionization are necessary but too high intensities cause too much ionization which impairs the beam propagation and phase matching which in return decreases the overall efficiency.

High-Harmonic Radiation

After an electron tunneled through the potential barrier it has no kinetic energy, but it is accelerated by the present electric field of the laser. Assuming a linearly polarized laser field and as tunneling occurs most likely close to the peaks of an electric field oscillation the electron is accelerated for a quarter period away from the ion and the next half-cycle brings it back to its starting position but with a kinetic energy which depends on the exact time of the tunneling. According to Corkum [17] the highest kinetic energy is $3.17 U_p$. When the electron returns to its parent ion it can recombine and emit an XUV photon whose energy is given by the kinetic energy of the electron and the binding energy of the atom. The highest

possible energy is given by

$$E_{cut-off} = 3.17 U_p + I_p, \quad U_p = \frac{e^2 E_0^2}{4m_e \omega_L^2}. \quad (2.21)$$

With the relation $I = \varepsilon_0 c E_0^2 / 2$ for intensity and electric field strength and an intensity of 10^{15} W/cm² $U_p = 52.4$ eV. U_p is proportional to the focus intensity and scales quadratic with the central laser wavelength. Recently a 4 μ m laser at high intensities was used to generate high-harmonic spectrum up to 1.6 keV which corresponds to ~ 5000 th harmonic [21]. Unfortunately the recombination cross-section per atom decreases rapidly with the laser wavelength $\sim \lambda_l^{-5.5}$ [22, 23]. Multiple recombinations of the same half-cycle add up coherently and form a very short XUV pulse. However high harmonics are generated every half-cycle of the laser field (peaks in the electric field) generating an XUV pulse train with half laser period distance and thus form a modulated spectrum with a modulation length of $2\hbar\omega_L$ with the peaks at the odd harmonics of ω_L . For the highest photon energies which are emitted from the strongest half-cycle no interference occurs and the spectrum is smooth before the cutoff. To generate an isolated attosecond pulse this can be used by spectrally filtering this highest energy part leaving only one pulse of the attosecond pulse train. Obviously the energy bandwidth of the isolated pulse increases with shorter laser pulses as the ratio of neighboring electric field half-cycles increases.

The process is not very efficient. The biggest factor is the recombination cross section which decreases for longer trajectories and thus longer wavelengths and higher photon energies. Typical values for 800 nm are of the order 10^{-6} . Considering that most of the time only a small bandwidth of the highest photon energies of the spectrum is used decreases the the usable signal by two additional orders of magnitude. This scaling in photon flux is the main reason to pursue HHG in solids as it scales much better especially towards higher photon energies [13, 24, 25] but as a stable source for experiments further development is still necessary [26].

Spectral Isolation

The generation of XUV high-harmonics takes place every half-cycle of the laser if the driving laser pulse is linearly polarized and strong enough to ionize electrons. The XUV photon energy of each XUV pulse depends on the acquired kinetic energy of the electrons and thus on the intensity of the laser. So an intense short laser pulse generates a series of spectrally diverse XUV pulses. Because of their different spectra the pulse with the highest photon energies can be selected spectrally by blocking all lower energetic components. The bandwidth which is occupied by the most energetic half-cycle depends strongly on the CE-phase. In Fig. 2.1 the generated XUV pulses are shown for three different cases. In a) a cosine pulse provides the highest contrast between the strongest half-cycle and its neighbors. The electric field of the 3.6 fs pulse is shown with the XUV attosecond bursts demonstrating their different energies and pulse durations. To the right, a measured XUV spectrum using a zirconium filter which only transmits above 70 eV shows a selected spectral range above 70 eV. The spectrum is slightly modulated due to the residual contribution of the other half cycles. In b) the same pulse with different CE-phase is used to generate HHs. For the sine pulse two XUV pulses cover the same energy resulting in strong modulation of the XUV spectrum. For longer pulse duration as e.g. in c) with 4.5 fs the two XUV pulses have even less differences in their ionization step which increases the contrast of the modulation. For a longer cosine pulse the unmodulated part of the spectrum becomes smaller. So in order to get an isolated attosecond pulse only a) provides the right conditions because of its CE-phase. According to the measured spectrum in a) and in order to truly isolate one XUV pulse we would have to pick a photon energy of 95 eV or more, but a weak side pulse can be tolerated in some measurements.

For short broadband XUV pulses using a suitable metal filter provides the broadest bandwidth, for longer pulses usually a dielectric multilayer mirror is used which allows the selection of a specific photon energy with a few eV bandwidth. To eliminate the NIR laser the mirror is still used in combination with a metal filter which reflects the laser light.

Regarding the strong CE-phase dependence on the generated spectra or the corresponding attosecond pulse trains shown in Fig. 2.1 it is also clear why it is crucial to stabilize the CE-phase of the driving laser to ensure reproducible XUV pulse generation with each laser pulse. For more details about the experimental implementation see Sec. 3.3.3.

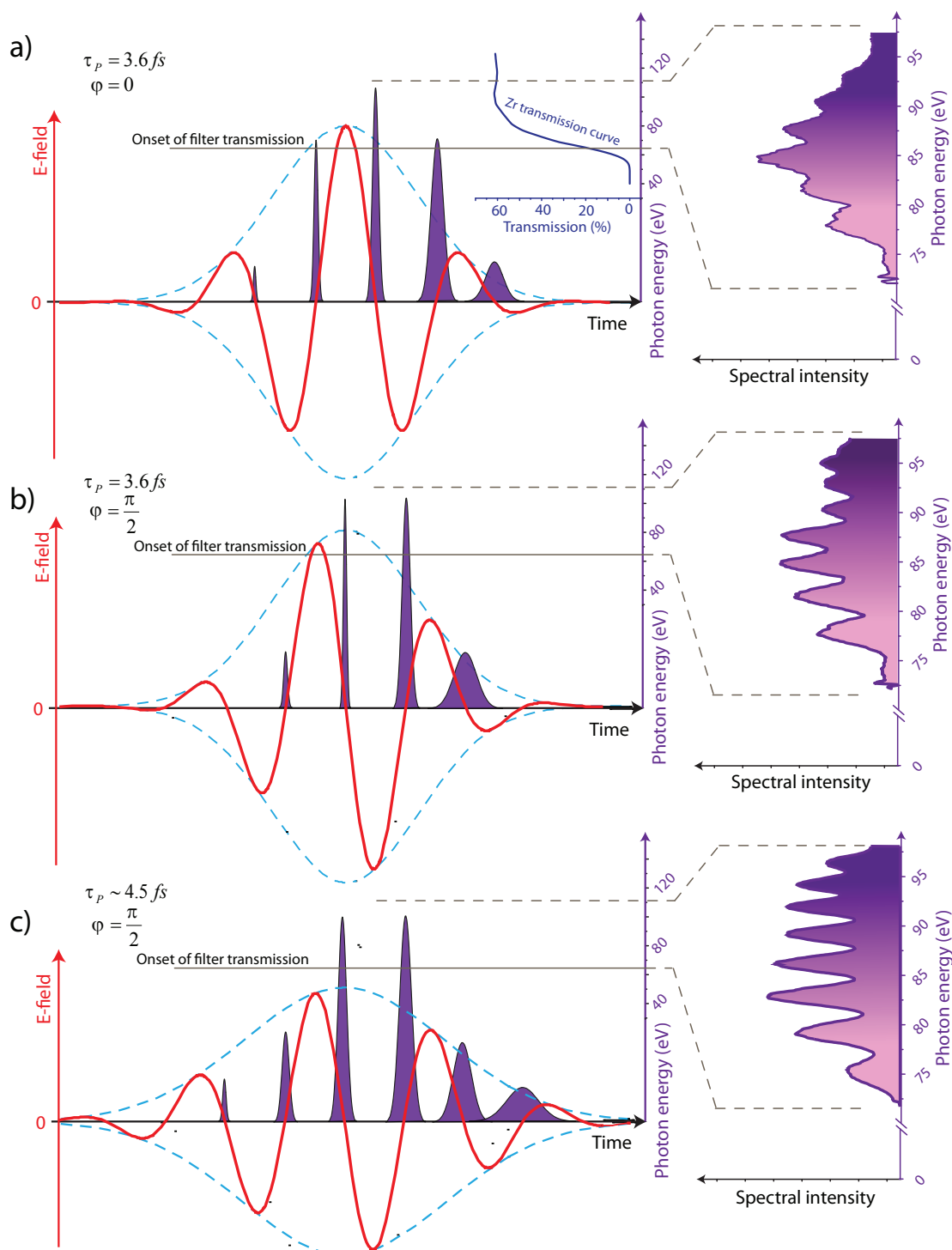


Figure 2.1: The figure demonstrates the CEP dependence of the generated HHs and the generation of an isolated attosecond pulse by spectral filtering the highest energetic XUV pulse in a) while b) and c) can only provide double pulses separated by a half-cycle of the laser field. The figure is taken with permission from [27].

2.3 Streaking Metrology

The next step after generating short XUV pulses is to measure and characterize them. For attosecond pulses in the XUV the usual methods used for laser pulses don't work. One way to characterize the pulses is to cross-correlate the photo-emission of the XUV with the driving laser field which results in a delay dependent spectral trace which can be used to reconstruct both pulses. The method explained here is called attosecond streaking.

The XUV pulse is focused into a gas target where it ionizes the atoms. In our case we usually use neon as the target gas. The ionized electrons inherit the characteristics of the pulse regarding energy, pulse duration and even chirp with the exception that the kinetic energy is reduced by the binding energy of the original electron level. For neon-2p this is 21.6 eV. The kinetic energy of the electrons is determined by measuring their time-of-flight (ToF) from the gas ionization in the gas target to a micro-channel-plate detector (MCP) where each electron is amplified and its time of arrival measured. The kinetic energy is given by

$$E_{kin} = \frac{m_e l^2}{2(t - t_0)^2} \quad (2.22)$$

where m_e is the electron mass, l the distance from the target to the detector, t the arrival time and t_0 the time of the ionization.

So far we are only able to measure the electron spectrum and therefore the XUV spectrum of the pulse this way, but by overlapping the XUV focus with the laser and by scanning their relative delay much more information can be extracted. Consider that the XUV pulse generates the photo-electrons during the presence of the linearly polarized laser field. The electrons will not only wiggle but can acquire a net momentum gain in the field direction depending on which time exactly the electron is freed. The momentum gain is proportional to the vector potential $A(t)$ of the electric field

$$E(t) = -\frac{\partial A}{\partial t}. \quad (2.23)$$

For streaking we only consider the electrons emitted perpendicular to the laser propagation in the plane of the electric field which is exactly how the ToF detector is set up. Fig. 2.2 shows two extreme cases. The first one shows the maximum momentum change when the electron is released at a zero crossing of the electric field of the laser field. Depending on the half-cycle the momentum is up or down shifted. In this

Chapter 2. Fundamentals of Ultrashort Pulses and Attosecond Tech.

case the momentum is increased. Note that because the XUV pulse and thus the electron wave-packet is not a delta-function the measured electron spectrum is also broadened compared to the electron spectrum without the laser field. The second part of the figure shows the case when the electron is released at the maximum of the electric field. Here no net momentum is gained, but the measured spectrum is broadened. And because it is the highest gradient of the vector potential the spectral broadening of the electrons is strongest at this release time of a laser cycle. The momentum of the electrons is recorded delay dependent and has the vector potential of the laser field imprinted onto it.

So far we assumed an unchirped XUV pulse. For a chirped pulse the behavior becomes more interesting. The former uniform broadening caused by different release times can now enhance or counteract the XUV chirp which is imprinted onto the electron wave packet. Consider an XUV pulse which releases higher energy electrons at lower times of t (negatively chirped) and the vector potential of the laser field acting similar to the second part of Fig. 2.2 then the different spectral components see a different net momentum gain such that the electrons end up with a reduced energy spread because the higher energetic electrons are decelerated and the lower ones are accelerated. A half-cycle earlier or later it is the opposite which leads to a higher energy spread.

So we can conclude that attosecond streaking is sensitive not only to the XUV spectrum, but also to its phase which allows us to fully characterize the XUV pulse. And as we obviously measure the vector potential of the laser pulse it can be characterized completely as well. A delay scan of photo-electron spectra (spectrogram) of a chirped attosecond pulse and its retrieval can be found in Fig. 4.2 on page 65.

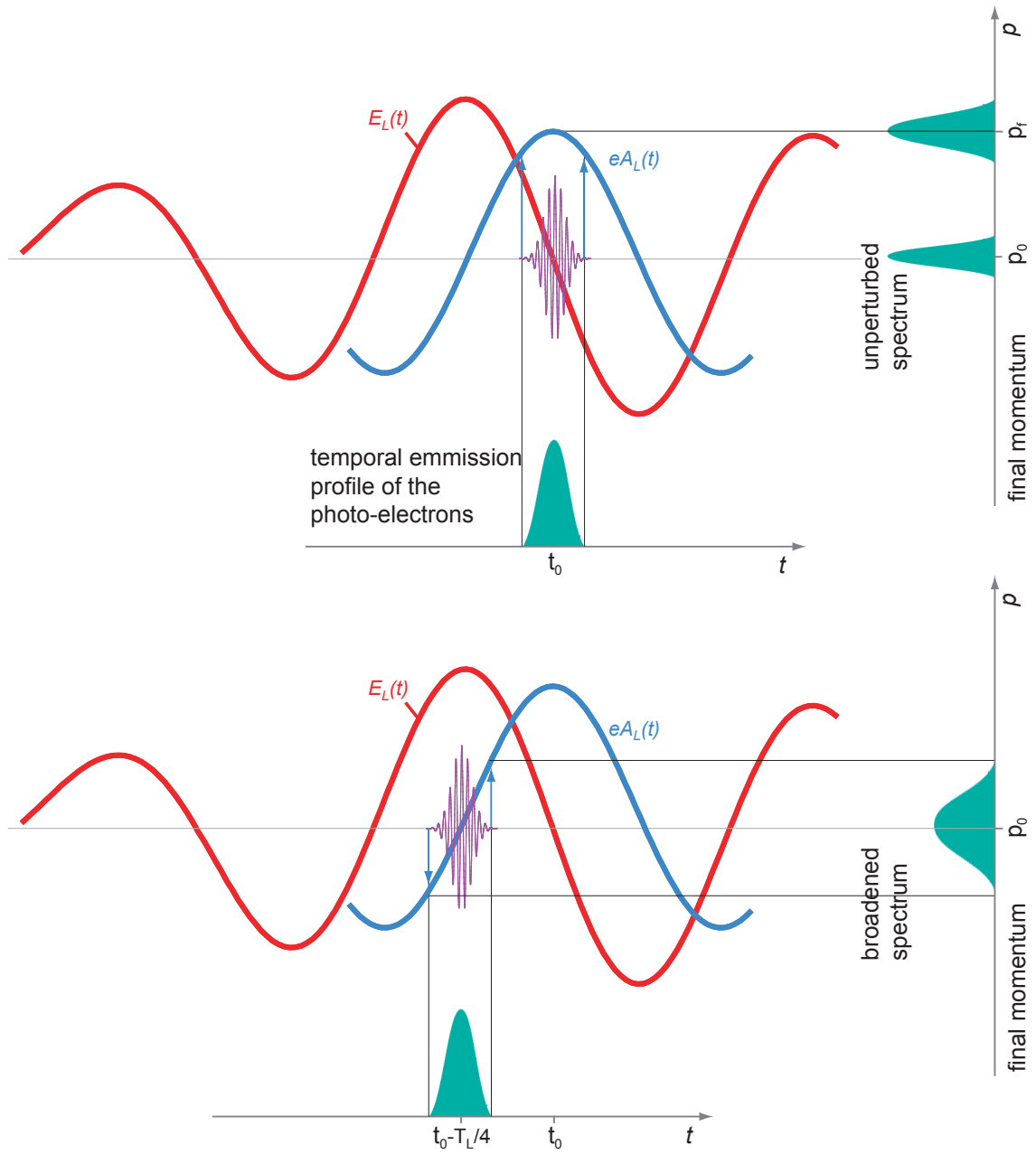


Figure 2.2: Delay dependent momentum shift of XUV photo-electrons: The momentum shift is proportional to the vector potential at the time the electron becomes free. This figure was provided by Dr. Schultze [28].

Chapter 3

Laser Development

Since the discovery and realization of the laser [9, 29] the progress in its technology and development has been remarkable. While continuous wave lasers have had a great impact on their own, mode-locked lasers [10] with nanosecond pulses permitted to achieve higher intensities which opened up the field of nonlinear optics. Since then, the peak intensity of laser systems covering various spectral ranges has been steadily improved, by decreasing the pulse duration to picoseconds [30] and later femtoseconds and by increasing the pulse energy by applying schemes like chirped pulse amplification (CPA) [31], which permits higher pulse energies in the gain medium. After a long period of dominance by liquid dye-lasers, diode pumped Ti:sapphire lasers became the primary laser source for high intensity lasers. Solid-state lasers are more robust and pushed the available pulse duration down to a few femtoseconds [32]. Today, Ti:sapphire oscillators commonly deliver nJ-pulses with pulse durations down to sub-5 fs [33]. At low repetition rates CPA-systems with several Joules within a few tens of femtoseconds, surpassing one petawatt, are possible. Such systems are commercially available and even more powerful ones are planned in the framework of the European collaboration: The Extreme Light Infrastructure – Nuclear Physics (ELI-NP), where the infrastructure for two 10 petawatt laser systems based on Ti:sapphire CPA is currently being built.

In order to decrease the pulse duration significantly, higher frequencies and broader spectral bandwidth are necessary. This can be obtained via high-harmonic generation (see. section 2.2) and for isolated pulses it is very beneficial to drive the process with close to single-cycle pulses. As HHG is a very nonlinear and quite inefficient process, pulse energies in the μJ – mJ range are necessary for a reasonable photon flux at kHz repetition rate. In the following, a short description of a commonly

used laser source is given. A slightly modified version serves as the starting point for the development of the cryogenic cooled second stage in order to enhance the pulse energy while maintaining the broadened octave spanning bandwidth and the compression close to single-cycle pulse duration.

3.1 Description of a Common Laser Source for HHG

A popular laser source for isolated attosecond pulse generation [1, 34] is the Femtopower PRO CE-Phase HP/HR (Femtolasers Productions GmbH). Its usual output parameters are 1 mJ pulses compressed to less than 25 fs at a repetition rate of 3 kHz which can be carrier envelope phase (CEP) stabilized (see Sec. 3.3.3 for explanation and description). These pulses are then spectrally broadened in a 250 μm diameter hollow core fiber filled with neon gas. A broader spectrum supports a shorter pulse, as long as the dispersion is managed well. Ideally, the spectral components are all in phase and form the Fourier-limited pulse given by the Fourier-transform of the amplitude spectrum.

This can be achieved by chirped dielectric multilayer mirrors (chirped mirrors) that compensate the dispersion of air and glass traversed by the laser pulses. In the visible and near infrared spectral region their dispersion is normal, inducing, so called, positive chirp which means that higher frequencies are delayed compared to the lower frequencies and the carrier frequency is time-dependent and thus chirped. After recompression the pulse energy is typically around 400 μJ and the pulses sub-5 fs in duration. Pulses like these have been used very successfully for several experiments in the energy range from 70 to 125 eV [5, 16, 35, 36].

The Femtopower (called 'amplifier' in this section) itself is seeded with a Ti:Sapphire oscillator, which is pumped by a continuous wave (cw), frequency doubled Nd:YVO₄ laser (Verdi, Coherent). The oscillator is Kerr-lens mode-locked for pulsed operation with a repetition rate of ≈ 80 Mhz and supports a broad spectrum with compressed pulses down to 7 fs pulse duration. The pulses pass through a Faraday Isolator, which suppresses the optical feedback from the amplifier to the oscillator, and a 10 cm SF-57 glass block, which stretches the pulses to more than 10 ps. These chirped pulses are then amplified in a second Ti:Sapphire crystal in the amplifier. The pulses are chirped in order to increase the damage threshold for the optics so higher pulse energies can be reached; this setup is called chirped pulse amplifier. This 9-pass multi-pass amplifier amplifies the pulse energy by six orders of magnitude, limited by the damage threshold of the crystal.

The amplifier crystal is pumped by a green (527 nm resp. 532 nm) Q-switched frequency-doubled Nd:YLF laser (or alternatively by a frequency-doubled Nd:YAG laser) and put in a small vacuum chamber to protect the crystal from dust and to

3.1. Description of a Common Laser Source for HHG

allow it to be cooled to a temperature of ≈ 200 K. After the fourth pass a pulse picker, a Pockels cell, is timed such that it selects single pulses, at the repetition rate of the amplifier pump laser, from the rest of the MHz pulse train, and turns their polarization by roughly 90° . A Berek compensator which introduces an adjustable retardation and can thus be used as polarization compensator is used to fine tune the polarization difference of the pulses to exactly 90° before the rest of the pulse train is separated from the single pulse by a polarizer. After nine passes of amplification the pulses enter the last part of the amplifier, the compressor. For this amplifier the compressor consists of two pairs of prisms which provide the necessary negative dispersion to compress the pulses.

To be able to reach 25 or even 20 fs pulse duration it is necessary to compensate the higher orders of dispersion, which can e.g. be done as in this system by higher order chirped mirrors, and to avoid spectral gain narrowing, caused by the non-uniform gain in amplification [37], by using a suitable spectral filter in the seed beam. In newer versions an acousto-optic programmable dispersive filter (AOPDF, 'Dazzler', Fastlite) is used to optimize spectral shape and dispersion [38, 39].

These 1 mJ, 25 fs pulses get spectrally broadened in a hollow core fiber setup and are subsequently recompressed by a chirped mirror compressor to below 5 fs. A picture of the hollow core fiber (HCF) setup is shown in Fig. 3.6 b) and the chirped mirror setup is shown in Fig. C.1.

For isolated attosecond pulse generation it is crucial to have a sub-two cycle laser pulse in order to be able to spectrally separate the highest energy pulse from the others, for more details on HHG see section 2.2. For an isolated attosecond pulse only the high energetic cutoff can be used. Some experiments require higher photon energies, which for HHG scale with $E_{cutoff} \propto I_{max} \lambda^2$. In order to reach higher cutoff energies either higher intensity or a longer central wavelength of the driving laser are necessary. For all experiments a high brilliance is desired as it improves statistics and reduces the influence of slow temporal effects like temperature drifts.

Using lasers with longer wavelengths for HHG is still a quite new research field as ultrashort optical parametric chirped-pulse amplification (OPCPA) systems [40, 41, 42] suitable for isolated attosecond pulse generation still have to be improved to serve as a stable source for XUV experiments. And although very high photon energies can be reached this way the conversion efficiency is comparably low as it scales with $\propto \lambda^{-5.5}$ [22].

Higher photon numbers and/or higher photon energies should be attainable with

higher pulse energies without altering the other laser parameters, which is the technical goal in laser development of this thesis.

3.2 Design Considerations

As higher pulse energies from the Ti:Sapphire amplifier are wanted there are two means to boost the energy. The first one is to amplify more, but most systems work already close to the damage threshold of their optical components. In order to achieve a higher output power it is either necessary to adjust the complete geometry of the system or to add a second amplification stage with increased pump and seed sizes which allow to amplify higher without risking damage. The second way is to reduce the losses in the system, especially those which can't be compensated by more amplification. These are mainly the losses in the compressor. A prism compressor is already quite efficient with a good transmission efficiency of $\approx 80\%$. The only compressor setups for mJ laser systems with higher transmission are bulk glass compressors and broadband transmission gratings. Both options were realized and optimized in the course of this thesis.

3.3 Two-Stage Amplifier with Glass Compressor

With these two options available, the present knowledge with a 10 Hz high energy laser system in house [43] which already uses a bulk glass compressor and the prospect that the more rigid design of a bulk glass compressor provides a more stable CE-phase, the negative dispersion setup was the first choice. The schematic design of the setup is plotted in Fig. 3.1. The first amplifier stage is a modified Femtopower as described in Sec. 3.1 and its detailed optical layout with implied changes thereof is shown in Fig. A.1 on page 106. The amplifier is pumped by a Thales Etna at 4 kHz and delivers 1–1.2 mJ per pulse. Below 1 mJ the pulse to pulse stability degrades and more than 1.2 mJ increases the probability of amplifier crystal damages dramatically.

In order to amplify the near-infrared (NIR) pulses further they are sent to a second Ti:Sapphire multipass amplifier which was built in cooperation with Thales Lasers (now Thales Optronique) which is pumped by two Etna HP lasers in a crossed configuration from both sides. Boosted to 4 mJ per pulse, the stretched and amplified pulses are sent through the glass block compressor which compresses them

3.3. Two-Stage Amplifier with Glass Compressor

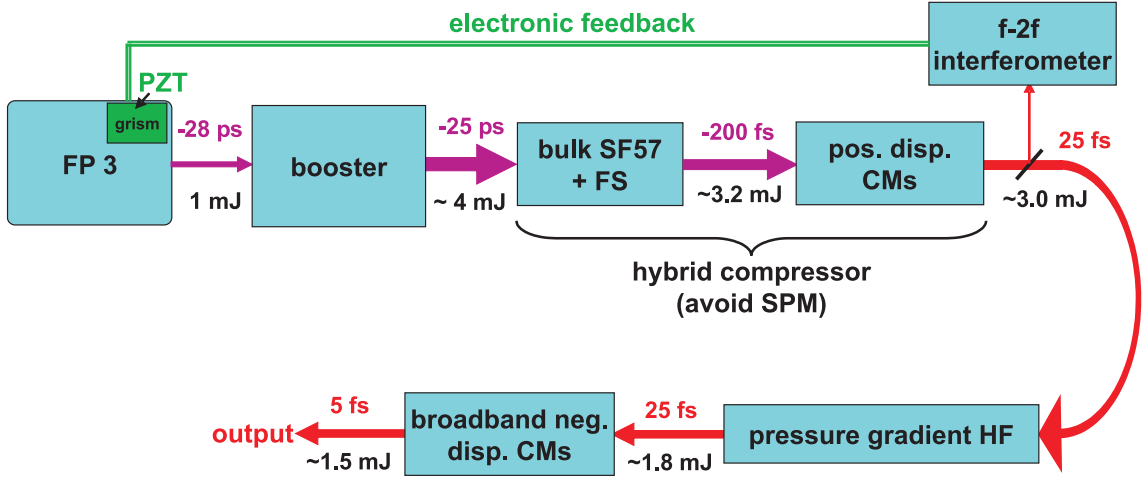


Figure 3.1: Schematic system setup of the two-stage amplifier with grism stretcher and glass compressor

down to 200 fs and a set of eight chirped mirrors (CM38) provides the final compression. This setup with additional chirped mirrors avoids nonlinear effects caused by a compressed pulse inside the bulk glass. The compressed pulses are then focused and broadened in a neon-filled hollow-core fiber. Due to the higher intensity a differentially pumped setup might provide better results than the common static setup see Sec. 3.3.2 for more details. The generated white light pulses will be recompressed to sub-5 fs and should contain around 1.5 mJ, which is three times more than the standard Femtopower.

Damage threshold considerations for the crystal and the mirrors ($\approx 10 \text{ J/cm}^2$) and more importantly the suppression of nonlinear effects in the gain medium and the chamber windows of the second stage demand a pulse stretched to 25 ps and as the glass compressor introduces positive dispersion a stretcher with negative dispersion is needed. In order to be incorporated in the existing Femtopower housing the stretcher should be compact and if possible have high transmission in the amplified spectrum. A grating prism combination (grism) seems to be the best option [44, 43]. It also allows to not only (pre-)compensate one order of dispersion but two, but all dispersive elements in the setup have to be considered for the exact design. In order to compress a 25 ps pulse with the typical Ti:Sa amplifier spectrum it takes $\approx 1.4 \cdot 10^5 \text{ fs}^2$ which corresponds to more than 3 meters of fused silica dispersion. The compressor should be compact but induce minimal nonlinear effects inside the glass. A physical measure of the accumulated nonlinear effect is given by the B integral:

$$B = \frac{2\pi}{\lambda} \int n_2 I(z) dz \quad (3.1)$$

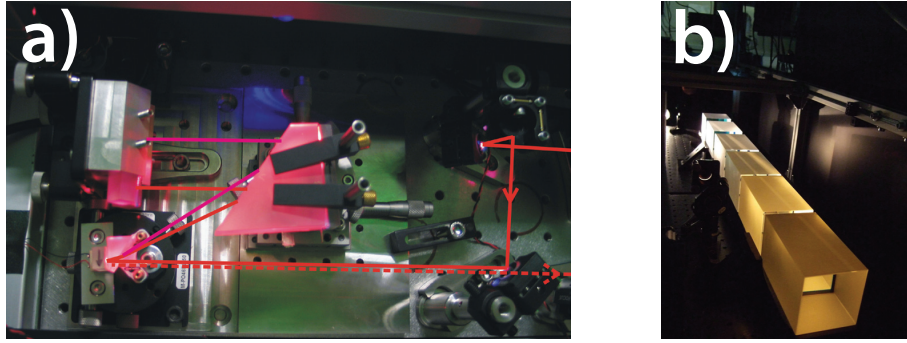


Figure 3.2: Top-view of the grism setup in a). The beam-path is indicated. The pink coloring is from scattered laser light. b) shows the lined up glass blocks. Four SF57 glass blocks (135 mm each), the F2 (110 mm) and the cube shaped fused silica block. Their aperture is $70 \times 70 \text{ mm}^2$.

After taking all aspects into consideration the compressor was designed to consist of 4 times 135 mm of SF57 a highly dispersive heavy glass, 110 mm of F2 and 70 mm plus 30 mm of fused silica. This is a compromise to keep the B-integral small while keeping the setup compact. The long pulse is compressed fast and the shorter the pulse becomes a less dispersive and less nonlinear glass is chosen. By avoiding the (almost) compressed pulse inside the fused silica and using chirped mirrors for the last step of the compression the B-integral can be reduced even further. After fixing the compressor parameters all optical components in the system are known and the grism parameters can be designed in such a way to precompensate the second and third order dispersion. Gold blazed gratings and N-BK7 prisms with an apex angle of 37.7° spaced 1 mm apart form the two parts of the grism-stretcher. The angle of incidence on the first surface and the distance between the two gratings can be adjusted to optimize the compression. A picture of the grism setup and the glass blocks is shown in Fig. 3.2. For more details see chapter 2. in [45]. The next section will focus on the mentioned different parts and their realization towards the design parameters.

3.3.1 Amplification

As mentioned before, the amplification takes place in two stages; the first one is a Femtopower with a redesigned stretcher and no compressor and the second stage consists of four passes through a highly doped ($\alpha=4.4/\text{cm}$) $6 \times 6 \times 8 \text{ mm}^3$ brewster-cut cryogenic cooled Ti:Sa-crystal placed in a high-vacuum chamber continuously pumped by a 2l ion getter pump. The cryogenic agent is pressurized helium. In use the crystal temperature is $\approx 80 \text{ K}$ at 100 W pump power. The original optical setup

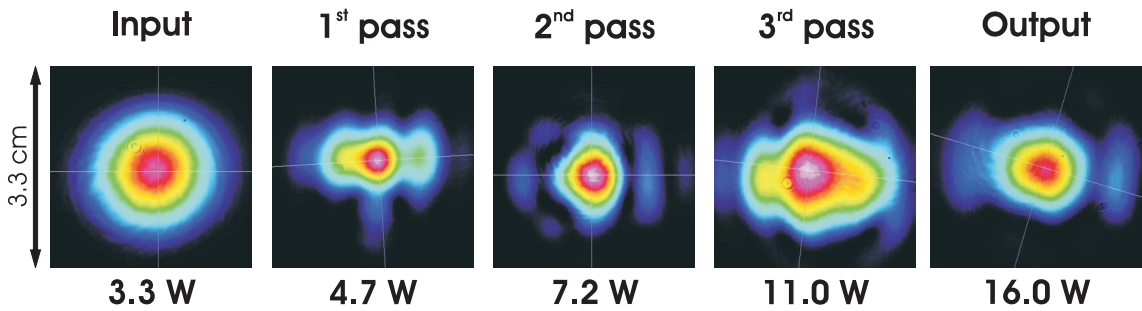


Figure 3.3: The development of the beam profile of the amplified beam in the 2nd stage with the improved crystal holder. Shown are the profiles at the crystal position for the next pass and the measured power at that position. So the picture in the middle shows the beam profile after two passes of amplification with 7.2 W power at the crystal position meaning it is the profile which will be amplified in the third pass of the amplifier. The Output shows the beam profile after the last(forth) pass.

of the second amplifier is shown in Fig. A.5 on p. 110 and a picture of the chamber and the optics are in Fig. 3.4 b) and c). The design is calculated for a 0.8 mJ, 25 ps input pulse to be amplified to 4 mJ. The amplification per pass starts at 1.6 and drops due to saturation to 1.3 for the fourth pass. For this amplification the pump volume or rather the beam diameter of the pump lasers is supposed to be around 1.5 to 2 mm and the seed size around 1 mm in the crystal.

In the beginning this target output power was hardly achievable and only with very bad output beam profiles. The reason for the degradation of the beam profile was due to strong thermal lensing caused by insufficient heat transport from the crystal to the cool finger. A new crystal holder with better heat transport helped significantly to improve the system (see chapter 2 of [45] for details). The alignment and optimization for the second-stage amplifier are complicated by a few things. The first one being the thermal lens which results from the necessity to keep the seed beam from diverging, which also leads to high intensity on the turning mirrors. Furthermore, this means the alignment is strongly affected by any other change in the system e.g. small changes in the divergence of the first stage. Additionally this means it is difficult to keep the seed in the crystal at a similar size for each pass (see Fig. 3.3). It is important to keep the intensity of the NIR-laser below damage threshold, a too small beam could damage the crystal and has to be avoided, on the other hand, a larger beam diameter experiences stronger wavefront errors caused by the thermal lens which impairs the beam profile.

The second challenge is given by the ETNA HP pump lasers. These are Nd:Yag lasers which deliver a quasi-gaussian beam profile, which is however very dependent

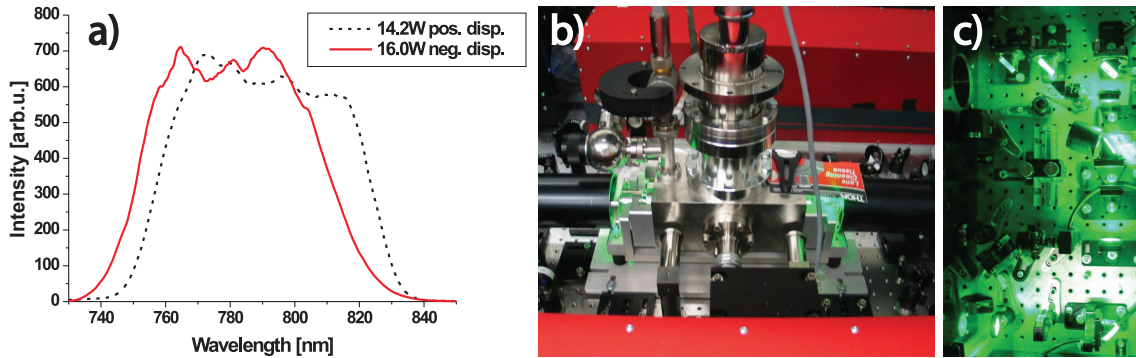


Figure 3.4: a) Comparison between measured amplified output spectra of the common positive dispersion setup and the negative dispersion setup at similar pulse energies: The leading spectral components always see a slightly higher gain and thus causes a blue shift of almost 10 nm for the neg. dispersion setup. b) Second stage vacuum chamber c) One side of the second stage optics

on the pump current. The peak intensity of the pump beam stays constant over a great range but the focal size increases with higher current, thus changing the pump current is not an option to change the pump intensity. This of course can be handled by a waveplate and a polarizer, but for adjusting the maximum achievable intensity the focusing geometry has to be optimized each time. The 2nd stage is designed for s-polarization, which makes the mirrors more efficient in the whole spectral range. In order to image all the beams at the focus the beam has to be attenuated and due to the polarization it takes at least two glass reflections (each 10 %) before filters can be used to attenuate the beam further, even then nonlinear effects in the filter might falsify the imaged beam profile if the beam is too intense. The achieved power for each pass and the beam shapes in the crystal acquired with the new crystal holder are plotted in Fig. 3.3.

As the pulse is negatively chirped for this CPA the blue components of the pulse see a slightly higher inversion of the laser medium in each pass which leads to a blue shifted amplified spectrum compared to a positively chirped system under similar conditions. A comparison of recorded spectra is shown in Fig. 3.4 a). The red spectrum supports a 21.8 fs pulse. This duration, however, can only be reached if the wavefront of the beam is not distorted and the pulse is dispersion free.

The compression was accomplished with the glass blocks mentioned above and dielectric mirrors which were also designed to compensate the residual 4th order dispersion. Fine adjustments were made with the Dazzler, after a rough compression was achieved by adapting the distance between the two gratings. At 4 mJ output-

3.3. Two-Stage Amplifier with Glass Compressor

power of the 2nd stage a compression to 30 fs was the best result. The laser spectrum supports much shorter pulses though. In order to narrow down the possible causes the pulse after the first stage was compressed by bypassing the second amplifier stage. The output of the 1st stage was well compressible to 22 fs. Pulse duration characterization by single shot frequency resolved optical gating (FROG) of the 4 mJ result is shown in Fig. 3.5 a) and the sub-1 mJ cases with differently shaped spectra are shown in b) and d). Besides the measured and retrieved spectrograms of the pulse the input spectra (black dashed), the retrieved spectra (cyan) and the retrieved spectra (red), using the marginal correction for second harmonic FROG, are plotted over wavelength in nm. In subplot b), c) and d) the spectrograms are the spectrally margin corrected versions. This margin correction is necessary because the nonlinear response of the medium is not constant over the full bandwidth of the spectrum thus usually less bandwidth gets retrieved. By using the input spectrum and calculating the consequential measured spectra this error can be corrected. This works particularly well with low noise spectrograms. Naturally the retrieved spectra from the corrected spectrogram are in better agreement with the reference input spectrum. The inability to compress the pulse to its Fourier limit (a) despite the fact that it works for the first stage output alone (b and d) reveals that the difficulties with the compression have to be introduced in the second stage or are due to the higher intensity and/or the bigger aperture used going through the glass blocks.

To tackle this problem with higher pulse energy, a setup was tested, in which the pulse was amplified to 1.0 mJ (instead of 0.8 mJ) and only two passes were used in the second stage to amplify it up to 3 mJ which could be compressed to sub-24 fs, as shown in Fig. 3.5 c), which is a big improvement compared to a). Additionally, in order to achieve this result the dielectric mirrors after the glass blocks were exchanged for four 2" PD70-mirrors which were placed directly behind the glass blocks before the telescope which reduced the beam size by a factor of 2.25, whereas the CM38 mirrors were 1" mirror only usable with the smaller beam.

The complete compressor setup is not lossless, but with 85% from amplifier output to compressor exit it is a very efficient compressor. For the next step towards isolated attosecond pulses the spectral broadening in a noble gases, also called white light generation, a sub-24 fs pulse with more than 2.4 mJ is available.

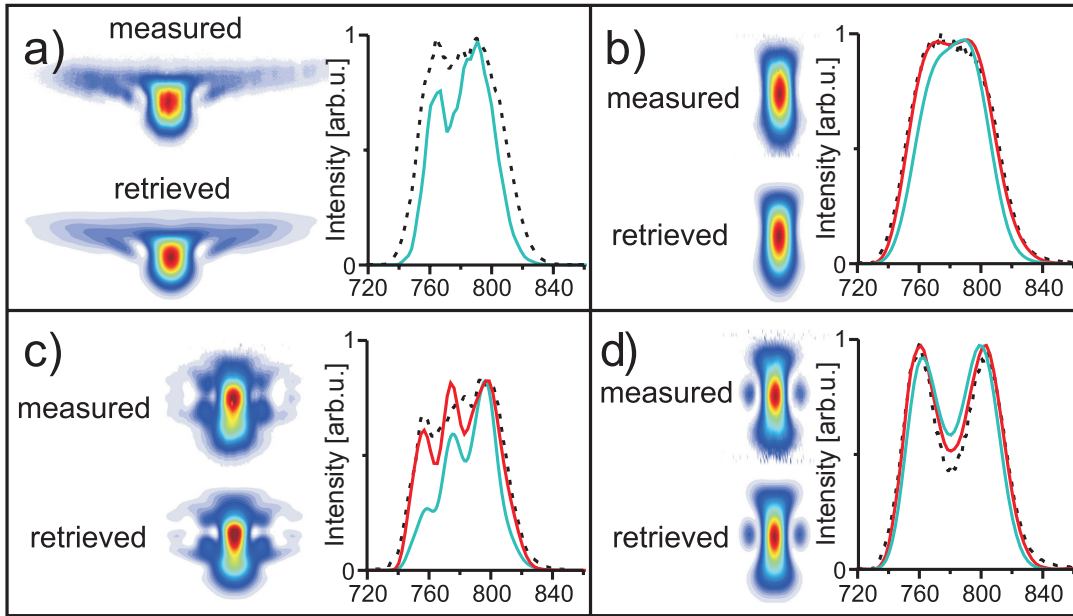


Figure 3.5: Plotted are the measured and retrieved spectrograms (frequency over delay) of a SH-FROG as well as the input spectrum (black dashed) and the retrieved spectrum (cyan). The retrieval can be corrected by using the measured input spectrum as a reference (marginal), which compensates e.g. a non-uniform nonlinearity of the measurement like phase matching or a wavelength dependent nonlinear refractive index $n_2(\lambda)$. The spectra retrieved this way are plotted in red. For a) the laser parameters are 3.3 mJ and the pulse duration ≈ 30 fs achieved by the first four pass configuration; b) and d) with 1 mJ without the 2nd amplifier stage show a almost perfect compression of 22 fs resp. 21 fs FWHM; c) 2.4 mJ using only two passes in the 2nd stage, pulses were compressed to 24 fs.

3.3.2 White Light Generation

White light generation in a hollow core fiber filled with gas is a complex process as several nonlinear effects contribute to the evolution of the pulse. The most important ones are self-focusing, field ionization, self-steepening, Raman scattering(if possible) and of course the dominant effect for broadening, self-phase modulation (SPM). The coupling from free propagation to the hollow core fiber (waveguide), the propagation and dispersion of the pulse are also important in order to describe the whole picture of the broadening process. A brief overview is e.g. given in [45] or in full detail in Boyd's Nonlinear Optics [11] and a sophisticated simulation is done e.g. in [46, 47]. For 1 mJ NIR laser systems there is a nice set of parameters which provide broad spectra and well compressible pulses with fairly high transmission efficiencies exceeding 50% [35]. For higher energy pulses [48] is a good example. With higher pulse energy or more precisely higher intensity the nonlinear effects get stronger,

3.3. Two-Stage Amplifier with Glass Compressor

which makes efficient coupling into a gas filled HCF with a typically inner diameter of $250\ \mu\text{m}$ very difficult. One solution is to use fibers with bigger inner diameters to reduce the peak intensity at the focus and nonlinear focusing or to use a differentially pumped setup which allows coupling into the fiber in vacuum but still provides broadening when the pressure increases inside the fiber. For even higher power it might be useful to combine both approaches as e.g. Suda et al. [49] who were able to reach 75% throughput with more than 6 mJ pulse energy as output by using a 2.2 m long argon filled HCF with an inner diameter of $500\ \mu\text{m}$.

The spectral broadening for a Gaussian pulse is roughly given by:

$$\delta\omega_{\text{max}} = 0.86 \Delta\omega_0 \frac{L_{\text{eff}}}{L_{\text{NL}}}, \quad (3.2)$$

where $\Delta\omega_0$ is the $1/e$ half width and L_{eff} the effective length of the nonlinear medium defined as

$$L_{\text{eff}} = \frac{1 - e^{-\alpha L}}{\alpha}. \quad (3.3)$$

and L_{NL} the nonlinear length

$$L_{\text{NL}} = \frac{cA_{\text{eff}}}{n_2\omega_0 P_0} \quad (3.4)$$

with c the speed of light, A_{eff} the effective mode area, the nonlinear refractive index n_2 , ω_0 the central frequency and P_0 the peak power of the pulse. For more broadening either higher peak power is needed (smaller fiber) or a more nonlinear medium or more of it (higher pressure/longer fiber/different gas), but there is also a limit to the intensity which can be used. This limit is roughly given by the multi-photon-ionization threshold given by the critical intensity:

$$I_{cr} = \frac{P_{cr}}{A} = \frac{\pi(0.61\lambda)^2}{8n_0n_2pA} \stackrel{\text{for neon}}{\approx} 2 \cdot 10^{14} \frac{W}{\text{cm}^2 \text{ bar}} \quad (3.5)$$

White light generation in gases can also be done without the guiding of hollow core fibers in a filament. Good examples are given by Stibenz et al. [50] with 8 fs pulses with 4 mJ at 1 kHz and Chen et al. [51] with 5 fs and 0.7 mJ at the same rep. rate. While using a filament is a bit simpler, using a hollow core fiber provides a prolonged nonlinear interaction and even the losses help to maintain a nice beam mode. A good overview of the two alternatives for mJ laser systems can be found here [52]. The superior stability and lower required intensity for similar broadening combined with the more uniform beam profile is in our opinion more beneficial than the higher power transmission filamentation provides.

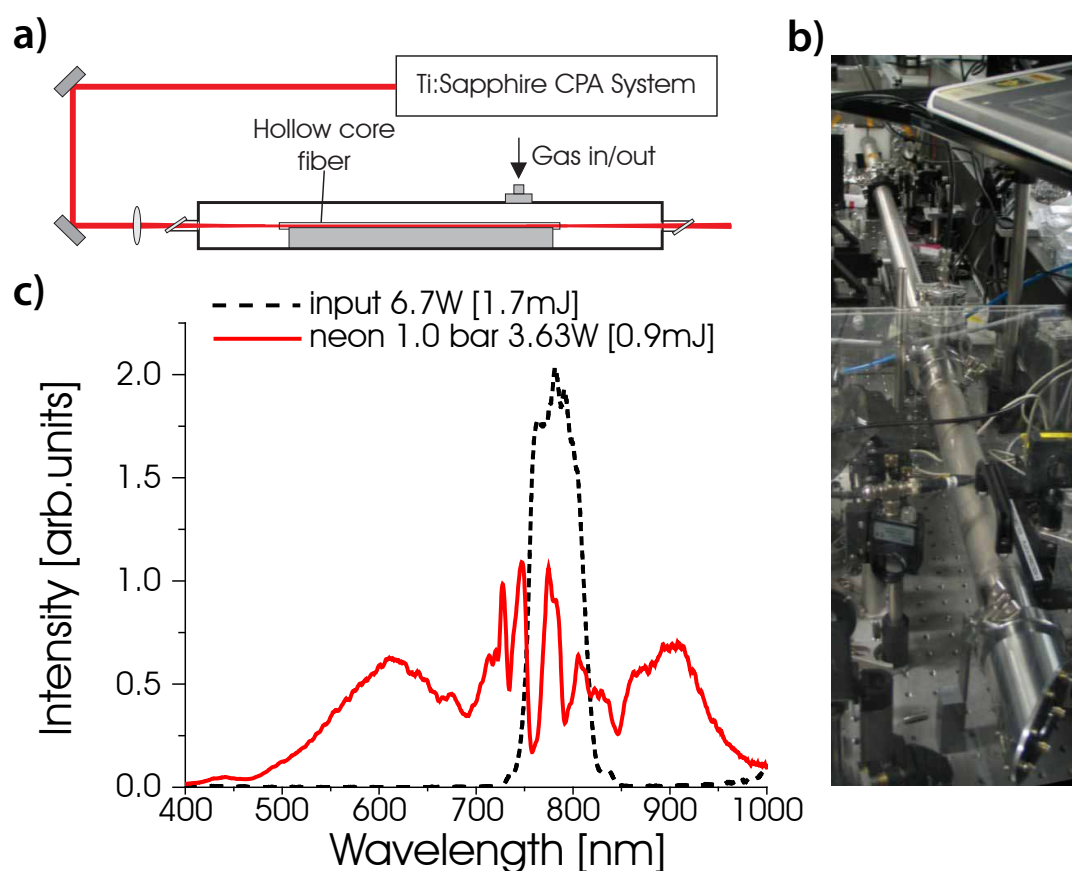


Figure 3.6: a) shows a schematic of the static pressure HCF setup, b) a picture of the fiber chamber in the laboratory and c) shows the spectra and power before and after the broadening.

Static Pressure Setup

The simpler and more commonly used setup for HCFs is the static pressure setup which consists of an evacuable chamber, typically a tube, filled with a noble gas and the HCF is placed in the chamber such that it serves as a straight waveguide for the focused beam (schematic in Fig. 3.6 a)). With such a waveguide the nonlinear interaction length is extended from the filament length to the waveguide length plus about the half filament length increasing the accumulated effect. However it is difficult to find the right beam parameters to couple into the fiber efficiently as it is not only defined by the focusing but also by the nonlinearities in the gas filament. Self-focusing makes the focus smaller and shifts the focus position towards the lens. Considering all this for the two-stage amplified beam a $400\ \mu\text{m}$ HCF with 1.2 meter length was used. A typical spectrum for input pulses with 1.7 mJ and the broadened output spectrum with 0.9 mJ using this fiber are plotted in Fig. 3.6 c). Using more

3.3. Two-Stage Amplifier with Glass Compressor

input energy didn't improve the output in terms of energy and mode hence not the full energy was used. For the reduced input energy of 1.7 mJ the transmission efficiency is still above 50 % which is good, but compared to the full energy available the efficiency is only around 38 %. Also with only 3 mJ pulse energy output of the second amplifier stage higher energies are in principle still available. In order to achieve the best mode and efficiency possible it is crucial that the fiber is straight and aligned perfectly to the laser beam. XY-stages at the entrance and the exit of the fiber are used to position the fiber correctly. The setup is very sensitive to the alignment of the front of the fiber which makes the use of stable high precision stages advisable.

The classic static pressure setup works well for moderately amplified energy in the second stage but seems to reach a limit around 1 mJ output power. Small improvements might be possible with better fitting core diameters of the fiber and a better focus profile, but big steps certainly need a different approach. For high power lasers, differentially pumped fibers have reached the multi-mJ scale as shown in [49] where up to 5.0 mJ were compressed. The scheme of differentially pumping the fiber entrance was tested as well and the results will be presented next. It should also be mentioned that using circularly polarized light instead of linearly polarized light [53, 54] shows improvement with higher laser power as field strength and thus ionization is reduced which is one of the limiting factors of this setup. However, for HHG a linearly polarized electric field is necessary so the accelerated electron can recombine with its parent ion to emit the high energy photon. Turning a circularly polarized field back to linearly polarization becomes increasingly more difficult the broader the spectrum of the field is, but once this is possible for the full broadened and compressed spectrum this could be utilized as well.

Another option is the compression of different, spectrally separated, arms of the white light [55]. Splitting up the laser power into multiple beams before broadening and using different frequencies for each beam may allow to broaden each of them in an optimized fiber for that wavelength and power. The separate beams can be recombined before or after the chirped mirror compression and then be used for experiments. This approach allows to scale the energy after the HCF and with different frequencies, the covered bandwidth can be increased at the cost of a complicated, interferometrically stable setup, which makes this approach technically very challenging.

Differentially Pumped Setup

As the pulse duration and beam profile results with the static approach for the multi-mJ system were not as good as for the classic setup, a differentially pumped HCF broadening scheme was tested. This means that the fiber is the sole connection between two chambers. The first one is evacuated and pumped continuously and the second one is filled with neon with an adjustable pressure. Neon is flowing through the fiber and the steady state result is a pressure gradient. The pressure of the gradient for a viscous gas is given by [56]

$$p(z) = \sqrt{p_0^2 + \frac{z}{L}(p_L^2 - p_0^2)} \quad (3.6)$$

where z is the position along the fiber, L is its length and p_0 and p_L are the pressures of the chambers. For $p_0 = 0$ the formula simplifies to $p(z) = p_L \sqrt{z/L}$. To achieve comparable broadening the accumulated nonlinearity can be compared:

$$p_s I_s(z) = \int_0^l p(z)(I_d(z))dz \quad (3.7)$$

I_d and I_s are the intensities of the differential respectively the static setup and l is the desired ratio of the fiber lengths. Assuming $I_s(z) = I_d(z) = I_0$ results in $L = 1.5$, which means that the fiber in the differential setup has to be 50% longer to achieve the same broadening. In combination with a longer focal length for the same fiber diameter due to the lack of filamentation makes this setup considerably larger than the static pressure setup.

Although the first attempts with a mechanical solution for separating the two chambers were unsuccessful (see. [45]) the colleagues Nagy and Simon in Göttingen (Laser-Laboratorium Göttingen e.V.) demonstrated great results [57] with their differentially pumped setup. In collaboration with them their setup was tested and adapted to our needs. In the end a 2.5 meter long, 320 μm core diameter fiber was used which is stretched and fixed by glue at its ends, providing a straight waveguide. In the static setup thick walled hollow core fibers are used to make it less flexible and utilize its weight in order to lay perfectly in a straight support structure. Here however, thin walled HCFs are used in order to keep its own weight low so that stretching it provides a lower radius of curvature. Considering the force used to stretch it, the radius is in the kilometer scale, making it almost perfectly straight. A schematic is

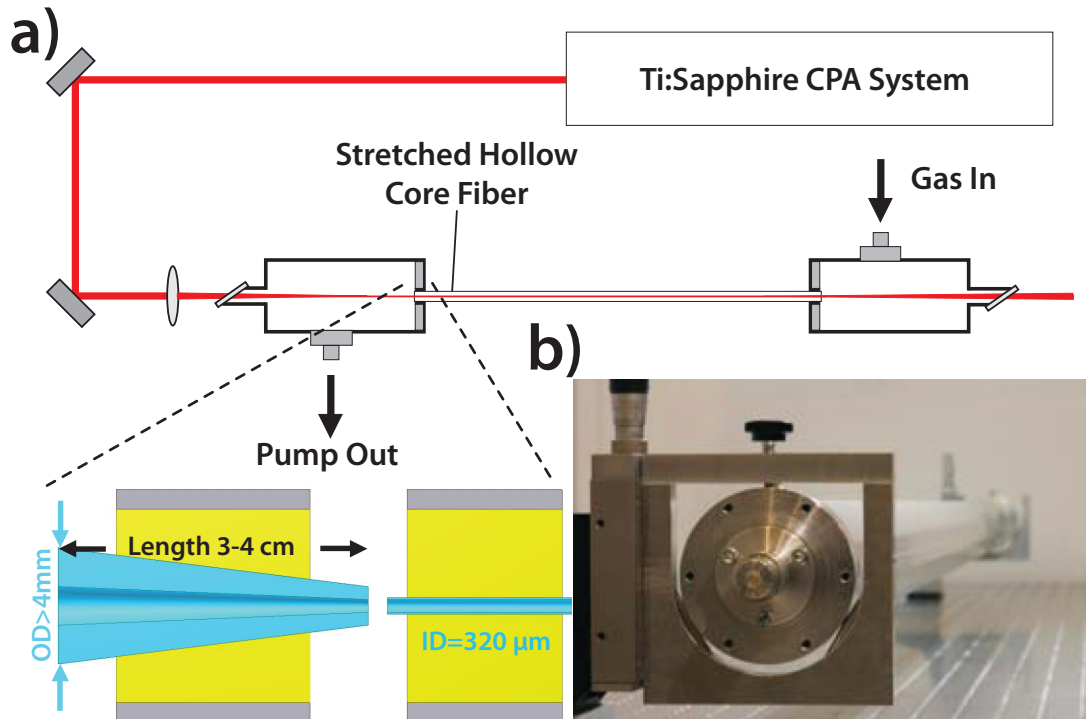


Figure 3.7: A schematic of the differentially pumped setup is shown in a) with an enlarged schematic of the tapered piece in front of the fiber. A picture of the real fiber, front side, is shown in b).

shown in Fig. 3.7 a) and a photo in b).

The coupling in vacuum has the great advantage that the focus can be measured accurately as it is not modified by self-focusing and filamentation. However, the absence of nonlinear effects increases the demand for a nicely round and well sized focus in order to couple into the fiber efficiently. As the mode of the laser used was not Gaussian but slightly elliptical and astigmatic, the coupling was suboptimal. In our first attempts we experienced some difficulties with the glue around the fiber. Because the fiber is quite small, misalignment or displacement caused ablation of the glue followed by a drastic performance loss. To avoid this risk in the future a funnel like fiber piece with much bigger outer diameter was placed directly in front of the stretched fiber without changing the in-coupling but preventing the glue from being hit directly. A schematic of this is also shown in Fig. 3.7 a).

As the chirped mirrors support a spectrum not broader than from 530 to 1050 nm additional broadening is not necessary. The neon pressure was adjusted to reach the needed broadening but with a throughput of more than 1 mJ a pressure dependent divergence of the out-coupled beam was noticed, which means self-focusing is occur-

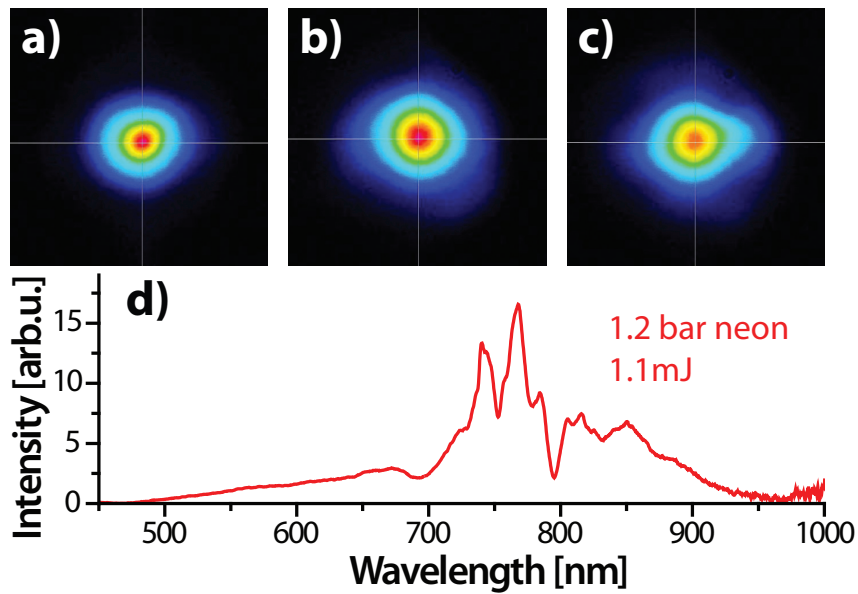


Figure 3.8: Beam profiles after differentially pumped fiber with 1.0–1.1 mJ refocused in front of the focus at the same position: a) in vacuum b) with 1.0 bar neon and c) with 1.2 bar neon. d) shows a typical spectrum obtained with the differentially pumped setup at a throughput of 1.1 mJ.

ring at the end of the fiber. The beam profiles for different pressures are shown in Fig. 3.8. The measured beam profile increases in overall size and decreases in mode quality with increasing pressure, as a result of the higher nonlinearity. Although the differences are not dramatic this dependence endangers the day to day stability of the system after the HCF. To avoid this effect we need a longer fiber, a setup with a larger hollow core diameter, or differential pumping on the exit of the fiber as well. At the time such a fiber was not available and in terms of length we are already at the limit of the optical table. The results with this fiber are shown in Fig. 3.8 d). The depicted spectrum is a typical spectrum and the throughput of a bit more than one mJ was reproducible. With new fibers the transmission was sometimes significantly higher, up to 1.6 mJ but it dropped within hours and was not reproducible. So although the glue isn't hit directly anymore there is still some damage, probably temperature-induced, to the glue, which then impairs the coupling to the fiber. The idea is very promising but a better technical solution is still necessary.

3.3.3 Compression and CE-Phase Stabilization

After generating the white light with the hollow core fiber one crucial step is left before it can be used for experiments. In order to have a short pulse we have to control the spectral phase such that all the spectral components are in phase meaning they arrive at the same time. Due to the bigger bandwidth, the difference in dispersion $n(\omega)$ becomes larger resulting in different optical lengths $l \cdot n(\omega)$ which is equivalent with saying that frequencies with higher refractive index $n(\omega)$ travel slower $v_{ph}(\omega) = \omega/k = c/n(\omega)$. For spectra shown in section 3.3.2 which support a sub-5 fs pulse a few millimeters of fused silica are sufficient to disperse the frequencies such that a 5 fs pulse becomes 100 fs long.

Typically, the beam propagates through windows and air before reaching the experiment. All these have to be (pre-)compensated by a compressor. For relatively small dispersion values special dielectric mirrors (chirped mirrors) have proven to be the dominant solution so far [58, 59, 60]. Finding the exact match to compensate the dispersion for this very broadband spectrum is not always straight-forward and takes usually some iterations for a satisfying result. The group delay from mirror reflections is not adjustable, and one can only add or subtract pairs of reflectors. Therefore a thin wedge pair is added for fine adjustment of the material dispersion, the extra dispersion added to the system has to be compensated for by more reflections on the chirped mirrors.

Metrology of fs-Pulses

In order to prove the existence of short pulses their pulse duration has to be determined. There are several techniques to measure pulse durations. Commonly used are: Intensity Autocorrelation, Interferometric Autocorrelation, Spectral Phase Interferometry for Direct Electric-Field Reconstruction (SPIDER) [61] and Frequency Resolved Optical Gating (FROG) [62]. The first two suffer from the fact that they can measure the pulse duration assuming a certain pulse shape, but provide no information about the spectral phase which can be used to optimize the compression. SPIDER and FROG provide this information, however some mathematical reconstruction is needed to retrieve it. All techniques use nonlinear processes whose response is usually not uniform for all wavelengths so with increasing bandwidth it gets more difficult to rely on these measurements. However, very short pulses were measured successfully with both, SPIDER and FROG [63, 64]. The general issue for broadband laser pulses and nonlinear effects is given by phase-matching

and thus a spectrally dependent response. By reducing the thickness of the nonlinear medium the phase matching condition becomes less limiting but at the cost of overall signal. To retrieve the pulse parameters it is typically necessary to correct the inhomogeneous nonlinear process. For some FROG techniques it becomes more difficult to detect the whole generated signal which can be angularly chirped. So for ultrashort pulses the effort to be able to rely on these measurements increases, but done correctly they deliver the correct result.

However the best way to measure a waveform is to measure the electric wave directly. In this work a technique called attosecond optical streak camera (streaking) by cross correlation is used to fully characterize the laser pulse which generates the high harmonics (HH).

Attosecond-Streaking of fs-pulses

Attosecondstreaking is a powerful tool to characterize electron wave packets and the optical light field which is streaking the electrons. A detailed explanation of the method was presented earlier in section 2.2. An isolated short XUV pulse is used to generate an electron wave packet by direct photoionization. The energy of the XUV photons minus the workfunction of the bound electron determines the kinetic energy of the electrons $E_{kin} = \hbar\omega - W_p$. If the electrons are ionized in the presence of an electromagnetic pulse, in other words experience the pulse only partially, the net momentum gain is not zero. For a linearly polarized streaking pulse the vector potential is mapped to the kinetic energy of the electrons on the axis of the polarization. The energy of the electrons in this direction is measured via a time of flight spectrometer. The kinetic energy of the electrons depends on the delay between the two pulses. Changing the delay allows to scan the vector potential of the laser pulse. A time of flight measurement is shown in Fig. 3.23 b) on page 58. The electric field of the pulse is obtained by differentiation of the vector potential. It characterizes the temporal behavior of the laser pulse at the time of flight spectrometer completely and can even measure sub-cycle optical laser pulses [65]. So it is a very reliable tool to measure short pulses as it measures directly the pulse itself.

It is however, not a single shot measurement and thus requires to reproduce identical conditions for each pulse which means that all parameters of the two pulses and the delay between the two has to be stable or respectively stabilized. The delay is handled by a feedback-controlled piezo and most of the laser parameters a quite stable by themselves all but its carrier-envelope phase (CEP).

Carrier Envelope Phase

When using long laser pulses and intensity-dependent effects the laser pulses are usually simplified to their intensity envelope as this is completely sufficient to describe these effects. When looking at processes which depend not on the intensity but on the electric field of the laser pulse it is necessary to look at the actual wave packet and its electric field which forms the pulse. For an unchirped linearly polarized pulse the electric field can be written as:

$$E_{car}(t) = E_{env}(t)\cos(\omega_0 t + \varphi)$$

where E_{env} is the pulse envelope ω_0 is the central frequency of the pulse's spectrum and φ is the offset from the cosine to the maximum of the envelope called the carrier-envelope phase. As long as the pulses are long the difference between different phases has very little influence on observed physics but the shorter the pulse is the more significant it becomes. A schematic of the CEP is shown in Fig. 3.9.

For a propagating pulse the CEP is typically not constant because the phase velocity $\nu_{ph} = \omega/k$ with k being the wave vector and the group velocity $\nu_{gr} = \partial\omega/\partial k$, the speed of the pulse, are not the same so the carrier and the envelope travel at different speeds. Another propagation phase effect is e.g. the Guoy-phase shift of a focused

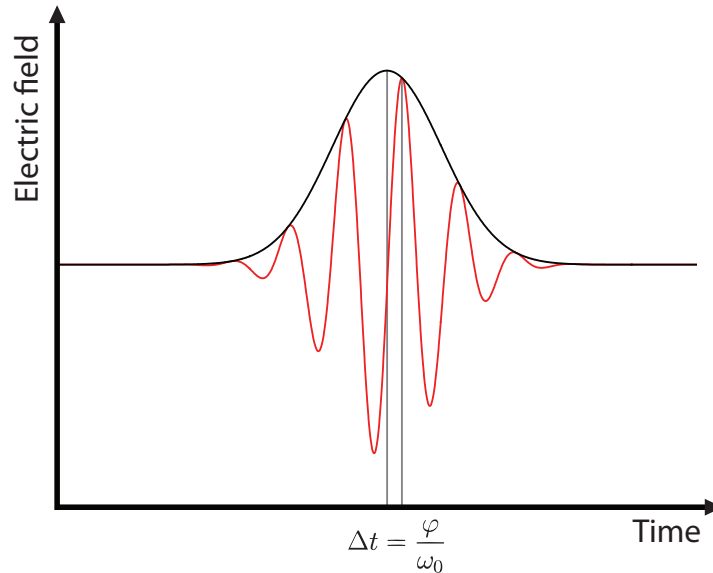


Figure 3.9: The relative position of the electric field of a short pulse in red and its envelope in black define the CE-phase. For this pulse the φ is slightly bigger than $\pi/2$.

beam [66]. For streaking and high harmonic generation it is necessary to ensure that every pulse has the same CEP.

In order to stabilize the CEP of a CPA laser system the phase has to be stabilized from the very start in contrast to OPCPA systems which are seeded by a difference frequency generated (DFG) seed. In an empty cavity the allowed modes are integer multiples of the repetition rate f_{rep} which is the inverse of the round trip time T

$$f_{rep} = \frac{1}{T} \quad ,$$

or in other words the cavity length l is an integer multiple of each allowed wavelength λ [67]. With dispersion however the cavity is not equal for all wavelengths and the effective length becomes wavelength dependent. For linear dispersion this corresponds to a constant frequency shift f_{offset} of the frequency comb. Thus every allowed mode can be written as

$$f_n = n f_{rep} + f_{offset} \quad , \quad n \in \mathbb{N}.$$

Of course not all modes carry energy. The gain medium, dispersion management, alignment etc. define the actually amplified spectrum. A schematic spectrum with frequency comb is shown in Fig. 3.10. The theoretically allowed modes are shown in gray and the realized ones in black forming the spectrum (red).

The offset frequency f_{offset} is directly related to the CE-phase shift for each round trip and thus for each out-coupled pulse.

$$\Delta\varphi = \frac{2\pi f_{offset}}{f_{rep}} \quad (3.8)$$

So in order to stabilize the CEP, f_{offset} has to be stabilized. f_{offset} is not only dependent on internal parameters but also affected by external ones like vibrations or temperature fluctuations, which change the cavity length. Two techniques used to first measure and then stabilize the f_{offset} which are used in this laser setup will be presented next. Both techniques utilize frequency mixing to gain access to f_{offset} .

f-to-zero CE-Phase Stabilization in the Oscillator

The f-to-zero technique [68] requires two steps, one optical and one electronic frequency mixing to isolate the offset frequency. First, different frequencies of the laser spectrum are combined nonlinearly in a crystal via difference frequency generation.

3.3. Two-Stage Amplifier with Glass Compressor

The newly generated frequencies are given by

$$f_{m-k} = f_m - f_k = mf_{rep} + f_{offset} - (kf_{rep} + f_{offset}) = (m - k)f_{rep}$$

which are obviously independent of f_{offset} . If the laser spectrum is broad enough, covering the same spectral area as the new frequencies, it will interfere with the difference frequency spectrum constructively or destructively depending on their phase difference which is exactly $\Delta\varphi$. A schematic overview of the frequencies involved is shown in Fig. 3.10. The second step is to isolate the interfering spectral region, measure f_{offset} and use a feedback loop to control it.

In the laser setup the compressed broadband Ti:Sapphire oscillator is focused into a periodically-poled lithium niobate (PPLN) crystal. It is quasi phase-matched to optimize the difference frequency generation (DFG) above one micrometer wavelength. Due to the high intensity the pulse spectrum also broadens via SPM, which is necessary because the fundamental oscillator spectrum without it wouldn't be broad enough to interfere with the DFG signal. The spectral components are then separated first by a dielectric mirror which reflects the seed for the amplifier but transmits the blue and the infrared components which are then isolated by an appropriate long pass filter. The infrared is then focused onto a fast photo-diode measuring the phase-dependent intensity modulated pulses caused by the beating of the two optical frequencies separated by f_{offset} . In the laser system the reflected blue part is used as a reference signal for the clock which triggers all electronic devices used after the oscillator.

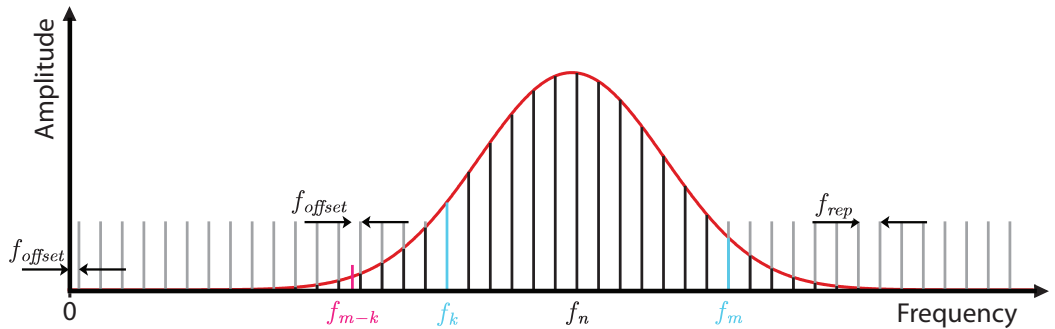


Figure 3.10: Schematic of frequency modes in the oscillator. Realized modes are black with the intensity envelope in red. In order to determine f_{offset} the difference frequency f_{m-k} is generated by mixing f_m and f_k in a suitable crystal. The frequency modes resulting from the mixing process are shifted by f_{offset} compared to the fundamental laser modes. The beating frequency can be detected on a diode.

The diode-signal is then coupled to an electronic locking box (Menlo Systems) which compares the beat signal (f_{offset}) with a reference frequency $f_{rep}/4$ to form an error signal for the feedback which is applied to an acoustic optic modulator in the pump beam of the oscillator. The pumping power affects the intra cavity dispersion of the oscillator and thus serves as a mean to control the CE-phase.

By locking the f_{offset} to $f_{rep}/4$, $\Delta\varphi$ is stabilized such that every fourth pulse has the same CE-phase (see Eq. 3.8). With this setup it is not possible to stabilize every pulse because the error signal would be injective and worthless for a feedback. There are other techniques which overcome this drawback [69]. For this system however it is insignificant as the pulse picker in the following amplifier picks exactly every 19500th pulse.

f-to-2f CE-Phase Stabilization

As attosecond experiments are not conducted with weak oscillator pulses, but with strongly amplified, spectrally broadened and recompressed laser pulses stabilizing the output of the oscillator is not sufficient. Throughout the whole laser setup the pulses are susceptible to fluctuations which might also affect their CE-phase. So after amplification and spectral broadening a second feedback is used to compensate for fluctuations of the stabilized CE-phase. The technique is very similar to the one described above it just utilizes a different nonlinear process, namely second harmonic

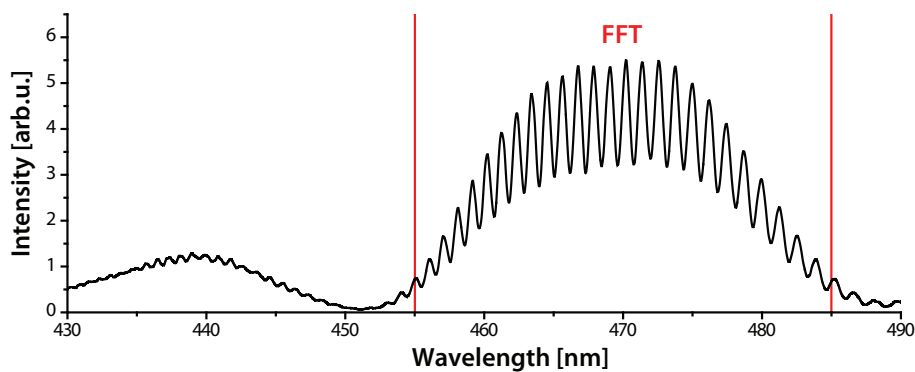


Figure 3.11: Spectral interference between fundamental and second harmonic in the spectral range of 455 nm to 485 nm. The Fourier-transform of the spectrum has an intensity peak according to the delay between the pulses. A CE-phase change results in a change of the phase difference between the two pulses moving the fringes (left and right) which is described by the phase of the Fourier transform at the respective frequency.

3.3. Two-Stage Amplifier with Glass Compressor

generation.

$$f_{SHG} = 2f_n = 2(nf_{rep} + f_{offset})$$

Two infrared photons generate a blue photon which is then spectrally interfering with the fundamental blue light. The difference of the new and the old frequency comb is given by

$$f_{SHG} - f_{2n} = f_{offset}$$

which leads to spectral interference depending on the CE-phase.

The actual setup is a bit simpler than for the oscillator. A weak reflection from a glass wedge used for adjusting the dispersion for the white light compression is focused into a beta-barium borate (BBO) crystal and then refocused onto a spectrometer entrance slit. In order to adjust the intensities of the two beams a waveplate and a polarizer are added before the spectrometer. As the incoming pulse is not compressed interference between the fundamental and the second harmonic causes spectral fringes. With fixed setup and alignment the delay between fundamental and second harmonic is constant which makes changes in the CE-phase observable as a change in the spectral position of the fringe peaks or mathematically as the phase of the Fourier transform of the oscillation's frequency. This can be used as an error signal for a feedback loop which translates the small grism half in the laser stretcher changing the dispersion to keep the CE-phase constant. A typical recorded interference spectrum with fringes is shown in Fig. 3.11.

This measurement is used to compensate drifts in the system that occur in the CPA

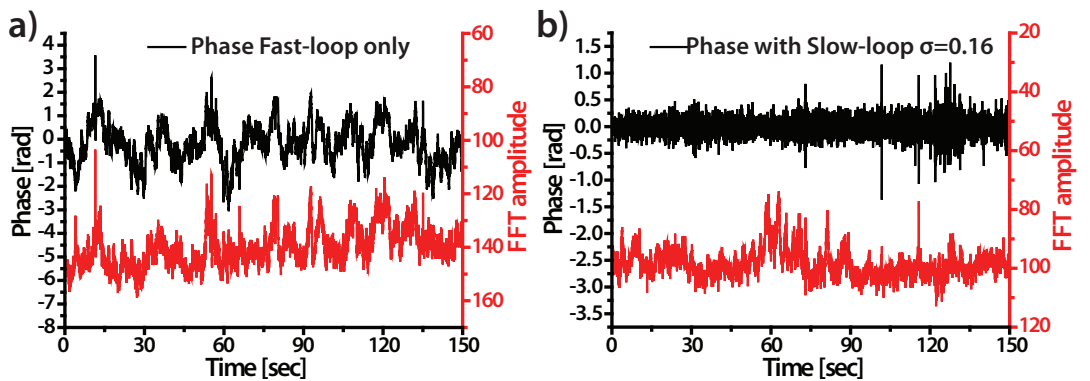


Figure 3.12: Plotted are the phase and the amplitude of the Fourier transformed f -to- $2f$ spectrum after broadening the laser pulses in a hollow core fiber. In a) only the fast stabilization of the oscillator is switched on. A strong correlation between the two curves is obvious. In b) the measured signal is used as a feedback for the Slow-loop stabilization resulting in an in-loop error of 0.16 rad rms.

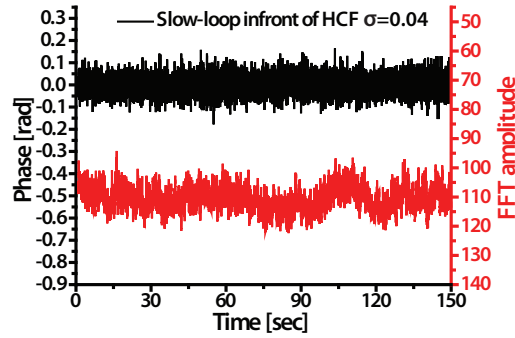


Figure 3.13: Fast and Slow-loop stabilized CEP measurement in front of the HCF showing almost a factor of four more stable error signal due to the better pulse to pulse stability at this point in the laser system.

system but there are still some components after the f-to-2f measurement on its path to the experiment and also e.g. power fluctuations can mimic CE-phase changes in this measurement. Therefore a less stable laser produces a less stable signal and feedback. This can be seen in Fig. 3.12 a) in which the changing CE-phase (black) and the amplitude of the oscillations (red) is shown after the hollow core fiber without the slow feedback loop. There is a clear correlation between the two. It is not clear if the changing power, and thus the broadening causes a CE-phase shift, or if the measurement is affected more severely as it uses the outer parts of the broadened spectrum whose phase is more susceptible to power fluctuations. A phase measurement with a stereo ATI could probably answer this question [70]. In Fig. 3.12 b) the slow-loop is switched on and the measured in-loop phase is locked with 160 mrad standard deviation which is not ideal but sufficient for attosecond experiments. As the laser stability was not optimal after the HCF the phase was also measured before the spectral broadening in the HCF. In this case a small fraction of the beam was used and broadened by focusing it into a fused silica plate. This white light is then sent to the f-to-2f setup. This measurement is shown in Fig. 3.13. Comparing Fig. 3.13 with Fig. 3.12 b) it is obvious that the laser is more stable visualized in the stable FFT amplitude and that the measured phase is with 0.04 mrad standard deviation by a factor of four significantly more stable. In summary, the CE-phase of the two-stage amplifier with a dazzler seems to be very stable. In terms of stability, power and pointing fluctuations and the HCF broadening make the system become less stable. It is however completely sufficient for high harmonic generation and attosecond streaking. The actual streaking measurements indicate a very stable CEP as it is possible to take streaking measurements without using the slow loop. This

means that the slow loop mainly has to stabilize small, slow drifts.

3.3.4 Challenges of this Setup

Most of the results presented in the sections above were acquired at reduced power or limiting the amplification to fewer passes than presented in the original design. In order to improve the setup and achieve the desired output power and stability a different concept was developed. In the following part presents the challenges which led to the decision for a different design and some technical problems which had to be solved.

Cooling Issues

The laser system requires two stronger pump lasers (in total 110 W @ 4 kHz) than the regular Femtopower and these come with power supplies and water-water chillers. In order to make space and reduce the noise level in the laboratory all this equipment was put outside of the lab in the front room with an access point to the newly installed cooling water circuit. Especially the cryo-cooling of the second amplification stage is quite noisy. It is also beneficial to remove these heat sources out of the laser laboratory in order to guarantee a stable air temperature and thus reduce drifts. The cooling water however is contaminated with black particles which are apparently abrasions from the tank's wall, which clog filters and cover the inside of the water-lines.

Additionally the functionality of the system was poor in the beginning. The feedback of the temperature regulation of the cooling water was insufficient and had to be optimized to allow stable pump laser performance. After the feedback-parameters for the big water circuit were adjusted a few times the water temperature is now stable within the specifications of one half degree – often even better.

The heat was also a problem at a different part of the system, namely at the second amplifying crystal. The setup provided by Thales showed too strong thermal lensing. Lensing is necessary to keep the beam from diverging, but excessive thermal lensing resulted in a terrible and unusable beam profile. The issue was solved by replacing the thin copper crystal mount by a new, bulkier version which can transport the heat away from the crystal to the cooling finger more efficiently. Photos of both versions can be found in Fig. A.7 on page 112.

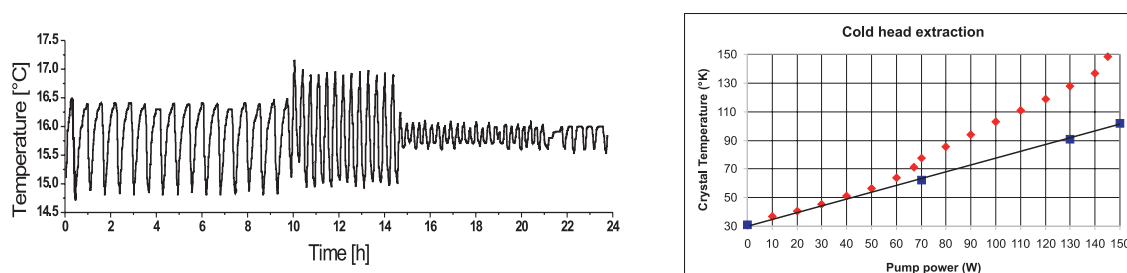


Figure 3.14: Insufficient regulation of the cooling water circuit (left) shows changes of 2°C within a few minutes which is too much and too fast for the connected chillers which dependent on a stable cooling circuit; on the right is the comparison between the two crystal holders in the second amplifier stage. The dependence of the measured crystal temperature of the redesigned holder (blue) shows a huge improvement to the first version (red) and reduced thermal lensing to a moderate level.

More detail on these two subjects can be found in chapter 2 of [45] but the two main measurements are also shown in Fig. 3.14.

High Damage-Threshold Mirrors

In the second amplification stage, the IR-pulses are amplified using only the thermal lens as focusing optic. This leads to very high intensities on the dielectric mirrors between the crystal passes. With 4 mJ, 25 ps and a FWHM beam size down to $500\ \mu\text{m}$, this exceeds the damage threshold of most mirrors. Thales installed the setup with 'TLMB' mirrors from CVI which have an improved and guaranteed damage threshold of $1.3\ \text{J}/\text{cm}^2$ for 46 fs pulses. For 25 ps-pulses it is an order or magnitude higher. The reflectivity is above 99.8% from 760–840 nm and their dispersion is designed to be very low in the supported bandwidth. The only drawback is that this bandwidth is hardly enough for our spectrum. Although the reflectivity may still be very high the spectral phase can be highly nonlinear which makes it, even with the Dazzler, very difficult to compress these spectral components. The theoretical curve of the mirrors is shown in Fig. 3.15 in green dashed and blue for the phase. The theoretical curve provided suggests a well behaved mirror reflection from 740 to 860 nm. Mirrors with these parameters (red) would be ideal for the laser system (violet). However other coating runs show a huge wavelength shift (black). The official specifications of the mirrors are $R > 99.0\%$ from 740 to 860 nm. But even if the black curve would meet the specifications, the phase error at 99% reflectivity is intolerably high and makes these spectral components incompressible and thus useless. Especially the spectral shift between the different stretcher-compressor

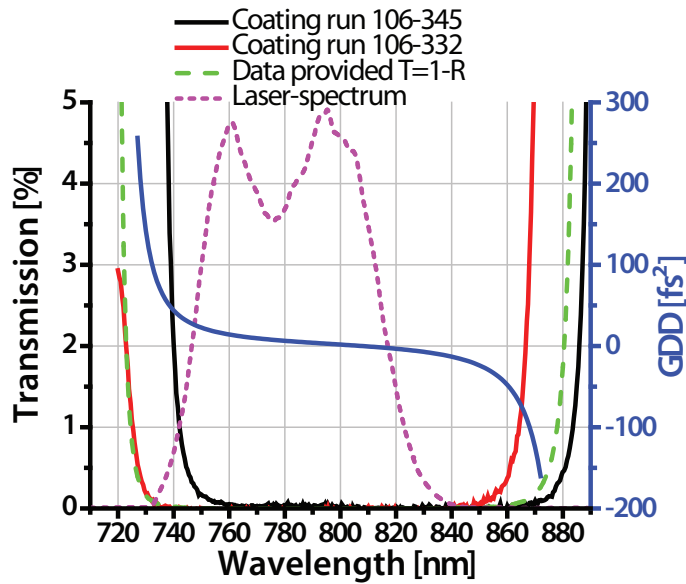


Figure 3.15: Shown are the theoretical transmission (green dashed) and the spectral phase (blue) for TLMB mirrors for 0° angle of incidence and two measured transmissions for two different coating runs of this coating (black and red). Due to the deviations from the theoretical curve several mirrors could not be used in the experimental setup.

schemes as shown in Fig. 3.4 means that some of the high reflecting mirrors can only be used in one of the two configurations. For 45° angle of incidence (AoI) mirrors, the limited supported bandwidth of the mirrors is even more problematic if they are used with p-polarization which always supports less bandwidth for high reflectors.

Beam Propagation

The toughest challenge is to broaden the multi-millijoule infrared laser efficiently. The static setup showed a saturation in transmission when using more than 2 mJ input energy. With the differentially pumped setup the focal properties limited the achieved results, due to half closed irises etc. to attain a reasonable focus profile to couple to these fibers. To find the source of this imperfect focus an extensive investigation was conducted.

A parameter set with the initial conditions of this investigation is shown in Fig. 3.16. This set was taken with reduced power; in most cases the beam was sent one pass through the second amplifier with (1.5 mJ) or without (1.0 mJ) amplifying. Only one pass was used as the thermal lensing plays such an important role for the alignment of multiple passes that recollimating it properly would involve too many changes for

a direct comparison. The columns of the figure represent three positions along the z-axis. One in the focus (peak intensity) and one before and after this position. Please notice the different zoom factors. For these measurements the laser was attenuated first by using two glass reflections (each 10%) followed by a reflective neutral density filter and finally absorptive filters directly in front of the camera. The different lines

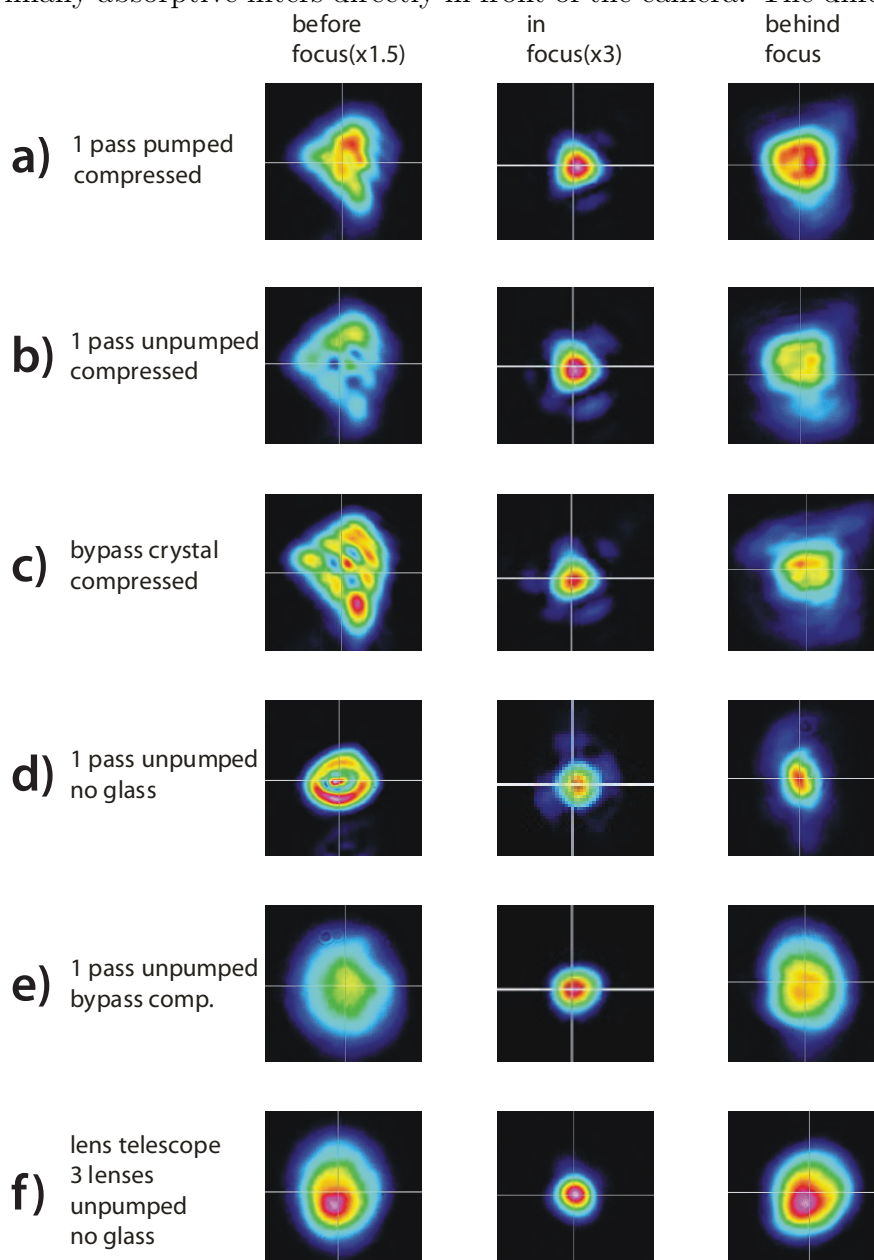


Figure 3.16: Tracing the source of the bad beam profile of the compressed pulse. Different parts of the setup are bypassed in order to identify the source. The optics in the expanding mirror telescope were identified as one source for the distortions.

3.3. Two-Stage Amplifier with Glass Compressor

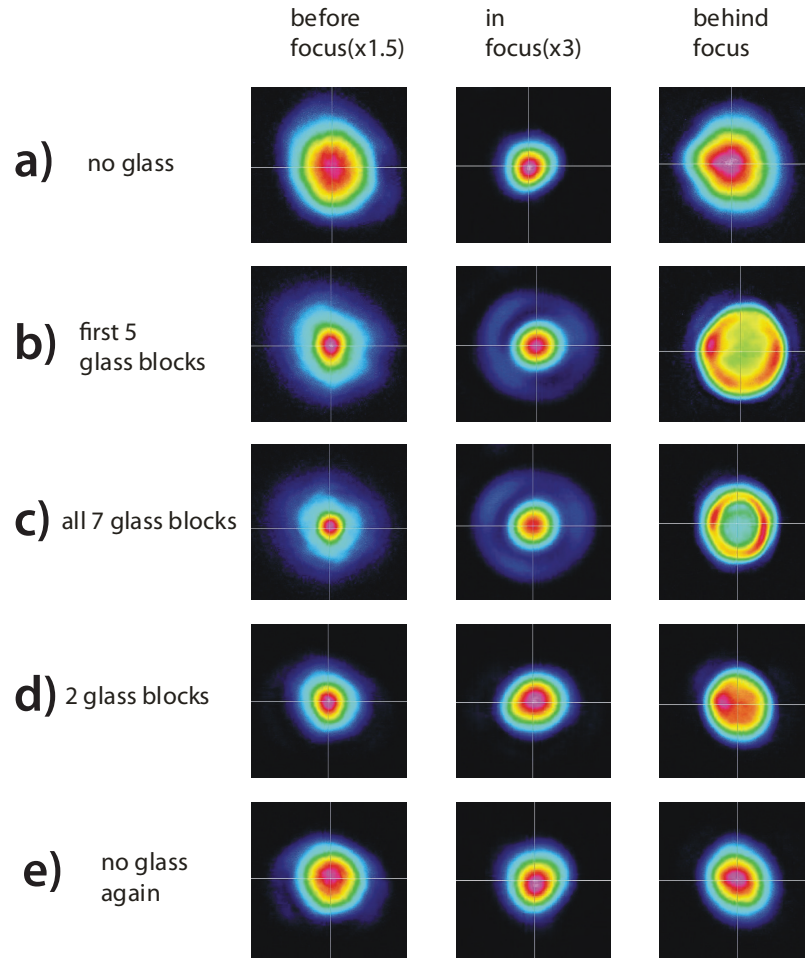


Figure 3.17: The glass blocks lead to a self-focusing pulse wavefront, which makes it difficult to couple this beam efficiently to the hollow core fiber.

in Fig. 3.16 show multiple situations: a) is normal usage meaning the beam is amplified and compressed, b) not amplified, c) bypassed the second amplifier stage but sent through the compressor, d) is like b) but with all the glass removed from the compressor, e) goes even further by bypassing the compressor, telescopes and glass blocks, completely and at f) a lens telescope replaced the first mirror telescope to expand the beam. e) and f) show nicely that without amplification and not using this compressor at all the focus quality is quite good. However, compressed a)–c) the beam is inhomogeneous and has a non-Gaussian beam profile especially before the focus and neither amplification nor bypassing the crystal chamber show a huge difference, so the main degradation of the beam profile has to occur in the compressor after amplification. A comparison of d) and f) shows that the spherical optics in the telescopes are partially responsible and the comparison of a)–c) with d) indicates

a problem with the glass blocks.

The glass blocks were characterized interferometrically and all of them show a small convex spherical deviation, but some have higher order distortions as well so the four best candidates were selected for further use. The results of several surface measurements of the glass blocks are shown in Appendix B. The spherical optics in the telescopes which are used to expand the beam from 4 mm to 5 cm for the glass block transmission and afterwards adjust the size suitable for one inch optics, were checked one by one and a one inch optic and both three inch optics were replaced or substituted. With the new configuration the focus looked much better so testing with full power was the next step. The measurement was conducted with 14 W of power. In Fig. 3.17 a similar measurement as in Fig. 3.16 is shown. The uncompressed pulses without any glass blocks in a) and e) show a very nice focus, but with increasing amounts of material and decreasing pulse duration clear self-focusing of the beam becomes visible. Although the B integral (Eq. 3.1) is well below 1 cf. [45] the effect seems to be very strong. The only option is to reduce the intensity which in this case only leaves the option for bigger beam size which requires new and bigger glass blocks.

When there is self-focusing one can also expect SPM. As the pulse is negatively chirped SPM reduces the spectral bandwidth. To reduce SPM we used four reflections on positively chirped dielectric mirrors, each reflection $+150 \text{ fs}^2$ (PD70), directly after the glass blocks, which confined the spectrally visible SPM to the lens before the HCF and the air before the entrance window to the HCF-setup.

Considering that the usage of the second stage without focusing optics and the stretcher-compressor setup caused quite a few challenges and that despite all efforts the target parameters (1.5 mJ sub-5 fs) of the systems were still out of reach the decision was made to use a different configuration to reach said parameters.

3.4 Two-Stage Amplifier with Transmission Grating Compressor

As presented in the previous section the problems with the negative dispersion setup were so severe that the decision was made to try a different setup to achieve the target parameters. The main issues were the coupled alignment of the passes in the second stage which made it very difficult to optimize the beam size for each pass and the unavoidable self-focusing in the glass block compressor even with reduced

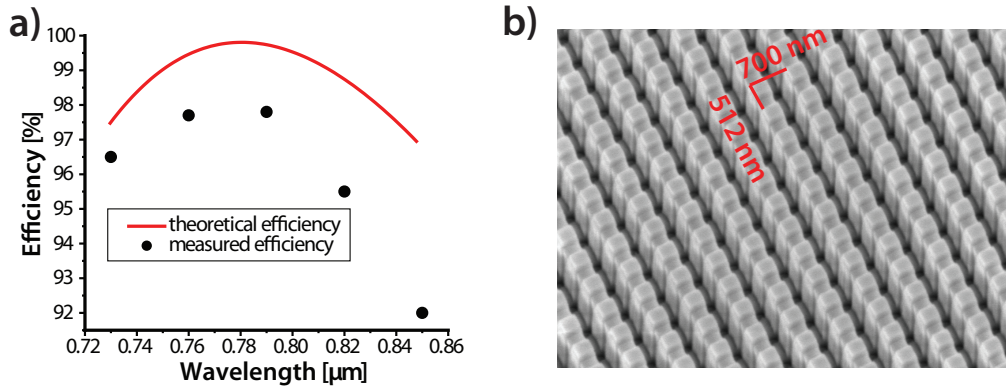


Figure 3.18: The one-pass efficiency of the transmission-gratings is plotted in a) and a scanning electron microscope picture of the grating is shown in b). Both measurements are provided by the Fraunhofer Institute of Applied Optics.

laser power. Naturally, the compressor should be as efficient as possible and the only suitable alternative to the glass blocks is a transmission grating compressor. In the past years the development of transmission gratings led to more efficient broadband versions [71]. However, the dispersion introduced by a grating is quite different from material dispersion as the amount of higher order dispersion is relatively high. The natural solution is to use a grating stretcher and compressor so they almost cancel each other's higher order dispersion (Öffner-type stretcher) but a solution without a second grating pair was preferred.

Alternatively, using a glass stretcher and the Dazzler for the higher orders is an option, but even with an upgraded version of the Dazzler, from WB800 to HR800 which doubles its phase capabilities, the stretching-compression is roughly limited to 17 ps, as for a longer pulse the Dazzler cannot compensate the third and fourth order dispersion. This is a bit shorter than before but as it was also planned to use a spherical optic in each pass of the second amplifier to keep the seed size at 1 mm for each pass the damage threshold should be very similar to the previous configuration.

Transmission-Gratings

The transmission gratings were produced by the Fraunhofer Institute for Applied Optics. The grating period is $0.700 \mu\text{m}$ (1428 lines/mm) and the angle of incidence is 34.353° which is very close to the Littrow angle. The backsides are anti-reflection coated and a second grating structure is used to reduce the losses on the grating side by reducing the diffraction into other orders. The theoretical transmission as well as a few measured points are shown in Fig. 3.18 a). The theoretical curve

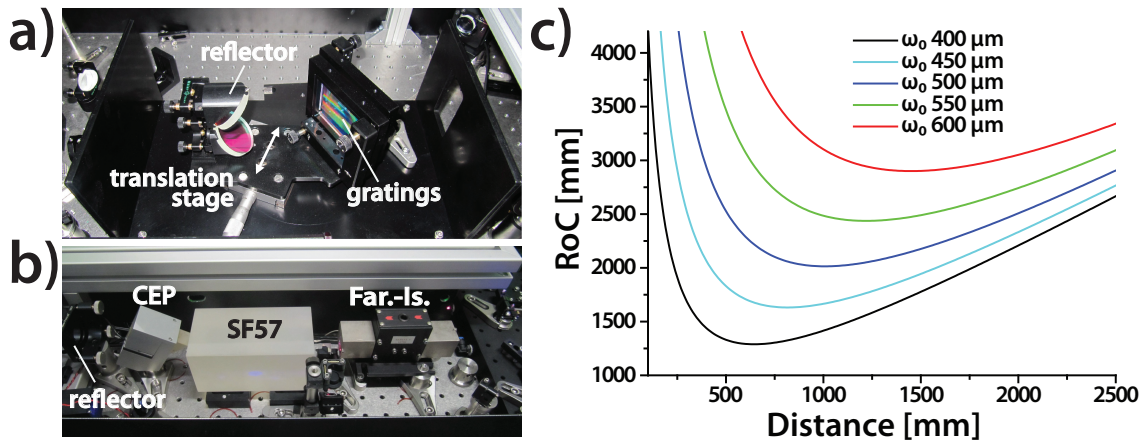


Figure 3.19: Photos of the transmission grating compressor a) and the new stretcher b). The wavefront curvature of a Gaussian beam for different sizes is shown dependent on the distance to the focus in c). The possible distance in the setup for spherical optics is 0.7 to 1.0 m from the focus.

claims a one pass efficiency of 97% or more over the full bandwidth of the laser. The measured values are of course a bit lower and the whole curve is shifted a bit to the blue, but the overall efficiency is still good regarding the bandwidth of the laser spectrum. Considering a measured spectrum (positive dispersion setup) and the measured values for single pass transmission the 4 pass transmission through the grating compressor should be above 86%. In Fig. 3.18 b) is a SEM picture of the grating surface. The 700 nm diffraction grating goes from left to right and the efficiency improving grating (512 nm) from top to bottom. These data and the picture were provided by the Fraunhofer institute.

Glass Stretcher

To stretch the pulses from a few fs to 17 ps, SF57 glass blocks are used because of their high dispersion. One of the big 135 mm blocks from the old compressor plus a wedged glass block pair whose optical path length can be adjusted by a piezo were used. The latter serves as the new slow loop control (CEP) and was purchased from Femtolasers. Two passes through these three glass blocks form the stretcher. All the other dispersive optics along the way contribute slightly to the stretching as well. The new stretcher fits in the same place as the grism and a picture of it is shown in Fig. 3.19 b).

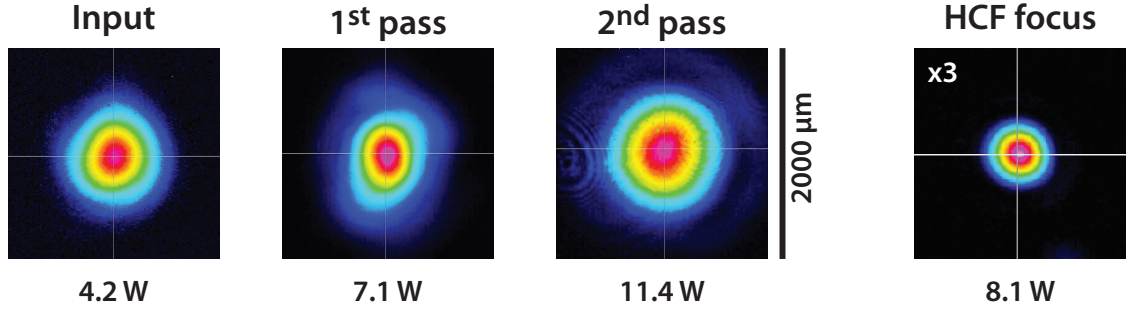


Figure 3.20: Measured beam-profiles and the measured power for each pass are presented. Beam-profiles are measured at the crystal position thus the next pass. The attenuated and magnified focus after compression and the total power in front of the HCF is shown on the right side.

Focusing Optics for the Second-Stage Amplifier

In the first, negative dispersion setup, one of the main drawbacks was the lack of possibilities to modify and adjust the beam sizes of each pass individually which made aligning the second stage very unsatisfying as the end result was always a compromise between the passes. As a solution, spherical focusing mirrors with a similar coating as the high reflectors in the second stage were ordered and installed in each pass. As these mirrors have to be placed near the Rayleigh range

$$z_R = \frac{\pi\omega_0^2}{\lambda} \quad ; \quad \left. \begin{array}{l} \omega_0 = 475 \mu\text{m} \\ \lambda = 790 \text{ nm} \end{array} \right\} \implies z_R = 897 \text{ mm}$$

of the beam, it is important to image the focus back into the crystal. The radius of curvature (RoC) has to almost exactly fit to the beam waist in the focus ($2\omega_0$). Placing the mirror a bit closer or farther away has very little influence therefore the RoC has to be chosen carefully. This behavior is illustrated in Fig. 3.19 c). In the end the focal beam size was set to just below 1 mm and the focusing optics with a RoC of $r = 2000$ mm have been installed. Three passes of amplification were used to reach more than 11 W output power. Their beam profiles are shown in Fig. 3.20 and compared to Fig. 3.3 they are more uniform and allow a nicer laser mode after amplification which, in turn, can be coupled more efficiently to the HCF.

There are however still some distortions (not visible here) in the beam which seem to be introduced by the gratings. It is not certain if these are due to the thin substrates and some bending or maybe have something to do with the second grating structure or are a result of the combination of both.

With all these changes a new overview over the setup is shown in Fig. A.6 in the appendix on page 111.

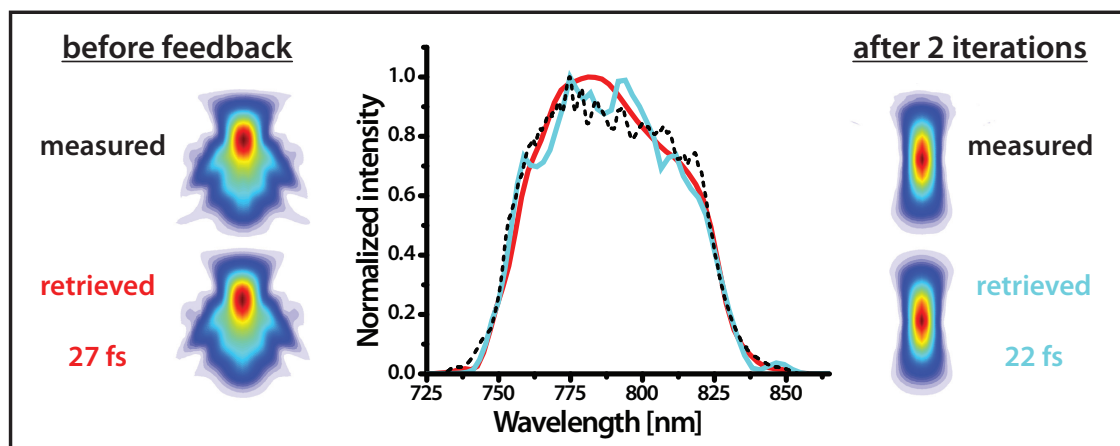


Figure 3.21: Measured and retrieved spectrogram (frequency vertically, delay horizontally) with FWHM pulse duration as well as the measured and retrieved spectra of the SH-FROG are presented. The retrieved phase is fed to the Dazzler for compensation. After two iterations the pulse is nicely compressed.

3.4.1 Amplification & Compression

With the new stretcher the system is positively chirped and the amplified spectrum is shifted back to the red side. Typically the pulses get amplified to 1.1 mJ in the first stage. For the second stage the primary goal is to keep a well-behaved beam so the total amplification is slightly reduced compared to the former setup. After two passes 11.4 W are reached. At 4 kHz this corresponds to almost 3 mJ per pulse. The measured power after each pass and in front of the fiber are also indicated in Fig. 3.20. After a crystal exchange in the second stage, the amplification was a bit lower so three passes were used with slightly different pump power to get close to 3 mJ again. After compression in front of the hollow core fiber the pulses have a bit more than 2 mJ energy and are compressed to 22 fs. A few steps are necessary to get these nicely compressed pulses. After carefully checking the optical alignment of the laser beam into and out of the compressor the grating compressor is fine-tuned by optimizing a nonlinear effect e.g. filamentation in air. By focusing only a fraction of the full power and observing the beam profile, the spectral broadening and the amplitude of the filament's noise at the repetition rate of the laser. The distance between the gratings for the dispersion and asymmetries in the filament hint to

3.4. Two-Stage Amplifier with Transmission Grating Compressor

angular chirp etc. so these can iteratively be optimized. With the calculated higher order values applied by the Dazzler a pulse duration below 40 fs can be reached. Adjusting the polynomial phase values with the Dazzler allows sub-30 fs pulses. Due to the dielectric mirrors and possibly some other unknown sources there are residual higher order distortions which can be addressed via the phase file of the dazzler. With it, an arbitrary phase, within limits, can be imprinted onto the pulses. The best way to use this is to measure the spectral phase of the pulses and use the phase information to precompensate it with the Dazzler.

A second harmonic FROG was used to measure the pulses and extract the phase information. It was fed back to the Dazzler with great success. The measured and retrieved spectrograms, spectra and pulse durations are presented in Fig. 3.21. After two iterations the pulse duration was reduced from 27 to 22 fs. As already mentioned in section 3.3.2 it is difficult to retrieve the full bandwidth of the pulse without using a measured spectrum as marginal correction for the retrieval. And thus using it the retrieved spectra match the input spectrum almost perfectly. Although applying the marginal reduces the retrieval error significantly it has almost no influence on the retrieved pulse duration. The smaller error and increased agreement between the measured and retrieved spectrum raise the confidence in the retrieval and the pulse measurement.

In short, the two-stage Ti:Sapphire amplifier provides phase-stable 22 fs pulses with 2-2.2 mJ energy at 4 kHz repetition rate.

3.4.2 Spectral Broadening

For HHG and other applications a sub-2-cycle laser pulse is required corresponding to a sub-5-fs pulse duration. So the NIR laser pulses are broadened via SPM in an hollow core fiber. So far we only tested a static fiber setup with mixed success. Different hollow core sizes (350/380/400 μm 1.5 m long) were tried in combination with different focal lengths (2000 and 2500 mm). The best result in terms of power transmission with an inner fiber diameter of 380 μm is shown in Fig. 3.22 in black. The transmission is up to 1.5 mJ which makes the throughput efficiency close to 70%. The broadening however is relatively weak on the spectral wings but covers the bandwidth supported by the chirped mirror compressor.

With the 350 μm fiber the achievable throughput is limited to 1.0 mJ but the broadening is significantly better; see red line in the figure. Broadening beyond 400 nm on the blue side is of minor interest for this system as the beam has to be transported

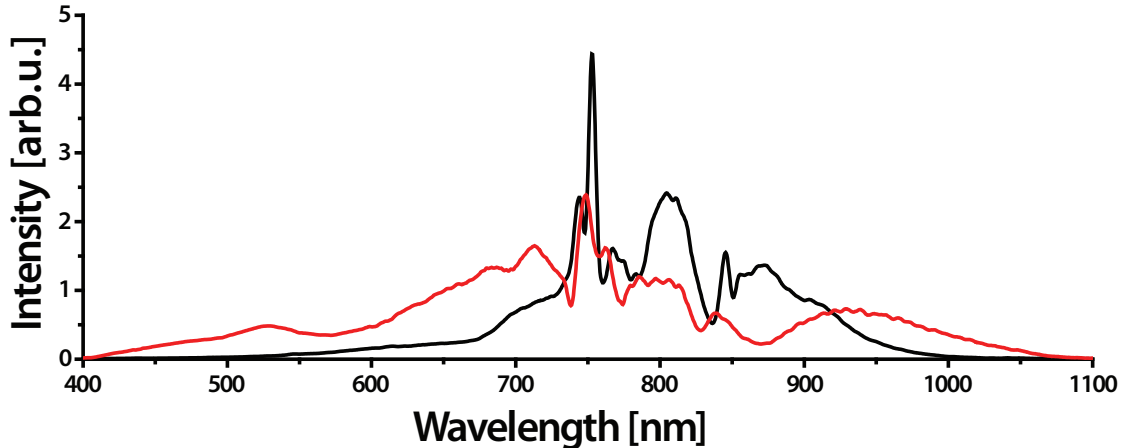


Figure 3.22: Output spectra for two different setups with 2 mJ input energy. In black 1.5 mJ output through 380 μm fiber with slightly chirped input pulse for better transmission and in red 1.0 mJ with compressed pulse and a 350 μm fiber. The neon pressure for both cases is 1.4 bar.

to the experiment with at least 10 metal mirror reflections (usually 14) before the HHG and using aluminum which supports bluer components has too high losses on the infrared side to keep the high pulse energy. However, a spectrum from 400 nm to 1.1 μm with more than 1 mJ is very desirable and should be possible by differentially pumping the fiber in the near future. Broadening more by using higher neon gas pressure does not work as the beam profile gets distorted similar as in Fig. 3.8, which makes the beam unusable for transport and experiments.

3.4.3 Compression and Characterization

The spectrally broadened pulses were compressed with dielectric chirped mirrors which compensate the dispersion of air and glass used for windows and wedges for dispersion control. Different designs were tested and the two sets which were used for experiments are explained in more detail in Appendix C. Both sets allowed compression of the pulses below 5 fs and even below 4 fs under ideal conditions, characterized by attosecond streaking. The efficiency of the chirped mirror compressor plus recollimation with a spherical silver optic is at 80–85 % depending on the white light spectrum. So after white light generation this system provides carrier envelope stabilized sub 5 fs pulses with up to 1.2 mJ pulse energy at a repetition rate of 4 kHz. This corresponds to two and a half times more pulse energy than the conventional one-stage laser system provides.

3.5 One-Stage Amplifier with Transmission Grating Compressor

After setting up the laser system of the previous section the laser was used for HHG and streaking as well as for measurements to study the effects of laser intensities just below damage threshold in fused silica. One part of this measurement studied the transmission of photons between 95 and 115 eV [16] and it proved to be very difficult to shift the cut-off energy of the HHG to this energy without hurting the stability. Thus, the laser was used in a modified setup, bypassing the second amplifier stage. Due to its components the system performed remarkably efficient and was due to its simplicity also very stable.

In order to compensate for bypassing the second stage the first stage was pushed closer to the limit to 1.15 mJ uncompressed output energy. The compression was adjusted, focusing and fiber diameter were reduced to the conventional setup $f = 1.75$ m and $250 \mu\text{m}$ with a length of 1.05 m. With 1.2 bar neon in the fiber a transmission of almost 70 % up to 0.6 mJ of broadened white light was achieved. This is an excellent value and probably mostly due to the better focus the transmission gratings provide compared to the prism compressors used in older versions of the Femtopower laser systems. After the chirped mirror compressor 0.47 mJ of usable pulse energy remained. A broadened spectrum using this setup with 1.4 bar neon is shown in Fig. 3.23 a). This spectrum is optimized for HH counts at 130 eV so the broadening is optimized towards the red side. A slight change of the third order dispersion with the Dazzler would enhance the blue side. The third order dispersion can, to some extent, change the intensity envelope of the pulse asymmetrically and the broadening is proportional to the gradient of the intensity envelope. Thus the broadening can be adjusted in a minor way to favor one side if desired.

The measurement of the vector potential of the compressed pulse, after HHG, is given in b). A scan of XUV-NIR delay over the NIR pulse duration allows the retrieval of the vector potential. For the evaluation the measured electron spectrum at each delay step is fitted with a Gaussian and its center corresponds to the central energy of that delay step. Differentiation results in the black line which represents the electric field of the pulse, or more precisely its component in ToF direction. From the electric field the intensity envelope is easily retrieved via Hilbert transformation. The envelope is plotted in red and the FWHM of the pulse is measured to be 3.9 fs. The overall pulse shape is very good as well. The trailing side of the pulse, at higher

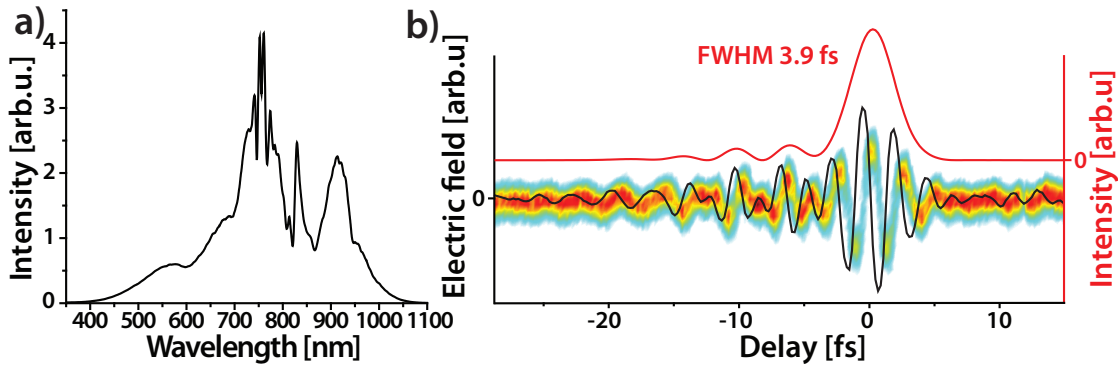


Figure 3.23: Pulse diagnostic of the single stage amplified pulses. The generated broadband spectrum after the HCF is shown in a) and a measured attosecond spectrogram is presented in b). The retrieved electric field is plotted in black and the intensity envelope with an offset in red. The retrieved FWHM pulse duration after HHG is 3.9 fs.

delays, is very clean; the leading side shows some weak pre-pulses resulting from imperfect compression. There seems to be an odd higher-order phase which is not compensated by the mirrors, with the two-stage amplifier the same feature is present but seems to be a bit worse. The chirped mirrors also contribute to the pre-pulses in a different way. With the broad spectrum shown in a) the whole supported bandwidth of the dielectric mirrors is used. As the spectral phase introduced typically deviates from the desired phase long before the reflectivity drops to zero the edges of the reflected spectrum are usually strongly chirped resulting in a weak pedestal. This could be avoided by a narrower spectrum or more broadband mirrors, but both approaches would most likely not result in a better pulse. A narrower spectrum will only support a slightly longer pulse whereas more broadband mirrors make it necessary to use more reflections which increases the amount of accumulated phase errors between the mirrors and the pulse as it is very difficult to match them perfectly.

The stability of the system was very convincing and performing phase stable measurements during daylight hours was common in contrast to other lasers in the same laboratory. Apart from recurring damages of the oscillator's Ti:Sa-crystal and the PPLN-crystal used for CEP-stabilization, which made moving the damaged crystal and small re-optimization of the amplifier necessary, this system was as close to a 'turn-key system' as one can expect it from a 0.5 mJ 4 fs laser system. Of course actually switching the system off and on requires re-thermalization which takes at least half a day. But keeping the system running (unseeded) proved to provide a stable laser source less than an hour after seeding the amplifier. To a lesser degree this applies to the two-stage system of the previous section as well.

3.6 Summary, Discussion and Further Development

In order to increase the output power of the Ti:Sa laser system a second cryogenic cooled amplifier stage was added. Two different dispersion management setups were tested. The first used a grism stretcher and glass block compressor. Although the efficiency of the compressor was, with more than 85 %, very high the beam was distorted by the transmission through the glass blocks and good pulse compression was limited to half the available power. The second setup used a glass stretcher and transmission gratings for compression. The efficiency is comparable and the beam quality after compression was improved by a lot. By fine-tuning the Dazzler, a 3 mJ 22 fs 4 kHz system was set up. The pulses are CE-phase stabilized, broadened and compressed to sub-2-cycle pulse duration with more than 1 mJ pulse energy providing a powerful laser source for nonlinear applications especially HHG and thus attosecond spectroscopy. Quite a few laser systems with more than 1 mJ and a pulse duration with less than 6 fs have been published. Mashiko et al. [72] show a phase stable 1 kHz laser system with 1.2 mJ and 5.6 fs pulses from a CPA stage cooled with liquid nitrogen. A very similar system was presented by Sung et al. [73]. Very recently Jullien et al. [74] presented a contrast cleaned 22 fs 8 mJ Ti:Sa.-laser system at 1 kHz with phase stabilization. If they find an efficient way to broaden this pulse they might be able to generate 4 mJ sub-5 fs pulses soon.

Careful redesign of the stretcher-compressor setup led to mJ pulse energies at a higher repetition of 4 kHz with a pulse quality close to the commonly used 400 μ J laser sources [35]. Although 1 mJ systems with slightly better compression of 3.7 fs [75] have been shown in the meantime this can also be achieved by the laser system presented here if the chirped mirror compression can be pushed closer to the optimum. With minor adjustments the energy of the Ti:sapphire laser can be increased further but a better scalable broadening scheme is needed first in order to be able to use this energy. Differentially pumped hollow core fibers promise an improvement for efficient spectral broadening for higher pulse energies while improving the outgoing mode of the HCF-setup [49, 56]. Differential pumping will be tested and implemented again in the near future promising a more efficient coupling to the fiber which leads to higher transmission and more broadening. Pumping the back side of the fiber will prevent self-focusing which is observable for this pulse energy, the pressure, and the fiber size used in the current setup. The problematic incoupling

and the self-focusing put a limit to the spectral broadening which will be overcome by implementing such a system and a broader spectrum supports shorter pulses.

There are other ideas to generate a gradient in the hollow core fiber e.g. with a temperature gradient [76] along the fiber where a high temperature increases the critical power and thus has a similar effect as decreasing the pressure. While this doesn't consume gas constantly the technical implementation with the high temperatures necessary is not trivial and the time demands for reaching the temperatures after exchanging the gas etc. are very inconvenient as well.

With the new differentially pumped system spectral broadening with mJ energies covering 400–1100 nm will be possible. Such a broad spectrum is not easy to compress with one set of mirrors alone because of the huge bandwidth but with a two channel synthesizer which is already in development it will be possible to get close to 3 fs pulse duration as demonstrated by [55].

On the road to sub-2-cycle laser pulses with even higher pulse energies the biggest challenge is the scalability of the spectral broadening after the CPA. One likely solution is to use non-collinear OPCPA systems instead which broaden the spectrum at the beginning of the amplification chain and use different phase-matching conditions in the amplification stages to preserve the high bandwidth. Using different crystals, phase-matching angles [77] or different pump wavelengths [78] can be used for that purpose. Integrating these approaches into existing high energy systems [79] is the current development of ultrafast OPCPAs. Increasing the average power will follow in time and multi-millijoule sub-2-cycle laser pulses at kHz repetition rate will become available.

But right now CPA systems like the two-stage laser system with the demonstrated parameters are the state of the art sources which allow attosecond spectroscopy at higher photon energies with high photon flux. The next chapter will describe the first applications of the system starting with HHG and streaking as the first step for attosecond experiments.

Chapter 4

First Applications

The development of ultra-short laser pulses and the increasing control over laser pulse parameters grant access to many new phenomena. Predominantly, the high intensities are enabling the use and study of nonlinear effects. Utilizing terawatt, few femtosecond laser pulses in a highly nonlinear process called high-harmonic generation (HHG) converts energy to much higher frequencies, which can be used to form light pulses down to pulse durations of sub-100 attoseconds [36, 80]. These short pulses can be used for pump probe experiments to study ultrafast processes, mostly electron dynamics, with a temporal accuracy down to a few attoseconds [5, 7]. With higher photon energies and flux the study of inner shell electrons and their interactions draw high interest. Solving the course of the (multi-)electron response needs a very high temporal resolution provided by attosecond spectroscopy. An introduction to isolated attosecond pulse generation and characterization is given in Sec. 2.2 and 2.3. The results achieved with the laser systems described in chapter 3 are presented here.

4.1 Experimental HHG

The compressed laser systems described in chapter 3 are sent into a vacuum system to avoid dispersion and are transported to the experimental attosecond setups. The Attosecond-Beamlines (AS) are placed in the room below the laser laboratory. This allows to work on the beamline without the laser running in the same room. It makes a longer beam transport necessary but this can also be used to reach different end stations. So at the moment it is possible to reach three different vacuum setups this way. AS2 is used for atoms and molecules in the gas phase and also for transient

absorption spectroscopy of thin dielectric solids, AS3 is an ultra high vacuum setup for streaking of solids with in-vacuum target preparation etc. and AS4 is currently under reconstruction to utilize the developed ultrashort infrared OPCPA system for attosecond experiments [81] but was previously used for various side projects. The results presented here are all taken at AS2. A schematic of this beamline is shown in App. A.3 and more details can be found in [82, 83]. This beamline is a bit unconventional as the XUV and the driving NIR laser take separated paths and don't propagate collinear from the generation of the XUV to the experiment. The two beams are spatially separated into two arms of an interferometer by perforated mirrors utilizing the smaller divergence of the HHs. This allows e.g. to refocus the NIR laser without influencing the short XUV pulse. The paths have to be interferometrically stable. This setup allows a variety of new experiments. Another big difference is the angle of incidence on the XUV mirror. Whereas in the collinear double-mirror setup spherical mirrors close to zero degree are used, AS2 uses a flat multilayer mirror under 45° or three metallic mirrors with 75° AoI for a very short broadband pulse. The two arms are recombined by a second perforated mirror and then focused by a toroidal mirror with about 1 m focal length which is much longer than in the typical collinear setup.

The high harmonics are generated in the chamber directly before. For focal lengths below $f = 60$ cm the focusing optic can be installed directly in front of the HHG-target for longer focal lengths a flat folding mirror has to be used. The chamber itself would support a bigger distance but the placement of the HHG-target is not very flexible as the focus position is imaged below the time-of-flight detector and this has to work for both arms simultaneously. So changing the HHG-target position significantly demands huge changes further down the beam-path.

The HHG-target consists of a pre-drilled (200–300 μm) stainless steel tube. It can be squeezed before drilling so the interaction length can be modified between 1–3 mm. Typical backing pressures are up to 250 mbar for neon. For higher pressures a differentially pumping stage would be necessary. Using the target with an high power laser widens the hole in the target over time changing the pressure conditions and coats the optics close by with the tube's metals. Thus the targets and the mirrors have to be replaced on a regular basis. As the slow change and replacing the HHG target disrupts experiments pre-drilled ceramic targets with even higher damage threshold are likely to be used in the near future.

For diagnostic purposes of the HH radiation grazing incidence metal mirrors (gold,

nickel) can be moved into the beam before the XUV mirror to either look at the XUV beamprofile, filtered by suitable thin filters, or look at the XUV spectrum via a flat field grating (Hitachi flat-field grating 001-0266). Both are detected by a cooled XUV-CCD camera. The chip is not in the focal plane of the grating and no slit is imaged onto it so the resolution is quite limited, but the whole spectrum is measurable simultaneously. A similar spectrometer is set up properly in the experimental chamber with high spectral resolution.

The CCD camera not only detects XUV photons but also the NIR photons. Therefore the laser has to be suppressed while avoiding too high losses of the XUV. Thin foils of metal are ideal because they reflect the laser. These have to be thin otherwise the absorption of the XUV is too strong and the attenuation becomes too high. The transmission for different materials is plotted in Fig. 4.1. Aluminum and silicon have sharp absorption edges at 73 eV resp. 100 eV which are used as reference to calibrate the spectrum. The next usable material for a sharp edge is boron at 190 eV. On the first filter in the beam-path the laser intensity is still high and some materials are more resistant to the laser than others. Palladium is very good, molybdenum and zirconium are used successfully as well. Metals and other materials which absorb the laser to a higher degree have to be protected by a thin layer of the above mentioned ones or they get destroyed very quickly.

The contents of the HHG-chamber are two motorized mirrors, an iris aperture the

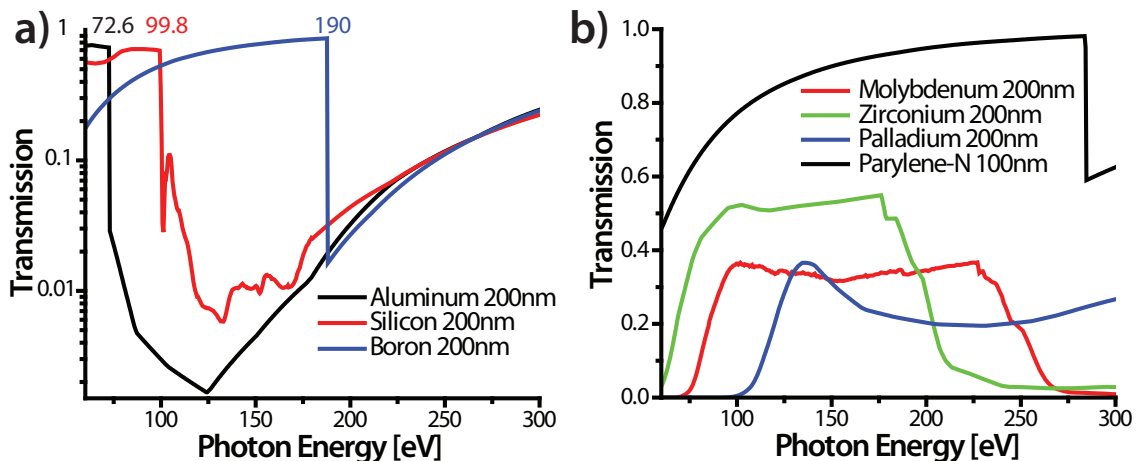


Figure 4.1: The transmission through various thin filters. In a) the XUV transmission of materials with sharp absorption edges used for energy calibration of the spectrometer are shown. The transmission for three commonly used metals for suppression of the IR laser and for Parylene is plotted in b). Parylene (C_3H_8) is often used as a substrate for brittle metals or very thin films. All data is from the Center of X-ray Optics [84].

focusing mirror, eventual folding mirrors and the target on a xyz-translation stage. The parameters to optimize the HHG are the aperture for fine adjustments of the intensity, the translation stage, mostly z, for the optimal positioning of the target. The direction, or the pointing of the XUV beam, has to be reproduced with the mirrors before the HHG target. Else the subsequent interferometer changes causing spatial and temporal mismatches and of course the XUV beam has to be aligned through the small holes in the perforated mirrors.

Laser pulse compression, CE-phase and gas backing pressure are further parameters which influence the HHG.

Ideally the photon flux after the XUV mirror would be optimized, but depending on the XUV optic the count rate might be rather low and it is much more practical to optimize on a faster obtained signal. Optimizing the intensity of the beamprofile on the CCD camera is a good choice provided the observed spectrum fits to the one selected by the mirror. If the observed spectrum contains the much more intense lower order HHs the influence of changes of the above mentioned parameters can be misleading. Also for most of the experiments an isolated attosecond pulse is required.

Observing the XUV spectrum can be used to find the right phase (stabilized CE-phase required) to produce an unmodulated spectrum tuned to the XUV mirror in use and to optimize the photon counts at the same time.

4.1.1 Results

When the two-stage system first started working properly and became usable for HHG, characterization and streaking of broadband XUV spectra were conducted first. A 150 μm thin molybdenum ($>70\text{ eV}$) or palladium filter ($>100\text{ eV}$) were used to suppress the laser and the lower energy pulse train. To keep a broad spectrum three reflections with angle of incidence of 75 degree on rhodium mirrors were used in the interferometer. More details about these mirrors can be found in chapter 4 of [83]. The three reflections combined offer more than 30 % reflectivity for the whole bandwidth from 90 to 140 eV. A multilayer optic can reach these values only close to the silicon edge for a very narrow bandwidth. In the measurement shown in Fig. 4.2 these mirrors and an 150 nm thin molybdenum filter were used for spectral selection. The recorded, background corrected and energy calibrated measurement is shown in a). Depicted is the kinetic energy of the photoelectrons depending on the delay relative to the IR-streaking field. The pulse was retrieved via FROG CRAB

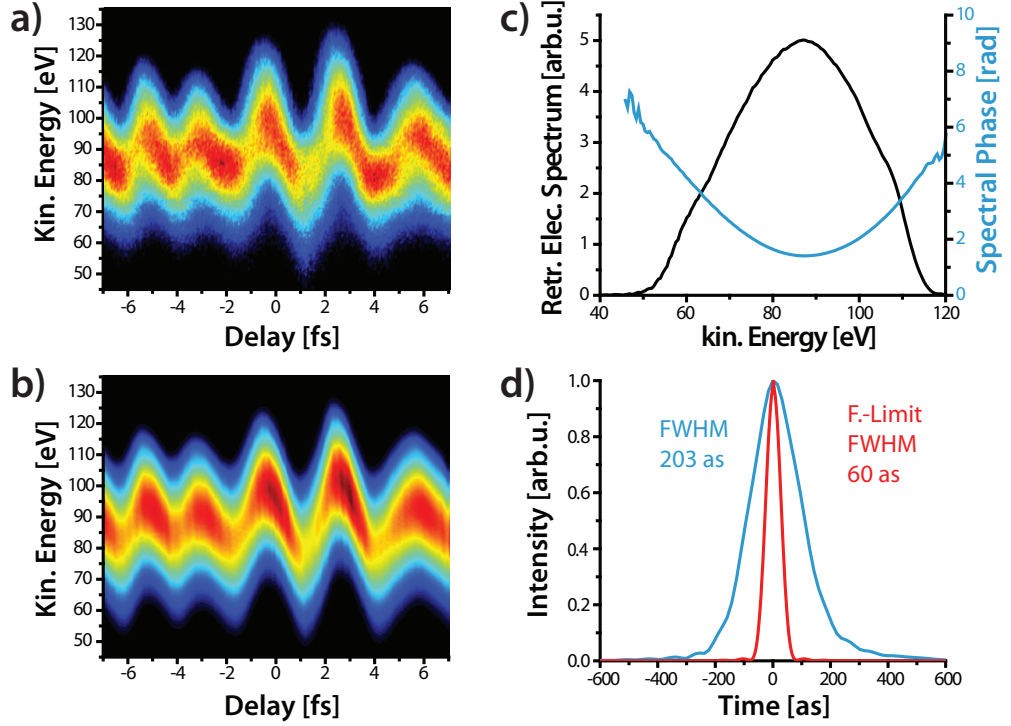


Figure 4.2: Measured broadband XUV streaking trace in a) with rhodium mirrors and 150 nm Mo-filter. The retrieved spectrogram b) and the spectrum and its phase in c) and the temporal pulse shape in d). For comparison the perfectly compressed pulse is shown as well.

(Frequency-Resolved Optical Gating for Complete Reconstruction of Attosecond Bursts) program called AttoGram by J. Gagnon [85]. This FROG like reconstruction retrieved the pulse very well. The trace is shown in b) and the retrieved electron spectrum is plotted in c) along with its phase. Clearly the pulse is not completely compressed but positively chirped. The chirp is due to the attochirp [86] caused by the generation. It is partially compensated by the thin metal filter but it would require more material to compress the pulse closer to its limit at the expense of photon flux. The retrieved pulse duration with 203 as and the Fourier-limit (60 as) of the corresponding XUV spectrum are plotted in d). The kinetic energy is calculated with the measured time of flight of the electrons referenced to time zero defined by the 'light peak' caused by a few photons hitting the MCP.

$$E_{kin} = \frac{m_e l^2}{2(t - t_0)^2}$$

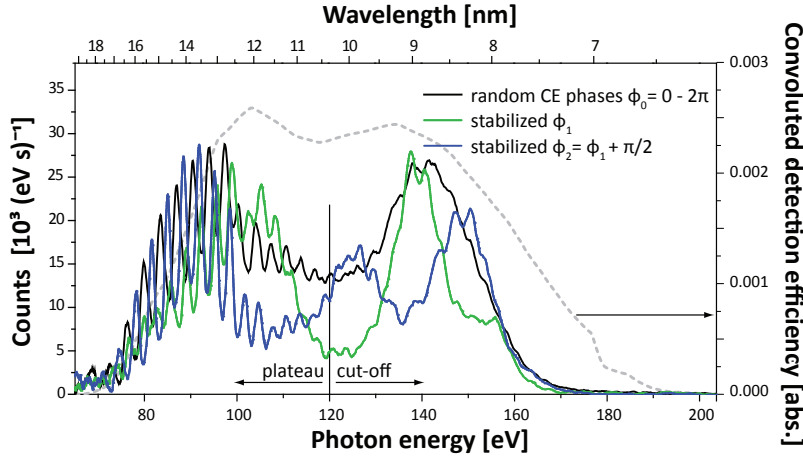


Figure 4.3: Measured XUV photon spectra generated in helium shown in blue and green for different CE-phases and in black unstabilized. The theoretical detection efficiency is given by the dotted line.

l is the length of the drift tube and t the measured time of flight.

The low energy electrons fit perfectly to the Mo-filter shifted by the ionization energy of the used neon gas (21.6 eV for neon-2p electrons). In the just mentioned experiment neon gas was used as HHG target gas and as target for the HHs for streaking. In order to reach higher photon energies helium can be used in the HHG target. The higher ionization energy of helium allows higher intensities and thus leads to higher photon energies see Eq. 2.21. Obviously less ionized electrons generate less HH radiation. So while an increased cut off can be expected the HH-flux will decrease. A measurement of the HH spectrum using helium is shown in Fig. 4.3. Photon energies up to 170 eV were detected with relatively high intensity in the cut-off region of 150 eV [87]. CE-phase effects were strong and clearly visible for the spectra shown here, in contrast to spectra recorded by Ishii et al. [88] at higher photon energies. But as shown in these and other publications [89] helium pressures have to be much higher as neon pressures to work efficiently for HHG. Helium also is more difficult to pump than neon. At kHz repetition rate pulsed nozzles can't be used in pulsed mode like for lower repetition rate high power lasers which makes it very challenging to apply a continuous high helium pressure for a HH-target.

For neon typical backing pressures in the used targets are between 100 and 200 mbar. For helium around 100 mbar was the maximum for stable operation. For a few seconds higher pressures could be applied which showed a quite linear gain of HHs with pressure. Ideal pressure for the setup is at 1.5 bar according to [89]. Without a

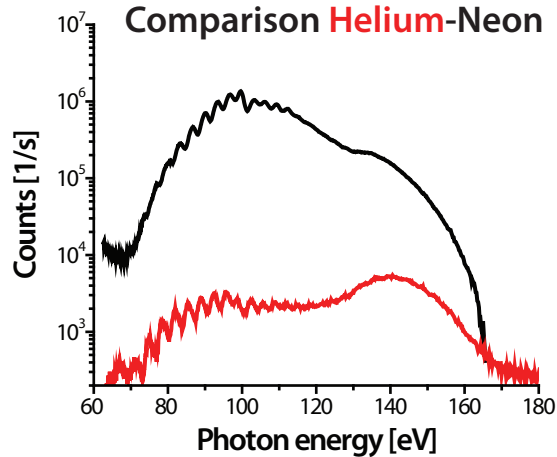


Figure 4.4: Recorded HH spectra for 130 mbar neon (black) and 95 mbar helium (red) produced by a 4.5 fs 600 μ J laser pulse focused with $f=800$ mm, both optimized for highest photon energies detected

decent differentially pumped HH-target helium will not produce the necessary XUV flux for experiments with a multi kHz laser system.

In Fig. 4.4 a comparison between the optimized HH-flux of helium at 95 mbar and neon at 130 mbar is shown spectrally. As expected the helium has relatively more components at higher photon energies but is on average two orders of magnitude below the neon generated HHs. Of course neon is used at optimal pressure conditions, the counts (for more than 120 eV) decrease with higher pressure whereas the helium pressure is far from the optimal value. These results were all obtained with the negative chirped two-stage amplifier setup the following measurements were obtained using the one-stage version using the transmission grating compressor for compression.

HH-Flux

High harmonic generation is not a very efficient process but the experimentally achieved pulse energies are of great interest in order to plan experiments. There are different possibilities to determine the generated photon numbers. The photon flux can be derived by using a photo diode [36, 90]. Alternatively using a CCD camera and recording an XUV spectrum can be used to determine the measured and generated number of photons [91]. The big advantage of this approach is that a spectrally resolved information about the pulse energy is obtained.

Chapter 4. First Applications

In order to do it correctly all steps from the generation to the recorded calibrated spectrum have to be accounted for. In the presented setup the generated XUV-photons get first reflected by a metal mirror then diffracted by a flat field grating and pass through two metal filters of $500\ \mu\text{m}$ zirconium before they get eventually absorbed by the CCD camera. Then the generated charge is converted into counts. For the used CCD camera four electrons generate one count. The number of electrons per photon is photon-energy dependent. For the photon-energies measured one electron per $3.65\ \text{eV}$ photon-energy is generated [92]. The detection efficiency of the chip is, according to the supplier, roughly 45 % in the energy range between 50 and 150 eV. The grating efficiency is around 20 % [83] and the transmission curves for the filters are taken from the center of x-ray optics [84] as is the reflectivity for the metal mirror with an angle of incidence of 80 degrees. Using all this information leads to Fig. 4.5 a) where the pulse energy per eV is plotted. For the energy range from 110 to 130 eV 5.5 pJ are evaluated. As ideal transmission and reflectivity of the optics were used for the correction this might underestimate the real value a bit as the metal surfaces age and get contaminated or even altered by the beam itself over time which causes higher losses which has been observed in the laboratory. The beam profile depicted in Fig. 4.5 a) was taken with a palladium filter, thus only the photons above 100 eV are transmitted. The central energy is at 120 eV. It shows a remarkably nice XUV-beam profile which is almost perfectly round. The size can easily be estimated by the shadow given by the hole of the perforated mirror. The hole is 2 mm in diameter which makes the beam's $1/e^2$ about 0.5 mm. The mirror is placed one meter behind the high harmonic generation target. Thus the divergence

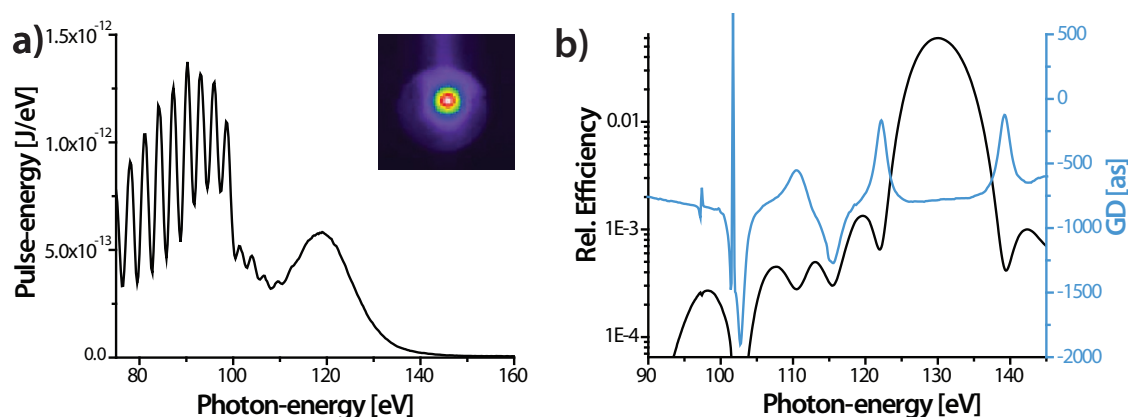


Figure 4.5: The measured and back-calculated generated photon flux is plotted in a). The beamprofile for 100–150 eV is shown as well. In b) the theoretical reflectivity and phase of the XUV multilayer mirror used in this thesis are plotted.

angle is

$$\theta_{div} = \arctan \frac{\omega(z)}{z} \approx \frac{\omega(z)}{z} = 2.5 \cdot 10^{-4}$$

with ω the beam waist radius and z the distance from the focus. For an ideal Gaussian beam this means the diameter of the generating volume is $28 \mu\text{m}$. The beam diameter of the driving NIR laser was measured to be bit more than twice as big. This small divergence reduces the losses at the hole of the second perforated mirror because less photons are clipped by this aperture. This is crucial for experiments, at this beam-line, which need a high XUV photon flux.

Small distortions in the beam quality of the driving laser e.g. a small astigmatism is passed on to the profile of the HHs. For higher harmonics the distortions become increasingly worse. So keeping the beam well behaved is of paramount importance e.g. any distortions of the flat and spherical mirrors have to be avoided e.g. caused by too tight set screws in mirror mounts. The high amount of optics in vacuum chambers, some of which are difficult to inspect, especially the turning mirrors in the cubes, makes it sometimes difficult to detect a bad or damaged optical component.

130 eV Streakings

As shown in Fig. 4.5 a) the CE-phase stabilized laser generates a reasonable photon flux above 120 eV photon energy. Some experiments prefer higher photon energies as it reduces the electron background in the region of interest due to above threshold ionization caused by an intense laser field. The XUV mirror design is shown in Fig. 4.5 b). The mirror works under 45 degrees angle of incidence and is designed in combination with a $150 \mu\text{m}$ palladium filter. Together they have 6% efficiency at 130 eV and a FWHM bandwidth of 7.6 eV supporting a pulse duration just below 330 as.

Ionization Gating in HHG

With the development of ultra short laser pulses with more and more pulse energy isolated attosecond pulses have been generated by different techniques. For longer driving pulses gating techniques, typically with polarization [93], have been used. Nature itself helps out with isolated attosecond pulse generation via ionization gating, which, in short, means that the ionization of the plasma affects the phase matching of the high harmonic generation such that the later half-cycles don't or

hardly contribute to the harmonics. More details about ionization gating can be found in Abel et al. [94]. Two instructive figures from said paper are shown in Fig. 4.6. In a) the classic attosecond pulse train generation is illustrated and in b) the ionization gating case. With higher intensities it grants a bigger difference in cut-off energies of the HH-generating half-cycles than the classic case. A simulation for their 8 femtosecond pulse is shown in c). The ionization rate is dashed in red, the phase matching for the cut-off energies is dotted in blue and the time dependence of trajectories actually producing these photon energies are plotted in black. So the amplitude of the generated photon energies can be affected severely by ionization. For HHG at very high intensities ionization gating is crucial to understand the generated attosecond pulses [90]. A recent study provides experimental insight into the exact effect of ionization from pulse to pulse in an attosecond pulse train [95].

In the following a few measurements are presented which show that ionization gating plays an important role in the HHG process with the laser parameters used and described in section 3.5.

Fig. 4.7 a) shows a calibrated streaking spectrogram using the 130 eV mirror from Fig. 4.5 b). This streaking is taken with neon gas so the ionization energy is $E_{2p} = 21.6$ eV for the 2p electrons and $E_{2s} = 48.5$ eV for the 2s electrons. The 2s line is always weaker than the 2p line due to a lower XUV cross section and the photoemission distribution. In this spectrogram it is barely visible and hidden in the noise. The main characteristic of this streaking is that it shows two streaked attosecond pulses. The whole spectrogram is a bit noisy but there is no contribution

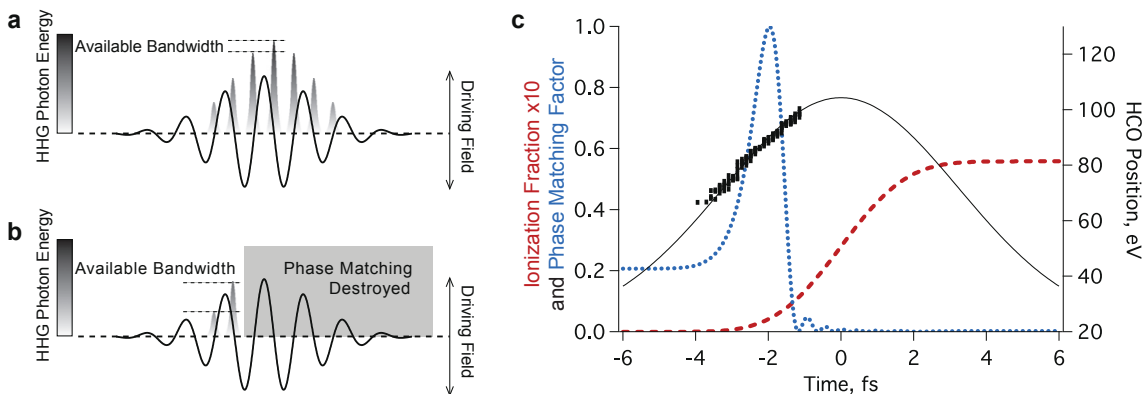


Figure 4.6: The generation of XUV attosecond pulse trains and the isolated attosecond bandwidth is shown in a) and b) without and with the effect of ionization gating for very intense laser pulses. The influence of ionization for an 8 fs pulse on the phase matching and XUV generation is plotted in c). All plots are taken with permission from [94].

of a third pulse visible in this spectral range. While the 110 eV line is very clean the two lines at lower energy are not isolated. There is a small contribution of the 2s electrons corresponding to the higher photon energy line. The XUV photons forming this line don't have as good contrast as the designed reflectivity at 130 eV which causes a weak, broad pedestal. If there are different attosecond pulses contributing to this spectral range they are considerably less intense than the main line.

The lower lines compared to the main line are shifted to earlier delays by approximately a half-cycle which suggests that they are formed by an XUV-pulse generated in the previous half-cycle of the driving laser than the main line. Looking at the mirror reflectivity in Fig. 4.5 b) it is remarkable to see any photo electrons at 80-90 eV as the attenuation should be almost two orders of magnitude. Unfortunately there is no recorded photon spectrum corresponding to this measurement but a relative long integration time and the signal to noise level of the streaking indicate that the photon flux at 130 eV was probably a factor of 5 less than in Fig. 4.5 a). So a bit more than one order of magnitude is accounted for the remaining difference has to be caused by differences between the design curve and the realized version of the mirror.

In order to evaluate the spectrogram the FROG CRAB program 'AttoGram' [85] was used. As the main interest lies in the lines the background was generously subtracted shown in Fig. 4.7 b). The reconstruction has difficulties with overlapping streaked pulses [96] as the expected interference pattern is not resolved in the measurement. So avoiding overlap makes the retrieval more reliable.

The reconstruction works nicely in this case and is plotted in c). The retrieved temporal structure of the pulses is presented in part d) of the same figure. The temporal separation between the pulses is retrieved to be $1.25 \text{ fs} \pm 0.1 \text{ fs}$ which fits perfectly to the half-cycle time of the central wavelength of the NIR laser pulse of 750 nm ($750 \text{ nm} \cdot c^{-1} / 2 = 1.25 \text{ fs}$). Please note that lower time values correspond to an earlier arrival time for the XUV. The retrieved spectrum and its group delay are shown in the final part e). Comparing the retrieved GD with the mirror plus filter design in Fig. 4.5 b) shows good agreement. The measurement retrieves an additional shift of 1250 as between the spectrum of the two pulses which is due to the pulses being generated at consecutive half-cycles and is not caused by the optics or the nonlinear medium involved. Also the design shows a strong change at the lanthanum edges at 102 and 105 eV which are not resolved in the measurement.

In short, this measurement demonstrates the existence of two spectrally separated

attosecond XUV pulses from two consecutive half-cycles of the driving laser field without any sign of other half cycles generating comparable harmonic counts in this spectral range and corroborates the excellence of the streaking technique.

Usually one would expect the half cycle following the half cycle generating the highest harmonics to have a similar spectrum as the one before. The measurement shows that it has if any a low contribution. So either the electric field strength is lower and/or the phase matching conditions have changed. As the CE-phase was optimized for the 130 eV photons and with the generating pulse being 4.5 fs long the half cycle before and after the main half cycle are quite similar in electric field strength thus the cause has to be the phase matching.

If the changing phase matching conditions caused by ionization are taken into account the experimental data is explainable. The increasing plasma density changes the phase matching in favor of higher photon energies. However the electric field strength has also to fit to the phase matching in order to generate high harmonics. As the laser parameters are typically optimized for the cut-off region, in this case the 130 eV, we can assume that the phase matching with the available pulse is close to optimal at the main half cycle. As there will be more plasma for the following half-cycle the optimal phase matching conditions will be shifted to higher photon energies but the field strength is not high enough to reach those, thus hardly any XUV is generated compared to the half-cycle before the main half-cycle for which the phase matching is sub-optimal for high energies but ideal to generate photons at slightly lower energies. In a similar way ionization gating also allows isolated attosecond pulse generation with longer driving laser pulses [93, 97].

4.1.2 Pulse Characterization by Attosecond Streaking

The following experiments demonstrate nicely the capabilities of attosecond streaking for pulse characterization even for a bit unusual cases. The first experiment was conducted with the second stage amplifier and the transmission grating compressor resulting in more than twice the pulse energy and marginally longer pulse duration for the high harmonic generating pulse. The XUV mirror used was the same 130 eV mirror as in the previous experiment. In order to adjust for the higher pulse energy of the driving laser the focal length for HHG was increased to one meter. The available pulse energy could support longer focal lengths and still produce harmonic radiation at 130 eV but the dimensions of the chamber and alignment considera-

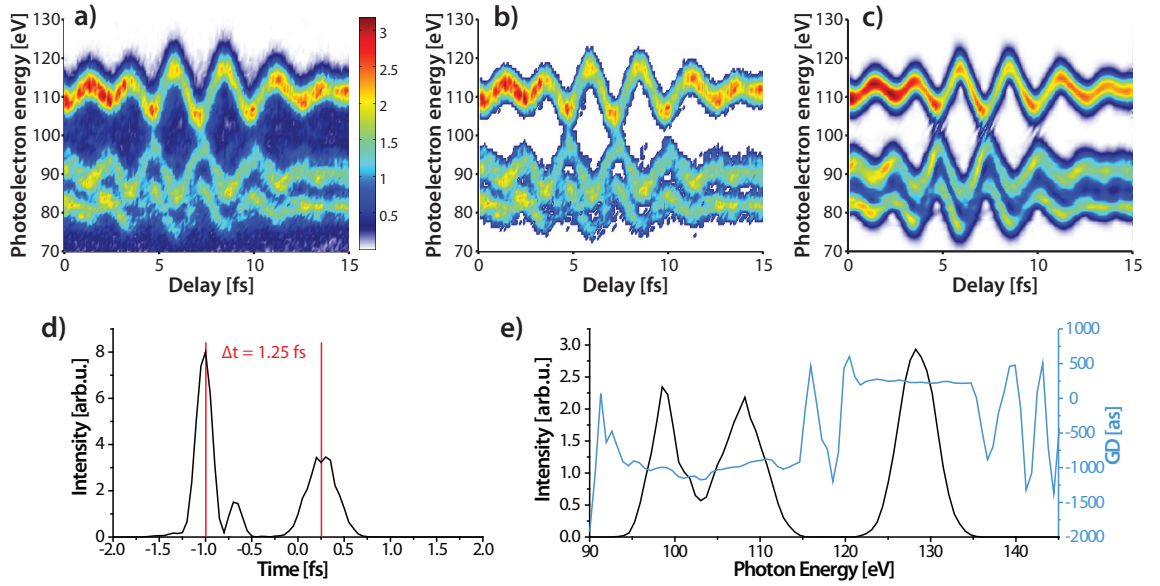


Figure 4.7: Evaluation of a streaking spectrogram. The calibrated measured photoelectron spectrogram is shown in a). A spectrogram reduced to values above 0.7 is shown in b) and its FROG CRAB reconstructed pendant in c). The retrieved temporal structure shows exactly a half-cycle difference between the two pulses. The retrieved photoelectron spectrum corrected by the ionization energy of neon resulting in the XUV photon spectrum and its retrieved group delay are plotted in e).

tions in the delay chamber prevented extensive reconstructions. The used pulse energy was adjusted by an iris aperture in the HHG chamber for optimal cut-off high harmonics. About 20% of the energy were lost that way, but it preserves the possibility to increase the intensity in case the pulse duration is longer as usual. For this focal length $\approx 600 \mu\text{J}$ pulse energy appeared to be optimal for HHG at 130 eV with a sub-5 fs pulse. The applied neon pressures at the gas target varied between 130–160 mbar which is almost half of the optimal pressure for 100 eV photons. In this experiment, Fig. 4.8, the influence of chirp on the HHG in the ionizing gating regime is illustrated. After the common procedure to optimize XUV photon flux at 130 eV by optimizing alignment, target position, pulse energy, neon pressure and CE-phase the streaking spectrogram a) was recorded. It shows a nice Ne-2p line at 108 eV amplified by the time of flight lens and a weak 2s-line at approximately 85 eV. The pulse is astonishingly long to generate an isolated attosecond pulse at 130 eV. Below the electric field of the pulse and the corresponding intensity envelope are plotted. The peak of a Gaussian fit for each delay step extracts the vector potential of the laser pulse. Slight smoothing and differentiation result in the plotted electric field. The single delay step at 18 fs delay with the unstable CE-phase was ignored

Chapter 4. First Applications

for the fit. The intensity envelope is given by the square of the Hilbert transform of the electric field. There is no dispersive component in the beam path of the laser only six silver mirror reflections thus the pulse is unchanged after the HHG. The pulse has a double peak structure and a FWHM of 11.5 fs and is strongly positively chirped (low frequencies first). The amount of glass in the beam path was reduced for b) and even further for c) to obtain an unchirped pulse. In each step the HHG at 130 eV was optimized again by testing and adjusting all parameters mentioned above. The measured pulse in b) shows with 4.7 fs the smallest FWHM but has a small prepulse caused by residual third order dispersion. The pulse in c) is slightly longer with an apparently better pulse shape. The streaking amplitude is controlled by an aperture and adjusted for these measurements so the streaking amplitudes can not be compared to each other. However, the photoelectron counts are normalized to acquisition time and can be compared. Therefore a) has almost double the counts of c) and about 50% more than b). The longer, chirped pulse generates a stronger isolated attosecond pulse at the photon energy of 130 eV. This behavior is qualitatively reproducible on most days, although quantitatively it is usually less than presented here.

For all three cases, 130 eV photons were generated in the last phase-matched peak of the spectrum, so in the classic picture it would be the cut-off region. Considering

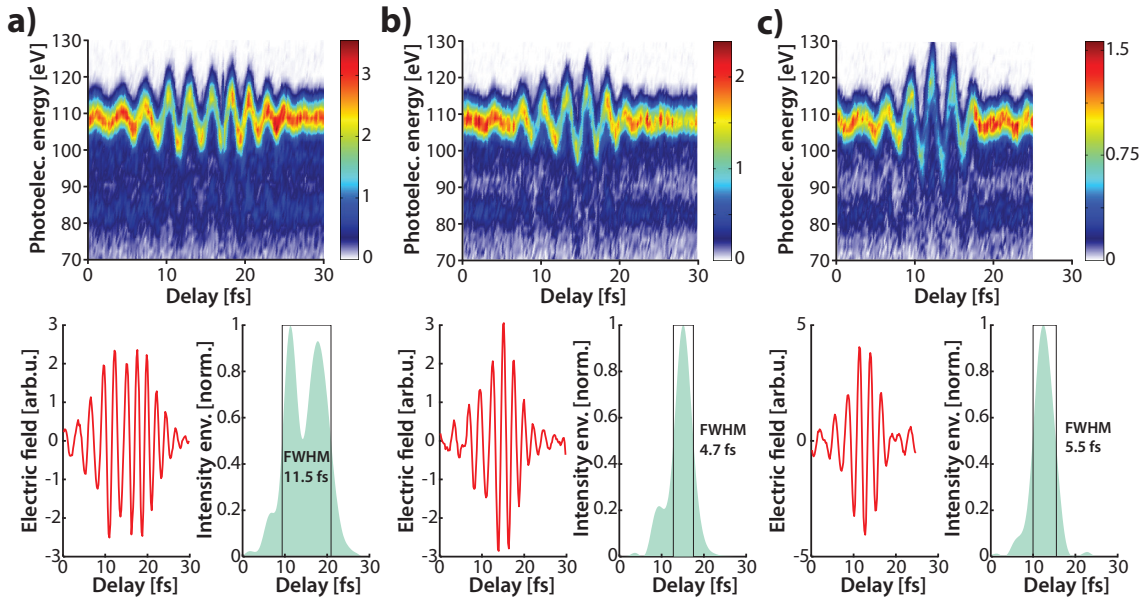


Figure 4.8: Three, in dispersion varied, pulses optimized for XUV generation at 130 eV and their streaking measurements are presented. Please note while the chirp is reduced going from a) to c) the achieved electron count rate decreases.

ionization in the HHG as shown in Fig. 4.6 c) the final amplitude depends strongly on ionization. The positively chirped pulse ionizes less at the same electric field amplitude and can in HHG reach higher photon energies at lower field strengths. Thus it is obvious that for the highest harmonics positive chirp is much better than negative chirp. The latter should be efficient in the generation of lower high harmonics though.

In conclusion we have demonstrated HHG with a 4 kHz millijoule sub-5 fs laser system. Using long focal lengths of 80–100 cm photon energies up to 170 eV were generated. The photon flux and photon energy are improved compared to the one-stage system. The number of generated XUV photons generated each pulse in neon was measured in a spectrally resolved way resulting in 5.5 pJ between 110 and 130 eV. The possibility to study the phase of electron wave-packets via attosecond streaking has been demonstrated for a streaking measurement featuring two spectrally separated attosecond XUV-pulses from two consecutive half-cycles of the driving laser field. The influence of ionization gating on HHG has been shown experimentally by generating isolated attosecond pulses at 130 eV with a chirped 12 fs driving laser without using any additional gating.

4.2 Probing the Giant Resonance of Xenon with Broadband XUV-Pulses

The attosecond streaking technique has become an important tool to investigate ultrafast electron correlations and processes. Delay studies of different energy levels of gases or solids provided experimental data to test and discard theoretical models of these processes [5, 7, 98]. The next natural step is to study more complex systems e.g. molecules instead of gas atoms or heavier atoms with more electrons and more electron interactions. In the photon energy range available, xenon is a promising system. Xenon has a strong 'giant resonance' at 100 eV photon energy for ionizing 4d-electrons. These electrons come from a full inner shell of the xenon atoms and are emitted into the continuum via meta-stable bound states. This potential barrier also called shape resonance is caused by the effective potential dominated by the coulomb force and angular momentum. Additional to these single electron effects strong sub-shell interactions are to be found at the giant resonance. This resonance has been a test case for many theories and its response is well studied [99, 100]. However, the temporal behavior of the response is experimentally challenging. Attosecond streaking provides a unique tool to characterize the electron wave-packet with attosecond resolution and thus is able to provide experimental data to test against the existing theoretic models.

4.2.1 Simulation of the Giant Resonance Response

In a simple model the photo-emission from the 4d level of xenon can be represented by a shape resonance which is schematically shown in Fig. 4.9 a). For photon energies which exceed the ionization energy of the 4d level the excited electron doesn't become a free electron right away but is first excited into a meta-stable bound state, trapped by the effective potential of the atom. In case of xenon these states have very short life times and the electron tunnels through the barrier almost immediately. For electrons with low kinetic energy the delay is high, but experimentally electrons with low kinetic energies are harder to distinguish because there are many other sources for low energetic electrons in a streaking experiment. At 15 eV of kinetic energy theoretic calculations of xenon by A. Kheifets [101] predict that the delay is already sub-100 as. He used random phase approximation with exchange (RPA) to model the response of xenon and the model shows good agreement with the measured partial cross sections measured for xenon. The goal of this experiment

4.2. Giant Resonance of Xenon Probed by Broadband XUV-Pulses

however is to test the temporal behavior of the photo-emission.

The shape resonance causes an energy dependent delay of the photoelectrons which means the free electron starts to feel the IR streaking field with this small delay. This results in a chirped electron wave packet similarly as if the XUV pulse was chirped with a corresponding phase. Dr. Kheifets was so kind to share his retrieved dipole matrix elements with us for simulations to investigate their effect on the phase of the electron wave packet.

In order to see whether the used reconstruction algorithm can resolve the change caused by the emission delay caused by the shape resonance a 100 as XUV pulse with flat phase is compared to a similar XUV-pulse with the phase calculated from the matrix elements. The results of these reconstructions are shown in Fig. 4.9 b). The reconstructed photoelectron spectrum is plotted in black and the retrieved phase respectively the group delay dispersion (GDD) of the wave packet is plotted in blue. The retrieval of the perfectly compressed wave-packet is plotted with a dashed line, the retrieved phase of the XUV-pulse with the phase-imprint of the xenon dipole matrix elements is plotted with the continuous line and the theoretical GDD itself is given by the dotted line. Analyzing the retrieved phases, it is obvious that only the central part of the spectrum is retrieved well because the oscillations of the GDD on the wings of the spectrum become very large and are artifacts of the retrieval. The averaged phase however seems to be still correct.

The dashed line, which should be a constant zero value, is in fact retrieved well. It is less than 100 as^2 off in the central spectrum. There is a tendency to lower GDD values for lower kinetic energies which seems to be an error of the retrieval. This might also be caused by imperfect normalization and interpolation of the input trace, but this can be taken as an example which precision of the reconstruction can be expected for any trace under ideal circumstances.

The reconstruction of the RPA calculated phase is in good agreement with the input value as well. The GDD values are slightly shifted to positive values but the gradient is reconstructed very well. The erroneous tendency of the first reconstruction seems to be slightly stronger here, but as the direction is the same, the difference of the two retrievals is actually closer to the theoretically predicted difference.

The conclusion from comparing the theoretical traces is that the reconstruction can resolve the phase-difference under ideal circumstances within $200\text{--}300 \text{ as}^2$, but also that the phase effect to be measured, the dotted line, is not substantial.

4.2.2 Experimental Setup

The experiment aims to reconstruct the imprint of the effective potential of the giant resonance onto the electron wave-packet. First, a broadband isolated XUV pulse in the range of 70 to 110 eV is required and a reference electron wave-packet has to be recorded, the difference between the reference and the probed system, xenon, is caused by its electron emission process. The result has then to be compared with the theoretical prediction.

The laser used was the first two-stage setup using a glass compressor (chapter 3.3). The experiment was conducted in the AS-2 beam-line, illustrated in App. A.3. In order to get the necessary isolated attosecond pulse the focal length was set to 80 cm and molybdenum was used as filter to suppress the laser light and the rhodium mirror set provided high efficiency for the remaining XUV spectrum. The combined reflectivity is more than 34 % from 80–130 eV for the whole bandwidth and more than 50 % at 110 eV [82].

For the reference several streaking measurements of neon were recorded and evaluated with AttoGram. Due to the large bandwidth of the pulse the recorded photoelectron spectra were carefully corrected for the lens transmission function for the applied voltage as well as the recorded time of flight due to acceleration by the electronic lens. The retrieved photoelectron spectrum and its group delay dispersion (GDD) are plotted in Fig. 4.10 a). The FWHM of the spectrum is 26 eV and the pulse duration with the retrieved phase is ≈ 125 as. The error bars on the spectrum are due to the statistical error of the reconstruction of three retrievals each on two,

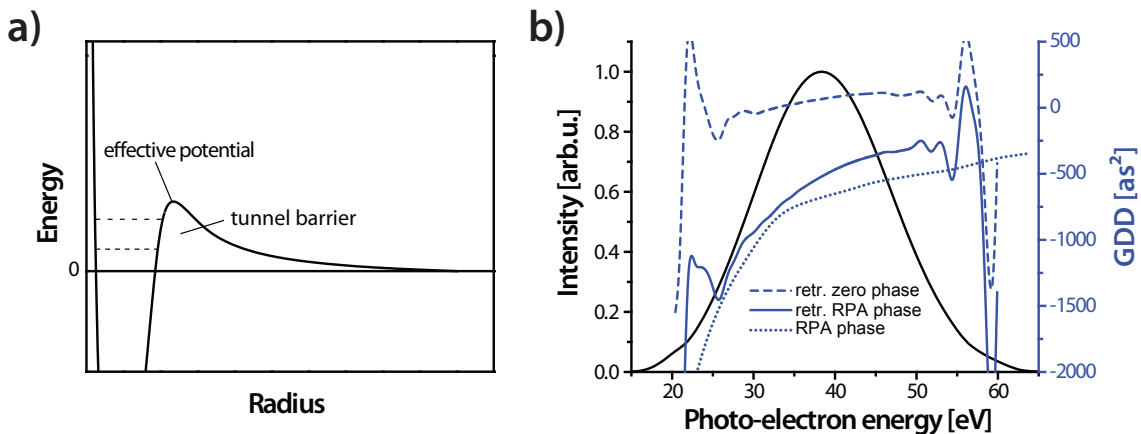


Figure 4.9: A schematic picture of a shape resonance with its effective potential is plotted in a). b) shows the results of the retrieval of simulated streakings, the spectrum in black the GDD in blue. The retrievals are in good agreement with the actual phase.

4.2. Giant Resonance of Xenon Probed by Broadband XUV-Pulses

almost similar, spectrograms of the same pulse. The difference between the spectrograms is a minor change of the lens voltage. In order to vary the retrieval, different temporal windows of each spectrogram were chosen: the full spectrogram, the first and the second half. For these photoelectron spectra of the neon measurements the error is small. The reconstructions of each part of the same spectrogram agree even better. In blue and labeled at the right is the GDD of the retrieved spectra. The GDD is almost constant at $4000 \text{ as}^2 \pm 1300 \text{ as}^2$. There is again a small tendency to lower GDD values for low energies and high values for high energies, but a constant phase for most of the central part of the spectrum is within the error bars of the reconstruction. This residual positive chirp could be compensated by using a thicker molybdenum filter. For this experiment however this pulse duration is completely sufficient and the XUV loss in the filter would hurt the statistics of the measurement.

In neon the recorded traces are very clean so there is no need for background correction. In Fig. 4.10 b) is the equivalent plot for xenon using the same XUV pulse under exactly the same conditions. The only difference is the probed gas and the lens voltage to collect the much lower photoelectron energies which are 45 eV lower than in neon due to the higher ionization energy $E_{ion} = 67 \text{ eV}$ of the 4d-sub shell of xenon. The changes caused by different lens voltages are taken into account by using the according lens correction data. The recorded and retrieved photoelectron spectrum is with $10 \text{ eV} \pm 2 \text{ eV}$ FWHM much narrower in bandwidth but the statistical error is comparable to the neon measurement. The GDD is also very different. It is almost constant for the electron energies between 30 and 40 eV at around -2000 as^2 and increases dramatically for lower electron energies. The statistical error of the phase is substantially higher for the lower energies. The higher background and the central momentum approximation have a higher influence on the low energy side.

In order to compare the two photoelectron spectra the retrieved neon spectrum was shifted by the ionization energy to represent the XUV-photon spectrum, multiplied by the partial cross section, taken from Kutzner et al. [102], and shifted by the ionization energy of xenon 4d resulting in the dashed red line in Fig. 4.10 b). The FWHM of the red line is with 22 eV much broader than the retrieved one. The discrepancy is most likely caused by the lens, respectively, wrong correction factors. Unfortunately there is no recent data for these corrections functions and the ones available seem to be off at least for the low voltages. On a different occasion the same measurement was conducted without lens. Two calibrated spectra of xenon are

shown in Fig. 4.11. For this evaluation the ATI background is subtracted in a very simple manner which causes the spectrum to start at 11 eV. The small amount of streaked photoelectrons at lower energies is hidden among a much bigger background of other low energetic electrons. The measured spectrum is slightly modulated by the odd harmonics clearly visible on the black line above 35 eV. The spectra are taken at different delays. The black line is a spectrum taken 6 fs before zero delay and the red line 6 fs after. Without the lens the measured photoelectron spectrum is clearly broader. It is also a bit lower in energy compared to the measurement shown before due to that day's laser performance.

With the observed double pulse structure it is not possible to retrieve any useful information about the chirp from this measurement, but it is a good demonstration what challenges have to be overcome in order to do so.

Without the lens a substantial background of lower energy electrons is visible. As they appear in a similar way for the reference measurement with neon just below the photon energies of the direct photoelectrons these are inelastically scattered electrons. As this background partially overlaps with the signal subtracting their contribution is crucial in order to not change the retrieved chirp by correcting for a false background. Slight errors in this necessary step can affect the retrieved phase more strongly than the change we expect caused by the xenon 4d electron emission. In photo-emission spectroscopy Shirley background correction is a common tool [103, 104, 105] to correct for inelastically scattered electrons. For this correction the background intensity within a peak is assumed proportional to the integrated intensity at higher energy with the condition that the background matches the mea-

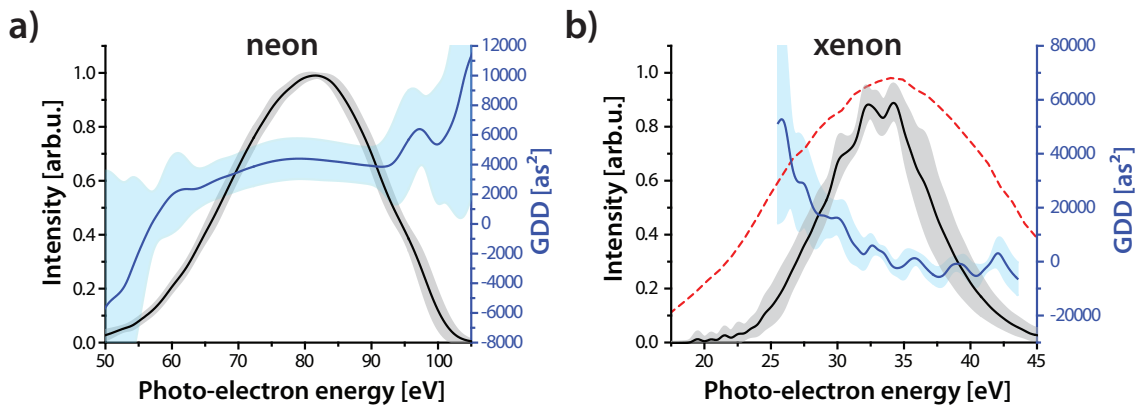


Figure 4.10: Retrieved spectra (black) and GDD (blue) for recorded spectrograms with neon and xenon. Statistical error bars in the according light color. The red dashed line in b) is the expected calculated photoelectron spectrum using neon as reference.

4.2. Giant Resonance of Xenon Probed by Broadband XUV-Pulses

sured spectrum outside the region of the peak. To utilize this correction the inelastic background has to be identified which is typically given by a plateau of lower energy electrons just below a direct photoelectron peak. With a mean free path in the order of magnitude of μm and electron energy of tens of eV the scattering time is in the order of ps for the gas target used which is much longer than the pulse duration of the IR laser. Thus the photoelectrons are streaked before they scatter making it necessary to calculate the Shirley background for each delay step separately. In the xenon measurement it is very difficult to identify the background as it merges with low energy electrons of different sources, mostly ATI electrons. It should be possible to extract the inelastically scatter electron background, at least for the unstreaked spectrum, by recording a spectrum without the IR laser. The second big complication is due to the Auger lines of xenon which are exactly in the spectral region of interest. The Auger lines are clearly visible in the red line spectrum in Fig. 4.11 but much less so in the black line before the zero delay. Before of course, means that the XUV-pulse comes first. As the Auger-electrons are not emitted instantaneously but corresponding to their life time the electrons feel the laser field at earlier delays than the photoelectrons. As their lifetime is much longer than half the laser period side bands are formed, depleting the main line and forming up- and down-shifted lines by multiples of the central energy of the streaking field. The life time of the highest

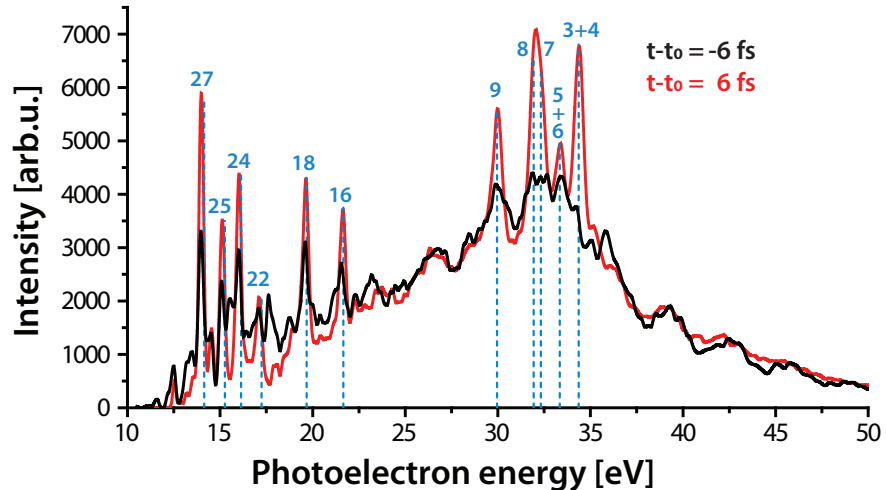


Figure 4.11: Two photoelectron spectra of xenon before (black) and after (red) the zero delay with the ToF-lens off. The bandwidth is broader than in Fig. 4.10. The delay dependent change of the Auger lines of xenon during the delay scan is apparent. The theoretical position of the Auger lines is indicated for the visible Auger lines and are numbered according to Werme et al. [106].

energies between 30 and 35 eV is such that the "zero delay" for the Auger electrons is a few femtoseconds earlier than for the photoelectrons. During the 12 fs difference of the two spectra the Auger-lines reappear, which makes the treatment of the lines very difficult. As they are not constant a simple subtraction is not possible. In order to extract the real pulse, wave packet information and the Auger lines have to be deconvoluted. Best chance in succeeding is by simulating the Auger lines and their streaking and fitting and subtracting it from the measured data. The setup was not able to supply such reliable data to perform these corrections with the necessary precision.

Recently, a work of Schoun et al. was published [107] in which they measured the dipole matrix elements of argon using a different approach. They studied the high-harmonic generation in argon and thus the dipole matrix element of the recombination of the accelerated electron with the argon atom. The imprint of the process is measured via resolution of attosecond beating by interference of two-photon transition (RABBITT). The bandwidth studied (20-70 eV) contains a Cooper minimum which provides a π -phase shift and a group delay change of more than 100 as which is about one order of magnitude higher than the effect of xenon 4d at 80 eV photon energy.

Studying a similar system with an isolated attosecond pulse in photo emission should have a much clearer imprint of the dipole matrix element. Xenon 4d has a Cooper minimum at 180 eV which provides an even bigger influence on the temporal behavior on the photoelectrons than in argon. Even in the Cooper-minimum the partial cross section of xenon 4d is with almost 0.5 Mb only a factor of 4 less than for neon 2p at 130 eV. The asymmetry parameter β however changes drastically from almost 2 to -0.8, which in streaking direction, corresponds to a factor of 15 less in counts. Mounting the ToF in the magic angle of 54.7° reduces the signal by a factor of three, but eliminates the influence of the asymmetry. For similar photon flux about one order of magnitude less signal than for current neon streakings can be expected. The XUV mirror at 180 eV with comparable bandwidth of ≈ 10 eV reflects about half an order of magnitude less than at 130 eV. Unfortunately the HH flux generation at 180 eV has been inefficient so far and the boron edge at 188 eV is still elusive in the recorded spectra (compare section 4.1.1). Using adsorbed xenon layers on a cooled solid target instead of a gas target will increase the signal by a fair bit and if the photon flux at 180 eV generated with a Ti:Sa-laser is still not sufficient the rapidly growing amount of ultrashort NIR OPCPAs at longer wavelength will provide the

4.2. Giant Resonance of Xenon Probed by Broadband XUV-Pulses

high energy photons.

So in summary, the conducted experiments on xenon 4d didn't allow a conclusive comparison between experiment and theory as the experimental approach has still too many uncertainties and has to overcome some challenges in data evaluation, e.g. correct treatment of Auger-lines and the background. However, it was shown that in principle the influence of the dipole matrix element on the electron wave packet is resolvable with attosecond streaking in close to perfect conditions. As the effect becomes bigger for lower energies a higher XUV photon flux will help especially to reduce the signature of low energy electron caused by the IR-laser which will also help in treating the inelastic background in the measurement correctly. So further improvements regarding the driving laser and the HHG will be a crucial step to tackle all the challenges of this experiment and will then be able to provide an experimental test of the theories in the near future.

4.3 Nonlinear Propagation in SiO₂

So far HHG with the new laser system and streakings of the driving pulse have been shown. The AS-2 beamline however is designed to be capable of much more. As the IR-laser and the XUV pulse are propagating through different arms (each about 1.6 m long) of the interferometer in the delay chamber it is easier to exchange filters and XUV mirrors in the XUV arm and the IR laser can be reused in its arm. Generating low order harmonics like second or third harmonic are one option, another is the introduction of a nonlinear effect which can, after recombining the beams, be probed by the XUV pulse. Following the transient absorption measurement slightly above 100 eV with intense IR-laser pulses in fused silica [16] and laser induced currents in dielectric materials with ultra-short pulses at intensities close to the damage threshold [108, 109, 110, 111] the investigation of the optical properties of fused silica and other dielectrics in the UV to near-IR with ultra-short pulses has been started. At AS-2 it is possible to refocus the IR-laser in its interferometer arm. By placing the sample close to the focus the intensity is high enough to damage most materials. Using very thin samples $<20\ \mu\text{m}$ and varying the intensity by moving the sample closer to or further from the focus. The intensity dependent effects on the pulse itself were studied by comparing the waveform extracted via streaking for different intensities. The data acquired with the very thin fused silica samples is presented in the PhD thesis by E.M. Bothschafter [112].

The very thin samples were used in order to not affect the pulse in a too strong manner which makes it very difficult to compare the pulses to each other and to theoretical simulations. Third order effects like self-focusing and self-steepening in the material increase the intensity in a hard to control manner which amplifies the effects themselves till higher order effects counter them e.g. generation of free electrons. Also in order to compare these measurements with full ab initio calculations of quartz, or more precisely a unit cell interacting with the intense laser field, which require a huge amount of computing power, thinner samples reduce it accordingly. These simulations are conducted by Prof. K. Yabana and his group and in collaboration with G. Wachter [111]. Using these thin fused silica targets is not without difficulties. The optical quality is poorer than is possible for more solid structures which affects the laser induced damage threshold and its statistical variance from sample to sample. So similar measurements were conducted with thicker samples.

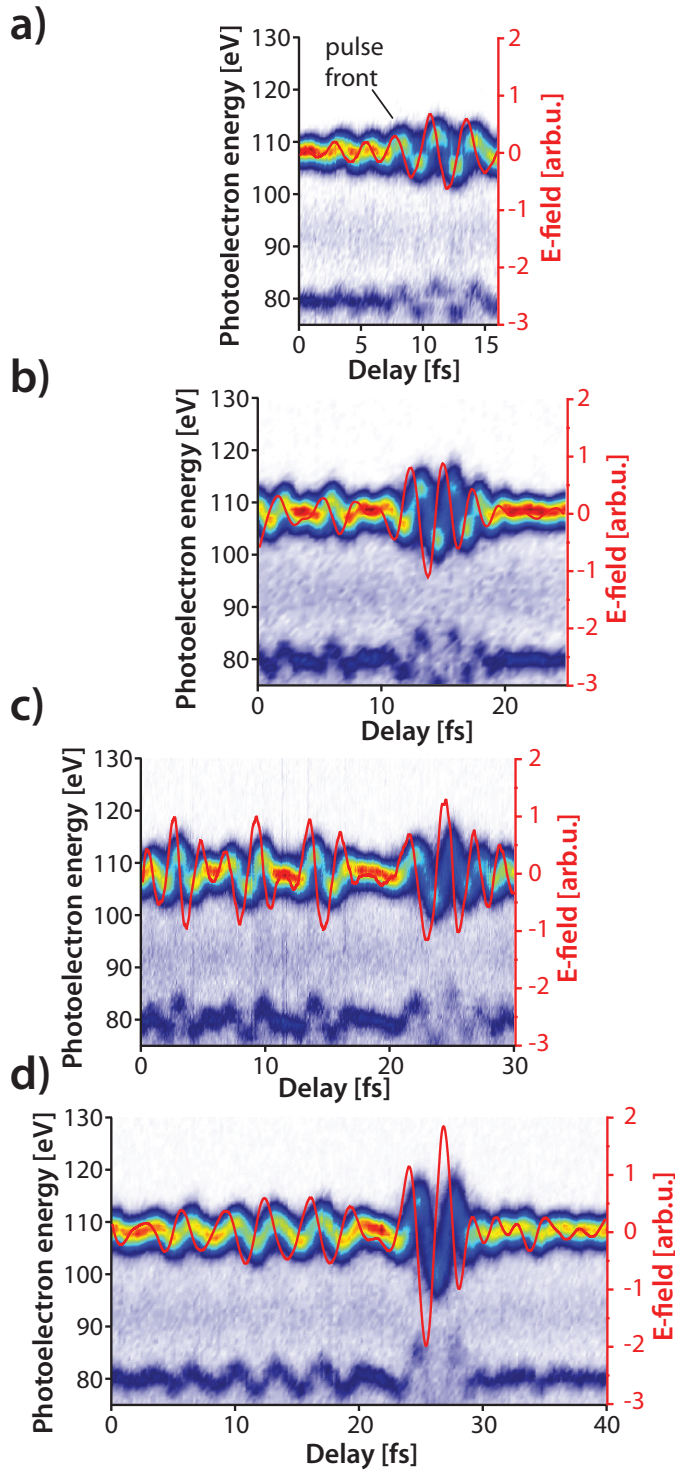


Figure 4.12: Recorded spectrograms without SiO₂ sample a) and with increasing intensity in a 100 μm fused silica sample b-d) and their reconstructed electric field.

A series of streakings and the extracted electric fields for a 100 μm thin fused silica sample mounted in Brewster's angle are shown in Fig. 4.12. In a) the pulse without the fused silica target is measured. This is equivalent to streaking the pulse which generated the HHs, or more precise the IR-pulse after generating the HHs. So this is a measurement similar to those in Fig. 4.8. The pulse duration here is just below 5 fs. Like before the low delays are before the IR pulse and high delays after. The pulse compression is not perfect there are some blue components visible in front of the pulse, the other side, although not recorded in this specific measurement is always quite clean. After inserting the target into the beam and adjusting the temporal overlap of the two arms b) was recorded. The intensity in the material is with $\approx 10^{12} \text{ W/cm}^2$ relatively low, but the waveform is already affected. The most obvious change is the increased amount of long wavelength components in front of the pulse beating there with the blue components already visible

in a) forming pre-pulses. The change is caused by SPM and to a minor degree by dispersion in the material. Increasing the intensity at the SiO₂ target leads to the streaking plotted in c). The changes from a) to b) become more enhanced and the pulse itself becomes shorter and visibly chirped by the newly generated components. By moving the target even closer to the focus reaching intensities above 10¹³ W/cm² the white light generation becomes even stronger than for c) but the streaking d) looks very different. The strong beating in front of the pulse is gone and instead of 3 distinct pulses it is one weak long pulse. The main pulse itself is considerably shorter and only slightly positively chirped. The FWHM of the envelope is 3.6 ± 0.1 fs. Note that the actual streaking amplitude is not always comparable as realigning the beam through the setup might slightly affect the position on iris apertures and their exact size is not always reproduced. The step from c) to d) has a different quality than from a) to b) to c) which show the same qualitative changes but due to the different intensities to different extent. In order to shorten the pulse from 5 fs to 3.6 fs the newly created spectral components have to be self-compressed to compensate the chirp caused by SPM clearly visible in b) and c). This compensation is intensity dependent and of higher order than SPM. An alternative option is that the measured pulse becomes shorter by an entirely different effect motivated by the following observation.

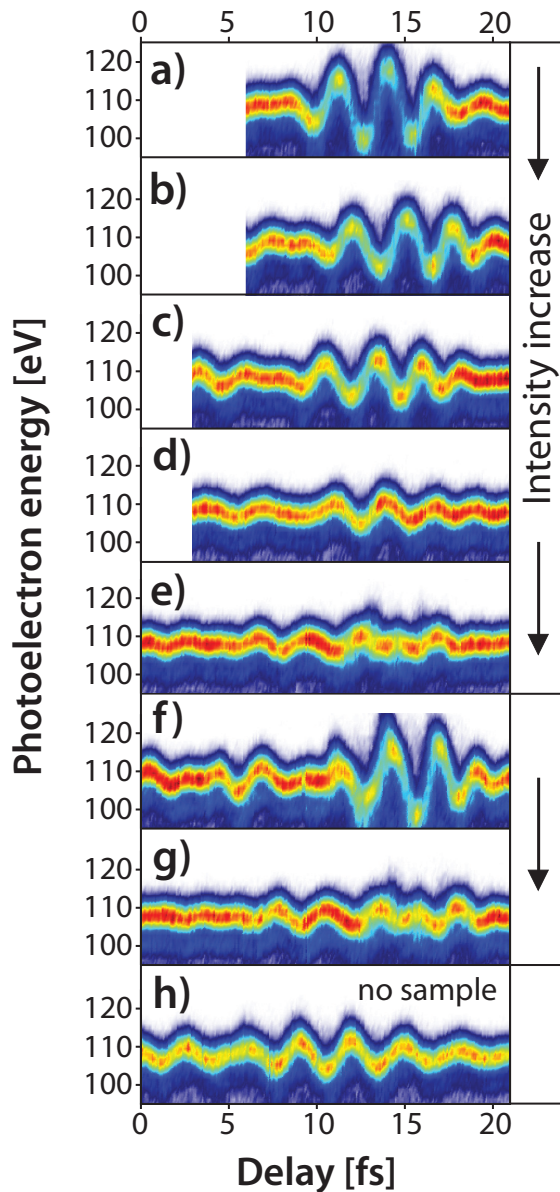


Figure 4.13: Recorded spectrograms without SiO₂ sample h) and with increasing intensity in a 100 μm fused silica sample a-e) and a rerun of a) and e) shown in f) and g).

The same measurement was repeated a few days later with very different results shown in Fig. 4.13. The intensity is gradually increased on target by moving it closer to the focus from a) to e). Here the iris aperture was unchanged during these measurements. Obviously the streaking amplitude is declining with more intensity and for d) and e) the pulse-form changed. This measurement was repeated with slightly higher streaking amplitude in f) and g) which reproduced the exact same behavior. For completeness the pulse without the SiO₂ target is plotted in h). As the laser power measured after the experimental chamber only changed by a few percent the main contribution of this dramatic decrease in amplitude is caused by an intensity induced change of the propagating pulse based on the Kerr-effect

$$n = n_0 + n_2 I = n_0 + \frac{3\chi^{(3)}}{8n_0} |E|^2 \quad .$$

The refractive index n can be written as an intensity independent part n_0 and an intensity dependent part n_2 . The latter is derived from the polarization of the material thus $\chi^{(3)}$ the susceptibility and depends on the applied electric field in this case given by the amplitude of the electric field of the pulse E . The high intensity increases (typically) the refractive index n of the material acting back on the laser pulse as a focusing optic. This change of the intensity distribution can be used to measure the nonlinear refractive index n_2 of the material ("z-scan") [113].

The streaking measurements are all conducted with the ToF detector at the same position. By changing the intensity on target the strength of the lens caused by the Kerr-effect changes and affects the beam propagation focusing the beam at different positions the size of the beam waist and the electric field strength follow accordingly. In Fig. 4.13 the focus moves further away from the streaked position thus the streaking amplitude becomes smaller. Of course this doesn't happen uniformly but intensity dependent, which for an ultrashort pulse is also strongly time dependent. Which means that the focus of the most intense part of the pulse is shifted the most. It is very likely that in Fig. 4.12 d) the self-focusing shifted the more intense part in the streaked z-position creating a shorter pulse at that position. Arguably with such distorted wavefront the measured pulse form doesn't describe the laser pulse well anymore as the measured pulse shape is very dependent on the spatial position. The exact effect on the pulse is highly nonlinear as small changes in pulse duration or beam shape lead to different results. So although the general effect could be reproduced an exact recreation was not possible in the allocated time. On a later

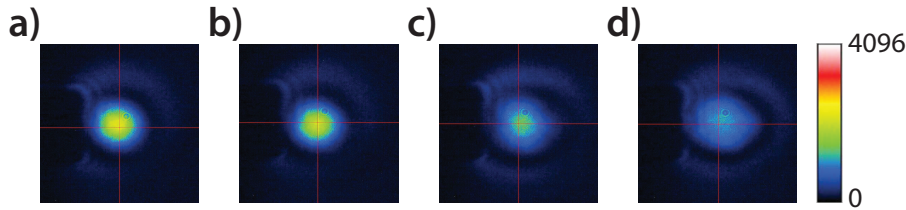


Figure 4.14: Imaged IR beamprofile at the position of the streaking nozzle (left) for increasing intensities a-d) in a thin fused silica sample close to the intermediate focus.

occasion we recorded the imaged intensity distribution at the streaking position for different intensities. With the thinner $20\ \mu\text{m}$ target used the effect is much small but still visible see Fig. 4.14. Of course the camera only detects the averaged intensity and not the temporal distribution of the pulse. Comparing the change between a) and d) from this figure to Fig. 4.13 the effect on the streaking measurement should be comparable to the change between a) and b).

For the transient nonlinear polarization measurement the lensing and propagation effect should be kept as small as possible and be better controlled. Moving the sample is not ideal as the effect on the pulse doesn't only depend on intensity, but also on the actual position. The beam profile should be as good as possible inside the SiO_2 sample to avoid higher order distortions caused by the Kerr-lens. As a hole is cut into the center of the beam by the perforated mirror separating the IR and the XUV the best profile is only available in the focal plane. Due to self focusing and propagation in the sample the effect is super-linear in sample-length (neglecting dispersion) so a thinner sample is to be preferred if applicable.

Considering the effect on the pulse duration observed in Fig. 4.12 the prospect of shortening the pulse duration from sub-5 fs to sub-4 fs by just adding a thin piece of fused silica at the right position before a focus is very alluring, as the effort necessary to achieve the same result by pushing the broadening and chirped mirror compression is challenging. By generating this short pulse right before using it can also circumvent propagation losses for these spectral components. But first it has to be determined how much energy is contained in this shorter pulse and if it is usable for nonlinear processes. The higher pulse energy of this laser system is an ideal test candidate as the trade off between effective pulse energy and pulse duration is an easy choice if you have surplus energy.

Chapter 5

Future Development

The main part of this thesis is the development and improvement of the laser source used for attosecond experiments e.g. to study multi electron dynamics as in xenon. This development of course never stops, but the time and space for implementation and testing is harder to come by when experiments can be conducted with the working laser. However, some issues just become apparent by using the laser for experiments and other problems might not be as crucial as expected for the experiments. The feasibility of innovative and challenging experiments stands and falls with the further improvement of the laser system.

5.1 Intense sub-3 fs Pulses

Although it is always advantageous to have more pulse-energy, as it is easier to dump some energy than to amplify more, with more than 1 mJ compressed pulse energy the space confinement, especially inside the vacuum chambers, starts to become problematic as damages of the optics occur more frequent. Also from the experimental side there is a bigger demand for yet shorter pulses than for a bit higher pulse energy.

Using the laser system as described in section 3.4 brought some of the limits of the current system to our attention which should be dealt with going forward. Up to the compression of the output of the second amplification stage the system seems to be in very good shape but the white light generation, though very efficient, lacks a bit of quality. With the high pulse energy the coupling to the fiber with static neon pressure is problematic and at the moment the broadening is limited by self-focusing at the end of the hollow core fiber. To tackle both of these issues a double sided

differentially pumped system is being built which consists of two aligned fibers with the gas inlet at the center and pumped chambers at the other end of each fiber. First tests, pumping the back side of one fiber, showed promise in using higher pressures for more broadening while simultaneously improving the spatial mode of the output. An improved mode profile will reduce the laser induced damages on silver mirrors which are disrupting the availability of the laser for experiments frequently. It will also result in an improved focus which will be beneficial for HHG or any other usage of the laser. Recently the glass wedges to adjust the exact dispersion, and thus the compression, of the white light have been moved into the vacuum system close to the HHG. As the pulse is still uncompressed, the intensity is reduced on the mirrors before it traverses the wedges and the laser induced damages of these optics seem to occur less frequent. The new fiber setup is accompanied by new challenges to be solved. The most important being the optical alignment and the mechanical stability of the system. The challenge of the alignment is the coupling at the center between the fibers which has to be matched well in order to be efficient and to keep a nice mode. Also transverse stress on the fibers has to be avoided as it will bend them which affects power and mode negatively. The whole setup will require more space on the optical table, especially in length, but hopefully the possibility to use higher gas pressures will counter this to some extent.

As the laser source (upstairs) and the experimental area (downstairs) are separated by more than ten reflections (for AS2) either the supported spectral bandwidth is limited by silver, to above 400 nm, or the reflection losses will be substantially increased by e.g. using aluminum mirrors. So for now, the target spectrum after the white light generation is determined by the reflectivity of silver, which means 400 nm to 1100 nm. Ideally the spectral intensity is well distributed and preferably with more weight on the red side in order to generate higher XUV-photon-energies. The new setup should be able to provide this at a reasonable output energy and surpass 1 mJ.

Compressing a spectrum that broad with one set of chirped dielectric mirrors is very challenging and several attempts with the half-mJ laser system have not shown a compelling compression so far. Spectral separation, individual compression of the different spectral parts and subsequent recombination has been demonstrated with outstanding results [65] and similarly for OPA [114]. Currently, a two-arm system is in development by A. Sommer to achieve excellent compression in this spectral range. The higher pulse energy of this laser system requires bigger optics to avoid

damage, leading to longer path-lengths, thicker substrates etc. and thus more dispersion has to be compensated which adds to the challenge. The distance of the compressor to the experiment and the necessary mechanical stability or alternatively the placement of the whole compressor inside the vacuum system, close to the experiment, is another. Adding more blue components to the current spectrum will also test the silver mirrors as the blue components seem to enhance the damage probability.

Improving the white light generation and the compression with the steps just mentioned will enable the system to provide 3 fs or sub-3 fs pulses with more than 600 μJ on the HHG target and will open up the path for attosecond UV and IR or UV and XUV pump probe experiments by generating very short UV-pulses in the intermediate focus of the AS-2 beam line.

Using the nonlinear effect inside a thin dielectric sample as described in chapter 4.3 might provide the opportunity to broaden the pulse significantly right in front of another nonlinear interaction. A test with fused silica and HHG in a collinear attosecond beam-line should be the first step to study the feasibility of this approach. This could very well moderate the challenges of propagating ultrashort pulses to the experiment if the generation of critical spectral components can take place right in front of the experiment.

5.2 Attosecond Experiments

This laser source was developed to provide more pulse energy at the same pulse quality as the common broadened 0.4 mJ Ti:sapphire CPA system in order to reach higher XUV photon energies and flux. It has been shown that the achieved XUV photo-spectra allow to apply higher photon energies e.g. the intensity dependent study of XUV transmission of silicon [16] up to 130 eV. An increased kinetic energy of the signal electrons permits higher laser intensities on target which is especially beneficial for photo-electron streaking of solid samples with low ionization energies (work-function). The same applies for most molecules as their ionization energy is usually considerably lower than for e.g. neon. The intensity required for the same kinetic energy of ATI electrons is obviously lower for materials with low work functions. Separating the XUV signal from the ATI background caused by the laser field is necessary for experiments with high intensities on target e.g. studies of the Franz-Keldysh effect close to the damage threshold of the material.

XUV photon energy dependent parameters can be extended into the now available range of 140 eV at comparable flux as formerly only achievable up to 125 eV. Studies of the energy dependence of e.g. photo-emission delays of tungsten can expand the observed spectral range in order to study effects of high energy band structures of solids.

With the expected shorter laser pulses, as described in the previous section, even higher photon energies will become available. Delay and chirp measurements just below the 4d-Cooper minimum of xenon should be feasible and as the expected effect is quite large, the delay is in the order of 100 as and the chirp accordingly, the visibility of the influence of dipole matrix element should be very high. On the other hand, increasing the focal length of HHG will enhance the photon flux at lower energies (≈ 100 eV) even further decreasing the time requirement of single scans or improving the statistical certainty of recorded data. Many interesting experiments with lower cross sections might become conductible with such an improved photon flux.

While decreasing the pulse duration and increasing the intensity pushes the cut-off energy to higher energies other generation setups than ionization gating offer much broader isolated attosecond pulses. While usually every attosecond pulse of the attosecond train propagates in the same direction, the direction of the XUV pulse can be influenced by the wave front of the driving laser field. A linear spatial chirp e.g. allows the separation of the XUV pulses spatially instead of spectrally [95]. A different route to more broadband attosecond pulses is to switch off all but one generating half-cycle via polarization gating [93]. This scheme as been improved by using a second color to break the symmetry even more, typically by using the second harmonic, named double optical gating (DOG) [115]. Adding an infrared field instead will even allow 30+ fs pulses to generate isolated attosecond pulses [116]. DOG has produced isolated ultra-broadband XUV spectra [117] covering several hundred eV. The lower energy part (50–130 eV) as been successfully compressed by 300 nm zirconium foil resulting in 67 as pulses [80]. So far DOG has only been used by few-cycle and multi-cycle pulses but although the generated XUV photon flux is a bit lower the broadband continuum is of interest for certain experiments, e.g. transient absorption measurements. The measured spectra also show an increase of the achievable photon energies and flux in the cut-off region compared to ionization gating for the same laser intensity. As the presented new laser source is quite powerful this scheme might be interesting to use for the 4-5 fs long pulses available right now.

Chapter 6

Conclusion

In order to proliferate attosecond science even further the sources for attosecond pulses have to be constantly improved and extended. In this work a standard Ti:Sa laser used for isolated attosecond pulse generation has been enhanced in pulse energy by a factor of 3.

A second cryogenic amplification stage provides up to 4 mJ pulses at 4 kHz repetition rate compressible down to 22 fs. Two efficient stretcher-compressor schemes, glass block compressor and transmission grating compressor, have been tested and the gratings have proven to be the superior design for this system. By using spectral phase feedback and a Dazzler the pulse is compressible close to the Fourier limit and by subsequent broadening in a static neon-filled 400 μm 1.5 m long hollow core fiber 1.5 mJ covering a spectral range of 500–1000 nm were achieved. After the compression by dielectric chirped mirrors 1.2 mJ with typically 4–5 fs pulse duration are available for experiments.

HHG with these pulses stands out due to higher XUV photon energies and photon flux. The generated photon flux in a neon gas-target was measured spectrally resolved and 5.5 pJ were obtained as pulse energy in the spectral range between 110–130 eV. Helium as target gas allows higher XUV photon energies, but for now the usable gas pressure is too low for efficient generation thus the XUV counts are too low for most experiments. In neon XUV photon energies up to 160 eV are available with reasonable flux up to 145 eV.

Broadband XUV pulses with 70–120 eV were used to study the photo-emission of the xenon 4d electrons to investigate the delay or rather the phase change caused by the dipole matrix element of the so called giant resonance in xenon. The capabilities of the approach were benchmarked by streaking the neon-2p electrons which

also served as a reference for the xenon measurement. Under good experimental conditions a phase with phase uncertainty of 1300 as^2 for the retrieval algorithm was determined. For the more challenging data of xenon the error was too big to confirm or falsify theoretical predictions but several ways to improve the accuracy of the measurement could be made based on this first attempt which is promising for a more extensive study of xenon.

Attosecond streaking was used to characterize the HH-generating pulse and provided insight into the significance of ionization gating when working at the intensity limit for efficient HHG. Single attosecond pulses at 130 eV were observed from chirped pulses as long as 12 fs as were two spectrally separated pulses generated in different half-cycles of the driving laser field. The delay between the two pulses was with $1250 \text{ as} \pm 100 \text{ as}$ retrieved in good agreement with the nominal half-cycle time of 1.25 fs.

The capabilities of the interferometric beam line were used to study the nonlinear polarization of fused silica close to its damage threshold with ultrashort pulses. For $100 \mu\text{m}$ samples the observed nonlinear effects are very strong and the intensity dependent Kerr-lens affects the propagation of the pulse severely. Aside from changes in the focus position, which are expected from a lens, a temporal shortening of the electric field was observed. The significant self-compression from 5 to 3.6 fs is a significant reduction of pulse duration which makes this process very interesting for applications.

With the improved laser and XUV parameters the developed laser system will serve as strong foundation for upcoming attosecond experiments. It improves and extends the existing capabilities as demonstrated in these first experiments and with the already ongoing upgrade to sub-4 fs the system will be able to provide high energy photon flux up to $\approx 155 \text{ eV}$.

With these short pulses and using a second gas target for third harmonic generation [118, 119] 2 fs UV pulses with $3 \mu\text{J}$ pulse energy (before spectral separation; assuming 0.5% conversion efficiency) will become available soon as well. Using strong cross phase modulation at higher intensities even shorter UV pulses with slightly reduced pulse energy are possible and will provide a perfect tool for time-resolved experiments e.g. using them as probe in time resolved transient absorption measurements of dielectrics. Combined with a probe in the NIR or XUV such short UV pulses can also serve as an ultrashort pump pulse to study fast electron dynamics in semi-conductors and molecules with unprecedented temporal resolution.

Bibliography

- [1] M. Hentschel, R. Kienberger, Ch. Spielmann, G. A. Reider, N. Milosevic, T. Brabec, P. Corkum, U. Heinzmann, M. Drescher, and F. Krausz. Attosecond metrology. *Nature*, 414(6863):509–513, November 2001.
- [2] M. Drescher, M. Hentschel, R. Kienberger, M. Uiberacker, V. Yakovlev, A. Scinzi, T. Westerwalbesloh, U. Kleineberg, U. Heinzmann, and F. Krausz. Time-resolved atomic inner-shell spectroscopy. *Nature*, 419:803–807, 2002.
- [3] P. Eckle, M. Smolarski, P. Schlup, J. Biegert, A. Staudte, M. Schoffler, H.G. Muller, R. Dorner, and U. Keller. Attosecond angular streaking. *Nat Phys*, 4:565–570, June 2008.
- [4] E. Goulielmakis, Z.-H. Loh, A. Wirth, R. Santra, N. Rohringer, V. Yakovlev, S. Zherebtsov, T. Pfeifer, A. M. Azzeer, M. F. Kling, S. Leone, and F. Krausz. Real-time observation of valence electron motion. *Nature*, 466:739–743, 2010.
- [5] M. Schultze, M. Fieß, N. Karpowicz, J. Gagnon, M. Korbman, M. Hofstetter, S. Neppl, A. L. Cavalieri, Y. Komninos, Th. Mercouris, C. A. Nicolaides, R. Pazourek, S. Nagele, J. Feist, J. Burgdörfer, A. M. Azzeer, R. Ernstorfer, R. Kienberger, U. Kleineberg, E. Goulielmakis, F. Krausz, and V. S. Yakovlev. Delay in photoemission. *Science*, 328(5986):1658–1662, 2010.
- [6] F. Kelkensberg, A. Rouzée, W. Siu, G. Gademann, P. Johnsson, M. Lucchini, R. R. Lucchese, and M. J. J. Vrakking. Xuv ionization of aligned molecules. *Phys. Rev. A*, 84:051404, Nov 2011.
- [7] A. L. Cavalieri, N. Müller, Th. Uphues, V. S. Yakovlev, A. Baltuška, B. Horvath, B. Schmidt, L. Blümel, R. Holzwarth, S. Hendel, M. Drescher, U. Kleineberg, P. M. Echenique, R. Kienberger, F. Krausz, and U. Heinzmann. Attosecond spectroscopy in condensed matter. *Nature*, 449(7165):1029–1032, 2007.
- [8] V. S. Yakovlev, J. Gagnon, N. Karpowicz, and F. Krausz. Attosecond streaking enables the measurement of quantum phase. *Phys. Rev. Lett.*, 105:073001, Aug 2010.
- [9] T. H. Maiman. Stimulated optical radiation in ruby. *Nature*, 187:493–494, 1960.

Bibliography

- [10] L. E. Hargrove, R. L. Fork, and M. A. Pollack. Locking of he–ne laser modes induced by synchronous intracavity modulation. *Applied Physics Letters*, 5(1):4–5, 1964.
- [11] Robert W. Boyd. *Nonlinear Optics*. Academic Press, third edition edition, 2008.
- [12] Th. Brabec and F. Krausz. Nonlinear optical pulse propagation in the single-cycle regime. *Phys. Rev. Lett.*, 78:3282–3285, Apr 1997.
- [13] G. D. Tsakiris, K. Eidmann, J. Meyer-ter Vehn, and F. Krausz. Route to intense single attosecond pulses. *New Journal of Physics*, 8:19, Jan 2006.
- [14] C. Lyngå, A. L’Huillier, and C.-G. Wahlström. High-order harmonic generation in molecular gases. *Journal of Physics B: Atomic, Molecular and Optical Physics*, 29(14):3293, 1996.
- [15] W. Li, X. Zhou, R. Lock, S. Patchkovskii, A. Stolow, H.C. Kapteyn, and M.M. Murnane. Time-resolved dynamics in n2o4 probed using high harmonic generation. *Science*, 322(5905):1207–1211, 2008.
- [16] M. Schultze, E.M. Bothschafter, A. Sommer, S. Holzner, W. Schweinberger, M. Fieß, M. Hofstetter, R. Kienberger, V. Apalkov, V. S. Yakovlev, M.I. Stockman, and F. Krausz. Controlling dielectrics with the electric field of light. *Nature*, 493:75–78, 2013.
- [17] P. B. Corkum. Plasma perspective on strong field multiphoton ionization. *Phys. Rev. Lett.*, 71:1994–1997, Sep 1993.
- [18] L. V. Keldysh. Ionization in the field of a strong electromagnetic wave. *Sov. Phys.*, 20:1307, May 1965.
- [19] M. V. Ammosov, N. B. Delone, and V. P. Krainov. Tunnel ionization of complex atoms and of atomic ions in an alternating electromagnetic field. *Sov. Phys.*, 64:1191, 1986.
- [20] G. L. Yudin and M. Yu. Ivanov. Nonadiabatic tunnel ionization: Looking inside a laser cycle. *Phys. Rev. A*, 64:013409, Jun 2001.
- [21] T. Popmintchev, M.-C. Chen, D. Popmintchev, P. Arpin, S. Brown, S. Ališauskas, G. Andriukaitis, T. Balčiunas, O. D. Mücke, A. Pugzlys, A. Baltuška, B. Shim, S. E. Schrauth, A. Gaeta, C. Hernández-García, L. Plaja, A. Becker, A. Jaron-Becker, M. M. Murnane, and H. C. Kapteyn. Bright coherent ultrahigh harmonics in the keV x-ray regime from mid-infrared femtosecond lasers. *Science*, 336:1287, Jun 2012.
- [22] J. Tate, T. Augustine, H. G. Muller, P. Salières, P. Agostini, and L. F. DiMauro. Scaling of wave-packet dynamics in an intense midinfrared field. *Phys. Rev. Lett.*, 98:013901, Jan 2007.

-
- [23] J. A. Pérez-Hernández, L. Roso, and L. Plaja. Harmonic generation beyond the strong-field approximation: the physics behind the short-wave-infrared scaling laws. *Opt. Express*, 17(12):9891–9903, Jun 2009.
- [24] P. Heissler, R. Hörlein, J. M. Mikhailova, L. Waldecker, P. Tzallas, A. Buck, K. Schmid, C. M. S. Sears, F. Krausz, L. Veisz, M. Zepf, and G. D. Tsakiris. Few-cycle driven relativistically oscillating plasma mirrors: A source of intense isolated attosecond pulses. *Phys. Rev. Lett.*, 108:235003, Jun 2012.
- [25] J. M. Mikhailova, M. V. Fedorov, N. Karpowicz, P. Gibbon, V. T. Platonenko, A. M. Zheltikov, and F. Krausz. Isolated attosecond pulses from laser-driven synchrotron radiation. *Phys. Rev. Lett.*, 109:245005, Dec 2012.
- [26] P. Heissler, R. Hörlein, M. Stafe, J.M. Mikhailova, Y. Nomura, D. Herrmann, R. Tautz, S.G. Rykovanov, I.B. Földes, K. Varjú, F. Tavella, A. Marcinkiewicz, F. Krausz, L. Veisz, and G.D. Tsakiris. Toward single attosecond pulses using harmonic emission from solid-density plasmas. *Applied Physics B*, 101(3):511–521, 2010.
- [27] A. Wirth. *Attosecond Transient Absorption Spectroscopy*. PhD thesis, Ludwig Maximilian Universität München, 2011.
- [28] M. Schultze. *Attosecond real time observation of ionization and electron-electron interactions*. PhD thesis, Ludwig Maximilian Universität München, 2008.
- [29] A. L. Schawlow and C. H. Townes. Infrared and optical masers. *Phys. Rev.*, 112:1940–1949, Dec 1958.
- [30] A.J. DeMaria, Jr. Glenn, W.H., M.J. Brienza, and M.E. Mack. Picosecond laser pulses. *Proceedings of the IEEE*, 57(1):2–25, Jan 1969.
- [31] D. Strickland and G. Mourou. Compression of amplified chirped optical pulses. *Optics Communications*, 56(3):219 – 221, 1985.
- [32] Ferenc Krausz, M.E. Fermann, T. Brabec, P.F. Curley, M. Hofer, M.H. Ober, Christian Spielmann, E. Wintner, and A.J. Schmidt. Femtosecond solid-state lasers. *Quantum Electronics, IEEE Journal of*, 28(10):2097–2122, Oct 1992.
- [33] S. Rausch, T. Binhammer, A. Harth, E. Schulz, M. Siegel, and U. Morgner. Few-cycle oscillator pulse train with constant carrier-envelope-phase and 65 as jitter. *Opt. Express*, 17(22):20282–20290, Oct 2009.
- [34] G. Sansone, E. Benedetti, F. Calegari, C. Vozzi, L. Avaldi, R. Flammini, L. Poletto, P. Villoresi, C. Altucci, R. Velotta, S. Stagira, S. De Silvestri, and M. Nisoli. Isolated single-cycle attosecond pulses. *Science*, 314(5798):443–446, 2006.

Bibliography

- [35] A. L. Cavalieri, E. Goulielmakis, B. Horvath, W. Helml, M. Schultze, M. Fieß, V. Pervak, L. Veisz, V. S. Yakovlev, M. Uiberacker, A. Apolonski, F. Krausz, and R. Kienberger. Intense 1.5-cycle near infrared laser waveforms and their use for the generation of ultra-broadband soft-x-ray harmonic continua. *New Journal of Physics*, 9(7):242, 2007.
- [36] E. Goulielmakis, M. Schultze, M. Hofstetter, V. S. Yakovlev, J. Gagnon, M. Uiberacker, A. L. Aquila, E. M. Gullikson, D. T. Attwood, R. Kienberger, F. Krausz, and U. Kleineberg. Single-cycle nonlinear optics. *Science*, 320(5883):1614–1617, 2008. isolated Attosecond 80 as pulse.
- [37] D. F. Hotz. Gain narrowing in a laser amplifier. *Appl. Opt.*, 4(5):527–530, May 1965.
- [38] P. Tournois. Acousto-optic programmable dispersive filter for adaptive compensation of group delay time dispersion in laser systems. *Optics Communications*, 140:245 – 249, 1997.
- [39] F. Verluise, V. Laude, Z. Cheng, Ch. Spielmann, and P. Tournois. Amplitude and phase control of ultrashort pulses by use of an acousto-optic programmable dispersive filter: pulse compression and shaping. *Opt. Lett.*, 25(8):575–577, Apr 2000.
- [40] T. Popmintchev, M.-C. Chen, O. Cohen, M. E. Grisham, J. J. Rocca, M. M. Murnane, and H. C. Kapteyn. Extended phase matching of high harmonics driven by mid-infrared light. *Opt. Lett.*, 33(18):2128–2130, Sep 2008.
- [41] G. Marcus, W. Helml, X. Gu, Y. Deng, R. Hartmann, T. Kobayashi, L. Strüder, R. Kienberger, and F. Krausz. Subfemtosecond k-shell excitation with a few-cycle infrared laser field. *Phys. Rev. Lett.*, 108:023201, Jan 2012.
- [42] N. Ishii, K. Kaneshima, K. Kitano, T. Kanai, Watanabe S., and Itatani J. Carrier-envelope phase-dependent high harmonic generation in the water window using few-cycle infrared pulses. *Nat Commun*, 5, 2014.
- [43] F. Tavella, Y. Nomura, L. Veisz, V. Pervak, A. Marcinkevičius, and F. Krausz. Dispersion management for a sub-10-fs, 10 TW optical parametric chirped-pulse amplifier. *Opt. Lett.*, 32(15):2227–2229, Aug 2007.
- [44] S. Kane and J. Squier. Grism-pair stretcher–compressor system for simultaneous second- and third-order dispersion compensation in chirped-pulse amplification. *J. Opt. Soc. Am. B*, 14(3):661–665, Mar 1997.
- [45] W. Schweinberger. Development of a high-energy pulse compression system based on a hollow core fiber. Master’s thesis, Ludwig Maximilian Universität München, 2008.

-
- [46] F. Reiter, U. Graf, E. E. Serebryannikov, W. Schweinberger, M. Fiess, M. Schultze, A. M. Azzeeer, R. Kienberger, F. Krausz, A. M. Zheltikov, and E. Goulielmakis. Route to attosecond nonlinear spectroscopy. *Phys. Rev. Lett.*, 105:243902, Dec 2010.
- [47] E. Granados, L.-J. Chen, C.-J. Lai, K.-H. Hong, and F. X. Kärtner. Wavelength scaling of optimal hollow-core fiber compressors in the single-cycle limit. *Opt. Express*, 20(8):9099–9108, Apr 2012.
- [48] A.J. Verhoef, J. Seres, K. Schmid, Y. Nomura, G. Tempea, L. Veisz, and F. Krausz. Compression of the pulses of a ti:sapphire laser system to 5 femtoseconds at 0.2 terawatt level. *Applied Physics B*, 82(4):513–517, 2006.
- [49] A. Suda, M. Hatayama, K. Nagasaka, and K. Midorikawa. Generation of sub-10-fs, 5-mJ-optical pulses using a hollow fiber with a pressure gradient. *Applied Physics Letters*, 86(11), 2005.
- [50] G. Stibenz, N. Zhavoronkov, and G. Steinmeyer. Self-compression of millijoule pulses to 7.8 fs duration in a white-light filament. In *Conference on Lasers and Electro-Optics/Quantum Electronics and Laser Science Conference and Photonic Applications Systems Technologies*, page CThA6. Optical Society of America, 2006.
- [51] X. Chen, X. Li, J. Liu, P. Wei, X. Ge, R. Li, and Z. Xu. Generation of 5 fs, 0.7 mJ pulses at 1 khz through cascade filamentation. *Opt. Lett.*, 32(16):2402–2404, Aug 2007.
- [52] L. Gallmann, T. Pfeifer, P.M. Nagel, M.J. Abel, D.M. Neumark, and S.R. Leone. Comparison of the filamentation and the hollow-core fiber characteristics for pulse compression into the few-cycle regime. *Applied Physics B*, 86(4):561–566, 2007.
- [53] X. Chen, A. Jullien, A. Malvache, L. Canova, A. Borot, A. Trisorio, C. G. Durfee, and R. Lopez-Martens. Generation of 4.3 fs, 1 mJ laser pulses via compression of circularly polarized pulses in a gas-filled hollow-core fiber. *Opt. Lett.*, 34(10):1588–1590, May 2009.
- [54] A. Malvache, X. Chen, C.G. Durfee, A. Jullien, and R. Lopez-Martens. Multi-mJ pulse compression in hollow fibers using circular polarization. *Applied Physics B*, 104(1):5–9, 2011.
- [55] M. Th. Hassan, A. Wirth, I. Grguraš, A. Moulet, T. T. Luu, J. Gagnon, V. Pavuk, and E. Goulielmakis. Invited article: Attosecond photonics: Synthesis and control of light transients. *Review of Scientific Instruments*, 83(11):–, 2012.

Bibliography

- [56] M. Nurhuda, A. Suda, M. Kaku, and K. Midorikawa. Optimization of hollow fiber pulse compression using pressure gradients. *Applied Physics B*, 89(2-3):209–215, 2007.
- [57] T. Nagy, M. Forster, and P. Simon. Flexible hollow fiber for pulse compressors. *Appl. Opt.*, 47(18):3264–3268, Jun 2008.
- [58] F. X. Kärtner, N. Matuschek, T. Schibli, U. Keller, H. A. Haus, C. Heine, R. Morf, V. Scheuer, M. Tilsch, and T. Tschudi. Design and fabrication of double-chirped mirrors. *Opt. Lett.*, 22(11):831–833, Jun 1997.
- [59] N. Matuschek, L. Gallmann, D.H. Sutter, G. Steinmeyer, and U. Keller. Back-side-coated chirped mirrors with ultra-smooth broadband dispersion characteristics. *Applied Physics B*, 71(4):509–522, 2000.
- [60] V. Pervak, A.V. Tikhonravov, M.K. Trubetskov, S. Naumov, F. Krausz, and A. Apolonski. 1.5-octave chirped mirror for pulse compression down to sub-3 Å fs. *Applied Physics B*, 87(1):5–12, 2007.
- [61] C. Iaconis and I.A. Walmsley. Spectral phase interferometry for direct electric-field reconstruction of ultrashort optical pulses. *Opt. Lett.*, 23(10):792–794, May 1998.
- [62] R. Trebino, K. W. DeLong, D. N. Fittinghoff, J. N. Sweetser, M. A. Krumbügel, B. A. Richman, and D. J. Kane. Measuring ultrashort laser pulses in the time-frequency domain using frequency-resolved optical gating. *Review of Scientific Instruments*, 68(9):3277–3295, 1997.
- [63] B. Schenkel, J. Biegert, U. Keller, C. Vozzi, M. Nisoli, G. Sansone, S. Stagira, S. De Silvestri, and O. Svelto. Generation of 3.8-fs pulses from adaptive compression of a cascaded hollow fiber supercontinuum. *Opt. Lett.*, 28(20):1987–1989, Oct 2003.
- [64] G. Steinmeyer and G. Stibenz. Generation of sub-4-fs pulses via compression of a white-light continuum using only chirped mirrors. *Applied Physics B*, 82(2):175–181, 2006.
- [65] M. T. Hassan, T. T. Luu, A. Moulet, O. Raskazovskaya, P. Zhokov, M. Garg, N. Karpowicz, A. M. Zheltikov, V. Pervak, Krausz F., and E. Goulielmakis. Attosecond optical control of bound electrons. *submitted to Nature*, -:-, 2014.
- [66] Robert W. Boyd. Intuitive explanation of the phase anomaly of focused light beams. *J. Opt. Soc. Am.*, 70(7):877–880, Jul 1980.
- [67] Th. Udem, R. Holzwarth, and T.W. Hänsch. Optical frequency metrology. *Nature*, 416:233–237, 2002.

-
- [68] T. Fuji, A. Apolonski, and F. Krausz. Self-stabilization of carrier-envelope offset phase by use of difference-frequency generation. *Opt. Lett.*, 29(6):632–634, Mar 2004.
- [69] F. Lücking, A. Assion, A. Apolonski, F. Krausz, and G. Steinmeyer. Long-term carrier-envelope-phase-stable few-cycle pulses by use of the feed-forward method. *Opt. Lett.*, 37(11):2076–2078, Jun 2012.
- [70] T. Wittmann, B. Horvath, W. Helml, M.G. Schatzel, X. Gu, A. L. Cavalieri, G.G. Paulus, and R. Kienberger. Single-shot carrier-envelope phase measurement of few-cycle laser pulses. *Nat Phys*, 5:357–362, 2009.
- [71] T. Clausnitzer, J. Limpert, K. Zöllner, H. Zellmer, H.-J. Fuchs, E.-B. Kley, A. Tünnermann, M. Jupé, and D. Ristau. Highly efficient transmission gratings in fused silica for chirped-pulse amplification systems. *Appl. Opt.*, 42(34):6934–6938, Dec 2003.
- [72] H. Mashiko, Ch. M. Nakamura, C. Li, E. Moon, H. Wang, J. Tackett, and Z. Chang. Carrier-envelope phase stabilized 5.6fs, 1.2mJ pulses. *Applied Physics Letters*, 90(16):–, 2007.
- [73] J.H. Sung, J.Y. Park, T. Imran, Y.S. Lee, and C.H. Nam. Generation of 0.2-TW 5.5-fs optical pulses at 1 kHz using a differentially pumped hollow-fiber chirped-mirror compressor. *Applied Physics B*, 82(1):5–8, 2006.
- [74] A. Jullien, A. Ricci, F. Böhle, J.-P. Rousseau, S. Grabielle, N. Forget, H. Jacqmin, B. Mercier, and R. Lopez-Martens. Carrier-envelope phase stable, high-contrast, double-cpa laser system. *Optics Letters*, 39:3774–3777, 2014.
- [75] J. Park, J. Lee, and C.H. Nam. Generation of 1.5 cycle 0.3 TW laser pulses using a hollow-fiber pulse compressor. *Opt. Lett.*, 34(15):2342–2344, Aug 2009.
- [76] Zh.-M. Song, G.-X. Zhang, S.-Y. Cao, D.-Q. Pang, L. Chai, Q.-Y. Wang, and Zh.-G. Zhang. Simulation of femtosecond pulse propagation through hollow fibre filled with noble gases of gradient temperature. *Chinese Physics Letters*, 25(1):129, 2008.
- [77] D. Brida, C. Manzoni, G. Cirimi, M. Marangoni, S. Bonora, P. Villoresi, S. De Silvestri, and G. Cerullo. Few-optical-cycle pulses tunable from the visible to the mid-infrared by optical parametric amplifiers. *Journal of Optics*, 12(1):013001, 2010.
- [78] D. Herrmann, C. Homann, R. Tautz, M. Scharrer, P.St.J. Russell, F. Krausz, L. Veisz, and E. Riedle. Approaching the full octave: noncollinear optical parametric chirped pulse amplification with two-color pumping. *Opt. Express*, 18(18):18752–18762, Aug 2010.

Bibliography

- [79] D. Herrmann, L. Veisz, R. Tautz, F. Tavella, K. Schmid, V. Pervak, and F. Krausz. Generation of sub-three-cycle, 16 tw light pulses by using noncollinear optical parametric chirped-pulse amplification. *Opt. Lett.*, 34(16):2459–2461, Aug 2009.
- [80] K. Zhao, Q. Zhang, M. Chini, Y. Wu, X. Wang, and Z. Chang. Tailoring a 67 attosecond pulse through advantageous phase-mismatch. *Opt. Lett.*, 37(18):3891–3893, Sep 2012.
- [81] Alexander Schwarz. *Few-cycle phase-stable infrared OPCPA*. PhD thesis, Ludwig Maximilian Universität München, 2014.
- [82] M. Fieß, M. Schultze, E. Goulielmakis, B. Dennhardt, J. Gagnon, M. Hofstetter, R. Kienberger, and F. Krausz. Versatile apparatus for attosecond metrology and spectroscopy. *Review of Scientific Instruments*, 81(9):–, 2010.
- [83] Markus Fieß. *Advancing attosecond metrology*. PhD thesis, Ludwig Maximilian Universität, Jun 2010.
- [84] P. Naulleau. The center for x-ray optics, 2014. Stand 02.06.2014.
- [85] Justin Gagnon. Attogram, 2008. Stand 21.05.2014.
- [86] M. Lewenstein, P. Salières, and A. L’Huillier. Phase of the atomic polarization in high-order harmonic generation. *Phys. Rev. A*, 52:4747–4754, Dec 1995.
- [87] W. Schweinberger, A. Sommer, E. Bothschafter, J. Li, F. Krausz, R. Kienberger, and M. Schultze. Waveform-controlled near-single-cycle milli-joule laser pulses generate sub-10 nm extreme ultraviolet continua. *Opt. Lett.*, 37(17):3573–3575, Sep 2012.
- [88] N. Ishii, S. Adachi, Y. Nomura, A. Kosuge, Y. Kobayashi, T. Kanai, J. Itatani, and S. Watanabe. Generation of soft x-ray and water window harmonics using a few-cycle, phase-locked, optical parametric chirped-pulse amplifier. *Opt. Lett.*, 37(1):97–99, Jan 2012.
- [89] M.-C. Chen, P. Arpin, T. Popmintchev, M. Gerrity, B. Zhang, M. Seaberg, D. Popmintchev, M. M. Murnane, and H. C. Kapteyn. Bright, coherent, ultrafast soft x-ray harmonics spanning the water window from a tabletop light source. *Phys. Rev. Lett.*, 105:173901, Oct 2010.
- [90] F. Ferrari, F. Calegari, M. Lucchini, Vozzi C., S. Stagira, G. Sansone, and M. Nisoli. High-energy isolated attosecond pulses generated by above-saturation few-cycle fields. *Nat Photon*, 4(12):875–879, 2010.
- [91] M. Krebs, S. Hadrich, S. Demmler, J. Rothhardt, A. Zair, L. Chipperfield, J. Limpert, and A. Tunnermann. Towards isolated attosecond pulses at megahertz repetition rates. *Nat Photon*, 7:555–559, 2013.

-
- [92] F. Scholze, H. Rabus, and G. Ulm. Mean energy required to produce an electron-hole pair in silicon for photons of energies between 50 and 1500 eV. *Journal of Applied Physics*, 84(5):2926–2939, 1998.
- [93] I.J. Sola, E. Mével, L. Elouga, E. Constant, V. Strelkov, L. Poletto, P. Villoresi, E. Benedetti, J.-P. Caumes, S. Stagira, C. Vozzi, G. Sansone, and M. Nisoli. Controlling attosecond electron dynamics by phase-stabilized polarization gating. *Nat Phys*, 2:319–322, May 2006.
- [94] M. J. Abel, T. Pfeifer, P. M. Nagel, W. Boutu, M. J. Bell, C. P. Steiner, D. M. Neumark, and S. R. Leone. Isolated attosecond pulses from ionization gating of high-harmonic emission. *Chemical Physics*, 366:9 – 14, 2009. Attosecond Molecular Dynamics.
- [95] K. T. Kim, Ch. Zhang, T. Ruchon, J.-F. Hergott, T. Auguste, D. M. Villeneuve, P. B. Corkum, and F. Quéré. Photonic streaking of attosecond pulse trains. *Nat Photon*, 7(8):651–656, 2013.
- [96] J. Gagnon and V. S. Yakovlev. The robustness of attosecond streaking measurements. *Opt. Express*, 17(20):17678–17693, Sep 2009.
- [97] D. Oron, Y. Silberberg, N. Dudovich, and D. M. Villeneuve. Efficient polarization gating of high-order harmonic generation by polarization-shaped ultrashort pulses. *Phys. Rev. A*, 72:063816, Dec 2005.
- [98] S. Neppl, R. Ernstorfer, E. M. Bothschafter, A. L. Cavalieri, D. Menzel, J. V. Barth, F. Krausz, R. Kienberger, and P. Feulner. Attosecond time-resolved photoemission from core and valence states of magnesium. *Phys. Rev. Lett.*, 109:087401, Aug 2012.
- [99] G. Snell, U. Hergenhahn, N. Müller, M. Drescher, J. Viefhaus, U. Becker, and U. Heinzmann. Study of xenon 4d, 5p, and 5s photoionization in the shape-resonance region using spin-resolved electron spectroscopy. *Phys. Rev. A*, 63:032712, Feb 2001.
- [100] U. Becker, D. Szostak, H. G. Kerkhoff, M. Kupsch, B. Langer, R. Wehlitz, A. Yagishita, and T. Hayaishi. Subshell photoionization of xe between 40 and 1000 ev. *Phys. Rev. A*, 39:3902–3911, Apr 1989.
- [101] A. S. Kheifets. Time delay in valence-shell photoionization of noble-gas atoms. *Phys. Rev. A*, 87:063404, Jun 2013.
- [102] M. Kutzner, V. Radojević and H. P. Kelly. Extended photoionization calculations for xenon. *Phys. Rev. A*, 40:5052–5057, Nov 1989.
- [103] D. A. Shirley. High-resolution x-ray photoemission spectrum of the valence bands of gold. *Phys. Rev. B*, 5:4709–4714, Jun 1972.

Bibliography

- [104] S. Tougaard and P. Sigmund. Influence of elastic and inelastic scattering on energy spectra of electrons emitted from solids. *Phys. Rev. B*, 25:4452–4466, Apr 1982.
- [105] S. Tougaard. Inelastic background correction and quantitative surface analysis. *Journal of Electron Spectroscopy and Related Phenomena*, 52(0):243 – 271, 1990.
- [106] L.O. Werme, T. Bergmark, and K. Siegbahn. The high resolution l 2,3 mm and m 4,5 nm auger spectra from krypton and m 4,5 nm and n 4,5 oo auger spectra from xenon. *Physica Scripta*, 6(2-3):141, 1972.
- [107] B. Schoun, S. R. Chirla, J. Wheeler, C. Roedig, P. Agostini, F. DiMauro, L. J. Schafer, K. and B. Gaarde, M. Attosecond pulse shaping around a cooper minimum. *Phys. Rev. Lett.*, 112:153001, Apr 2014.
- [108] A. Schiffrin, T. Paasch-Colberg, N. Karpowicz, V. Apalkov, D. Gerster, S. Mühlbrandt, M. Korbmann, J. Reichert, M. Schultze, S. Holzner, J.V. Barth, R. Kienberger, R. Ernstdorfer, V. S. Yakovlev, M. Stockman, and F. Krausz. Optical-field-induced current in dielectrics. *Nature*, 493:70–74, 2013.
- [109] T. Paasch-Colberg, A. Schiffrin, N. Karpowicz, S. Kruchinin, Ö. Sağlam, S. Keiber, O. Razskazovskaya, A. Mühlbrandt, S. and Alnaser, M. Kübel, V. Apalkov, D. Gerster, J. Reichert, T. Wittmann, J.V. Barth, M. Stockman, R. Ernstdorfer, V. S. Yakovlev, and F. Krausz. Solid-state light-phase detector. *Nat Photon*, 8:214–218, 2014.
- [110] Tim Paasch-Colberg. *Ultrafast, optical-field-induced currents in solid-state materials*. PhD thesis, Technische Universität München, 2014.
- [111] G. Wachter, Ch. Lemell, J. Burgdörfer, S. A. Sato, X.-M. Tong, and K. Yabana. Ab-initio simulation of optical-field induced currents in dielectrics. *arXiv preprint arXiv:1401.4357*, 2014.
- [112] E.M. Bothschafter. *Femtosecond and Attosecond Electron Dynamics in Semiconductors and Dielectrics*. PhD thesis, Technische Universität München, 2014.
- [113] M. Sheik-Bahae, A.A. Said, T.-H. Wei, D.J. Hagan, and E. W. Van Stryland. Sensitive measurement of optical nonlinearities using a single beam. *Quantum Electronics, IEEE Journal of*, 26(4):760–769, Apr 1990.
- [114] S.-W. Huang, G. Cirmi, J. Moses, K.-H. Hong, S. Bhardwaj, J. R. Birge, L.-J. Chen, E. Li, B. J. Eggleton, G. Cerullo, and F. X. Kärtner. High-energy pulse synthesis with sub-cycle waveform control for strong-field physics. *Nat Photon*, 5:475–479, 2011.

- [115] H. Mashiko, S. Gilbertson, C. Li, S. D. Khan, M. M. Shakya, E. Moon, and Z. Chang. Double optical gating of high-order harmonic generation with carrier-envelope phase stabilized lasers. *Phys. Rev. Lett.*, 100:103906, Mar 2008.
- [116] P. Lan, E. J. Takahashi, and K. Midorikawa. Isolated-attosecond-pulse generation with infrared double optical gating. *Phys. Rev. A*, 83:063839, Jun 2011.
- [117] H. Mashiko, S. Gilbertson, M. Chini, X. Feng, C. Yun, H. Wang, S. D. Khan, S. Chen, and Z. Chang. Extreme ultraviolet supercontinua supporting pulse durations of less than one atomic unit of time. *Opt. Lett.*, 34(21):3337–3339, Nov 2009.
- [118] U. Graf, M. Fieß, M. Schultze, Kienberger R., Krausz F., and E. Goulielmakis. Intense few-cycle light pulses in the deep ultraviolet. *Opt. Express*, 16(23):18956–18963, Nov 2008.
- [119] F. Reiter, U. Graf, M. Schultze, W. Schweinberger, H. Schröder, N. Karpowicz, A. M. Azzeer, R. Kienberger, F. Krausz, and E. Goulielmakis. Generation of sub-3 fs pulses in the deep ultraviolet. *Opt. Lett.*, 35(13):2248–2250, Jul 2010.

Two-Stage Laser Setup with Transmission Gratings

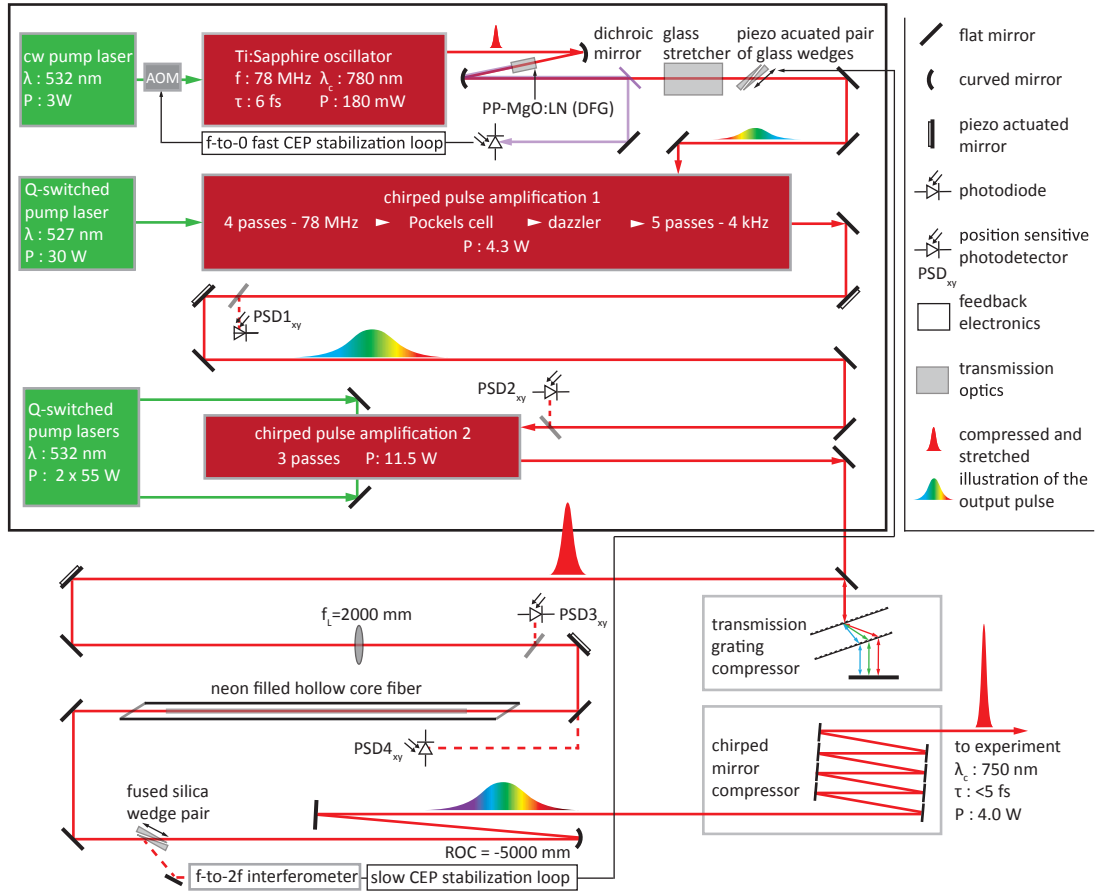


Figure A.2: Schematic beam-path of the two-stage laser setup: A glass stretcher is used after the oscillator and a Dazzler in the CPA1. After CPA2 the laser is compressed by an efficient transmission grating compressor. A static hollow core fiber is used for white light generation and chirped mirrors for sub-5 fs pulses with 1.0 mJ and more are available for experiments

AS-2 Beam-line Setup for Broadband Streaking

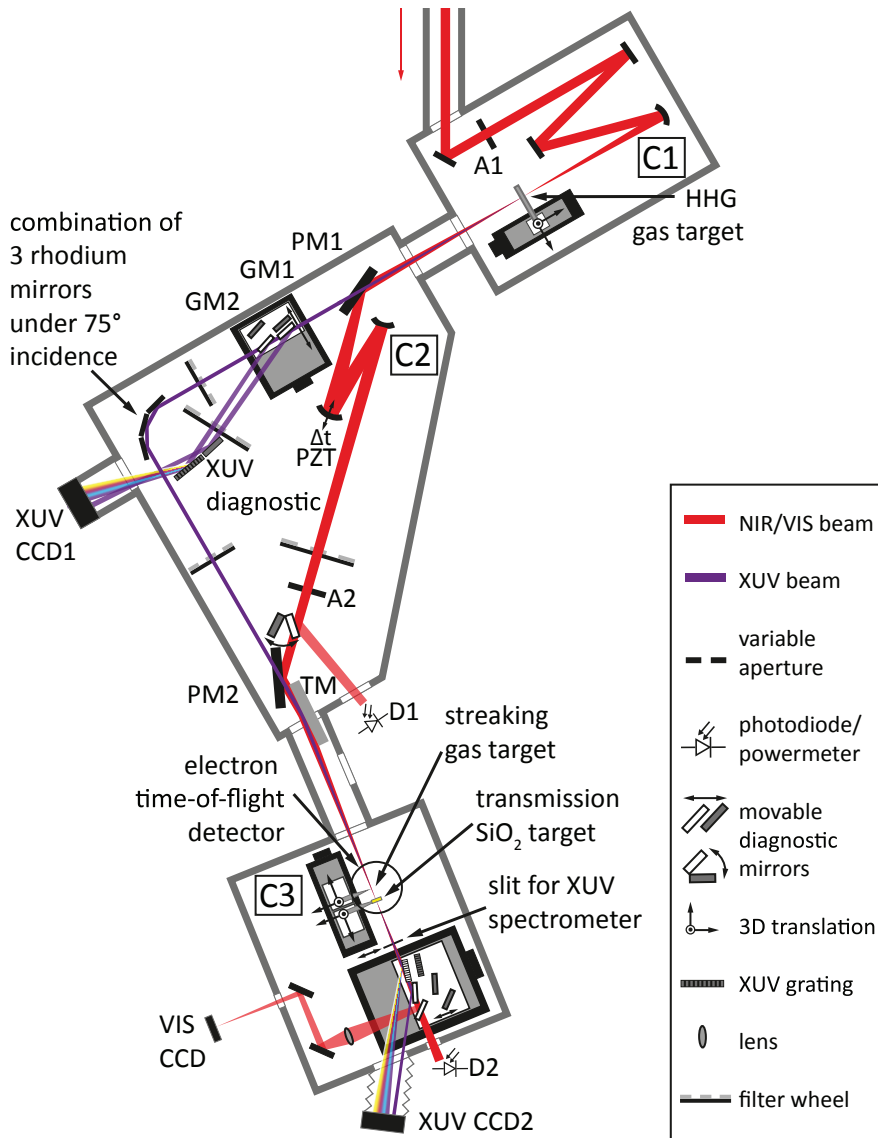


Figure A.3: AS2 beam-line setup for broadband attosecond spectroscopy. C1 is the HHG-chamber with movable gas target. C2 the delay chamber with the interferometer between the XUV and NIR laser beam. Separated and recombined by perforated mirrors (PM1, PM2). Diagnostics for the XUV can be used via gold mirrors (GM1, GM2) on a translation stage. The XUV beam is reflected by rhodium mirrors in the corner for broadband spectrum. Various filters can be changed in all beam-paths. After recombination both beams are focused by a toroidal mirror (TM) into the experimental chamber C3. The Tof and the gas target are placed at the focus which is imaged onto a camera outside the chamber and the XUV spectrum can be measured behind the gas target as can the NIR laser power and spectrum.

AS-2 Beamline Setup for SiO₂

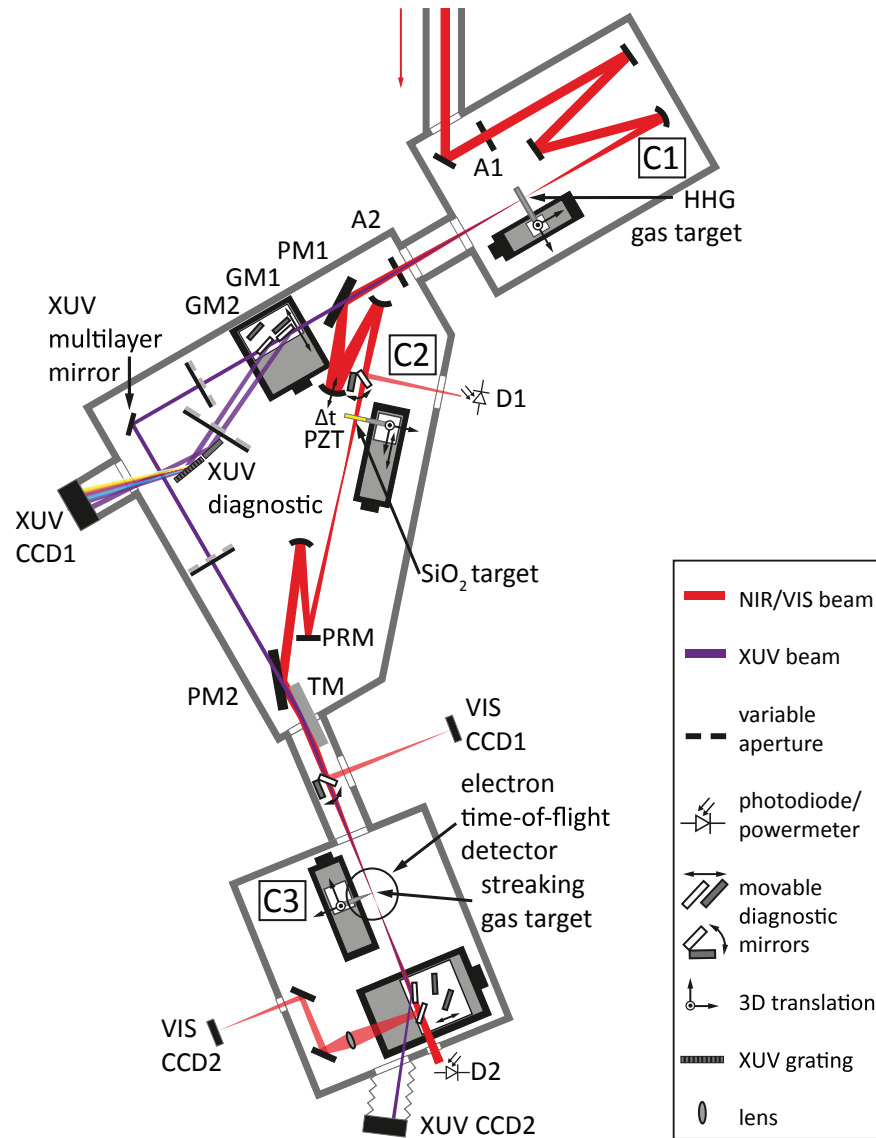


Figure A.4: AS2 beam-line for streaking the NIR waveform after transmission through thin dielectrics at close to damage threshold intensities. The SiO₂ target is movable in the C2 chamber along the convergent laser beam before the intermediate focus. The intensity dependent change is observed via streaking in C3. Fig. A.3 and Fig. A.4 are thankfully taken with permission from [112].

Original Setup of the Second Stage Amplifier

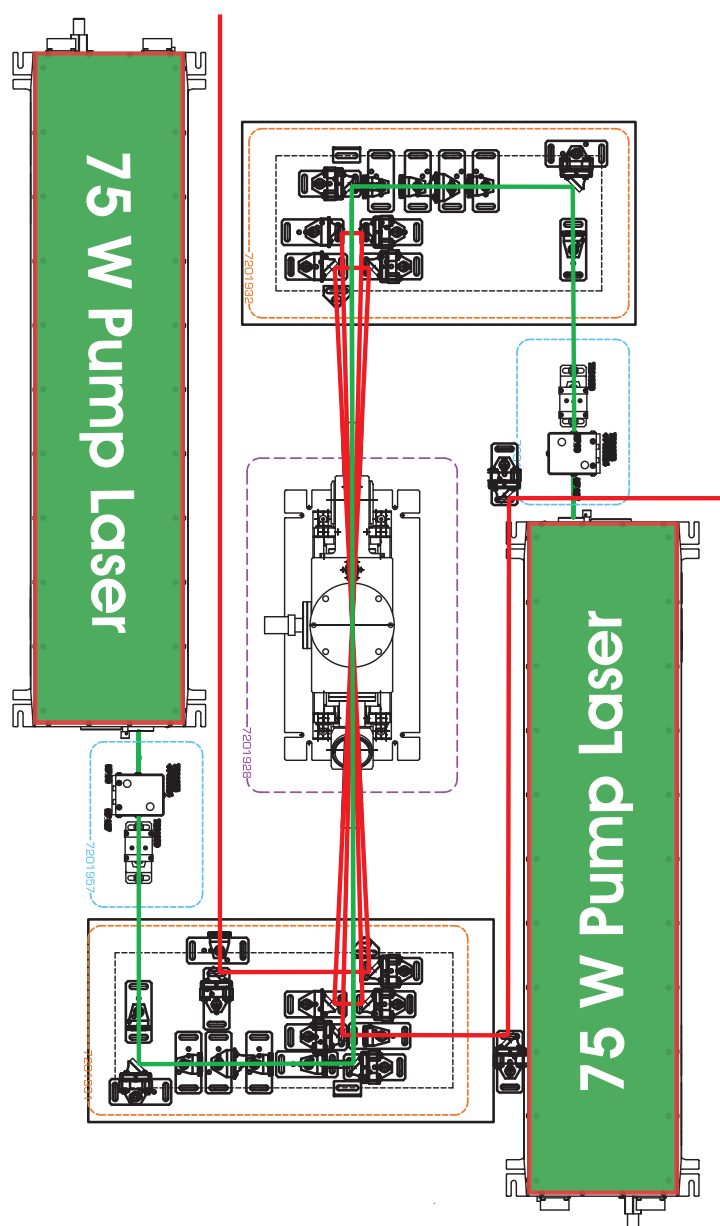


Figure A.5: Four pass cryogenically cooled multi-pass amplifier. Two ETNA HP pumps in green and the beam path of the seed in red. There is no focusing optic besides an initial lens in the optical beam-path of the seed. The thermal lens in the crystal refocuses the beam for the next pass.

New Setup of the Second Stage Amplifier

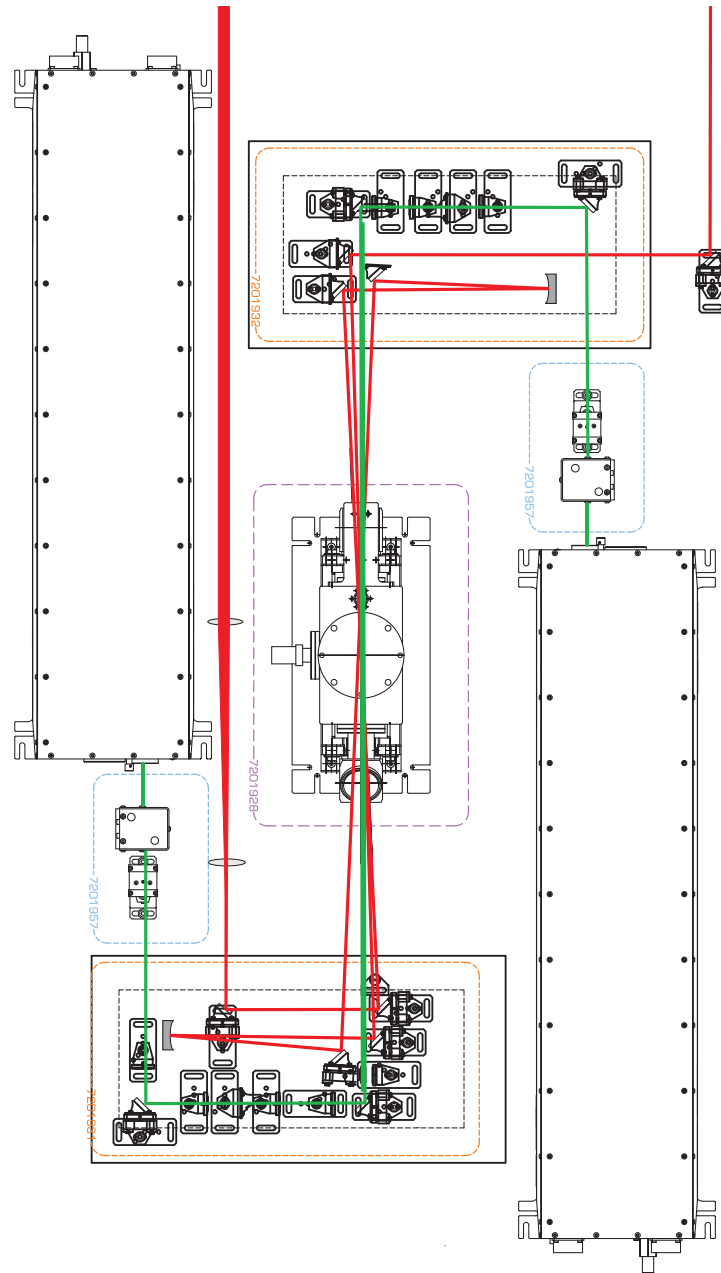


Figure A.6: Three pass setup with initial telescope and refocusing optics after the first and second pass granting much more control over the beam. As the focusing optics are placed at Rayleigh-length the behavior of the focus is often counterintuitive.

Crystal Holders of the Second stage

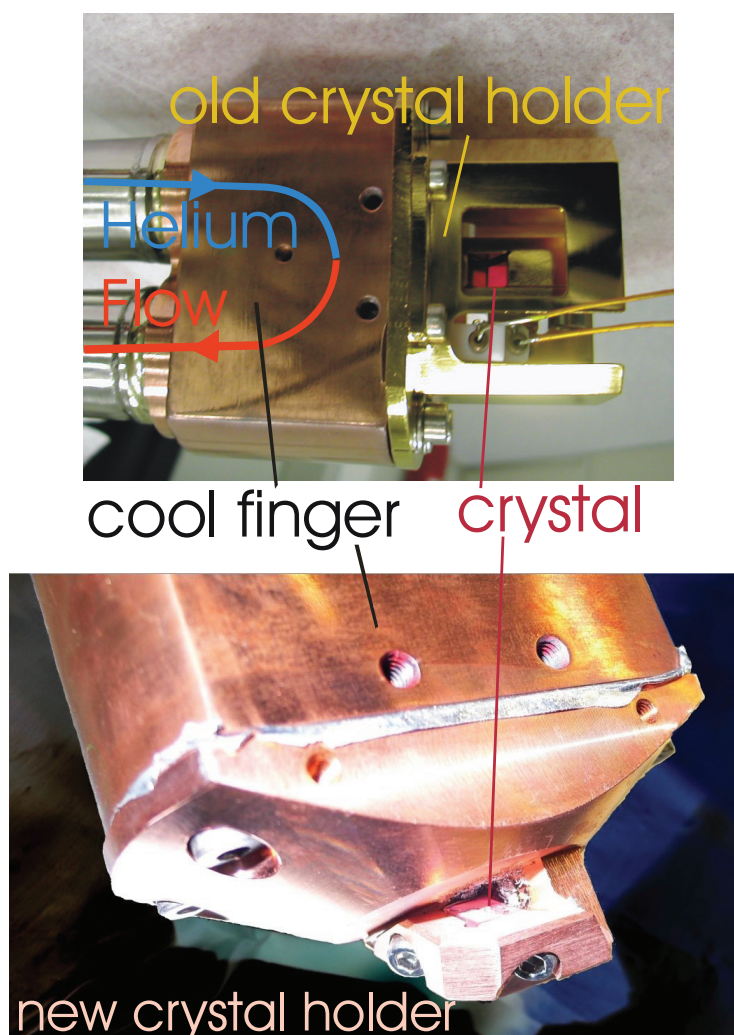


Figure A.7: On top, the first crystal holder of the second stage amplifier: The vacuum insulated helium lines are visible on the left. With a big surface on the inside of the cool finger there is efficient heat exchange between the copper and the helium. The crystal holder is on the right. The crystal itself is actually only in contact with the central part not with the cover like outer parts. The connection for the temperature measurement are also visible.

The new crystal holder is shown below. The cool finger is the same. The contact between the cool finger and the big copper piece was not ideal so we used indium foil as a gap filler similar as between the crystal and its holder. The heat transport in this configuration is not limited by the geometry of the holder but by the connection between the crystal and the holder. The crystal on this picture is damaged and the foil surrounding it re-sublimated to the holder.

Appendix B

Glass Block Data

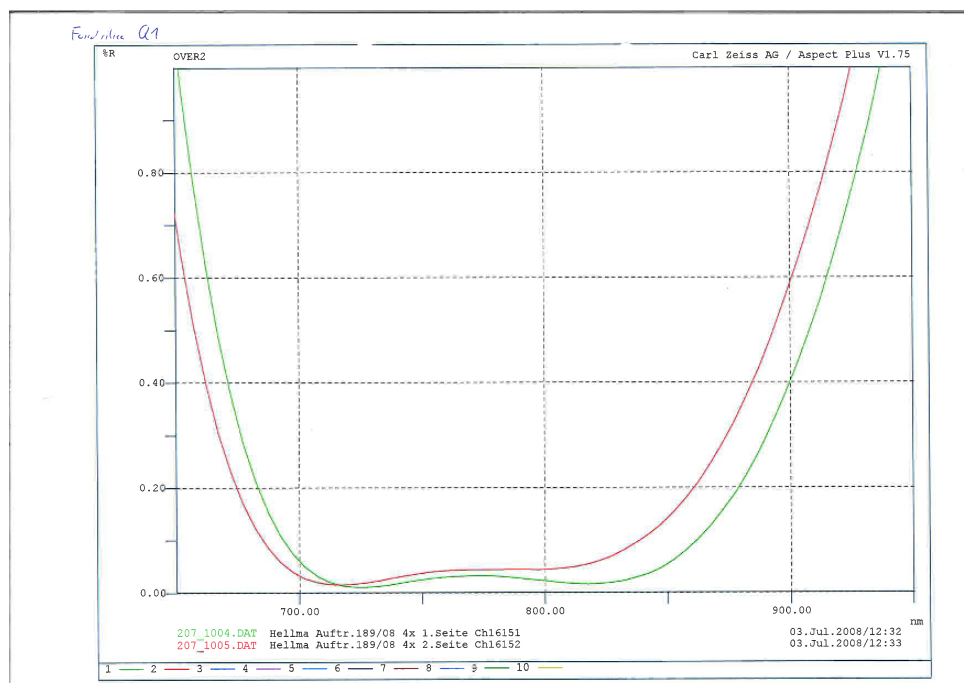


Figure B.1: AR-coating on fused silica glass block

Appendix B. Glass Block Data

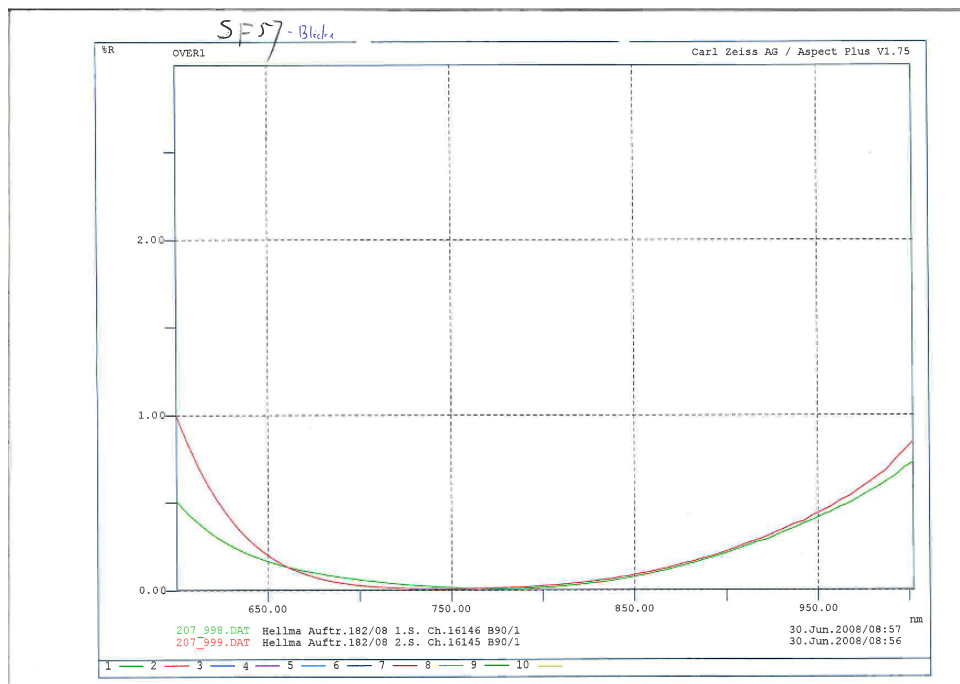


Figure B.2: AR-coating on SF57HHT glass blocks

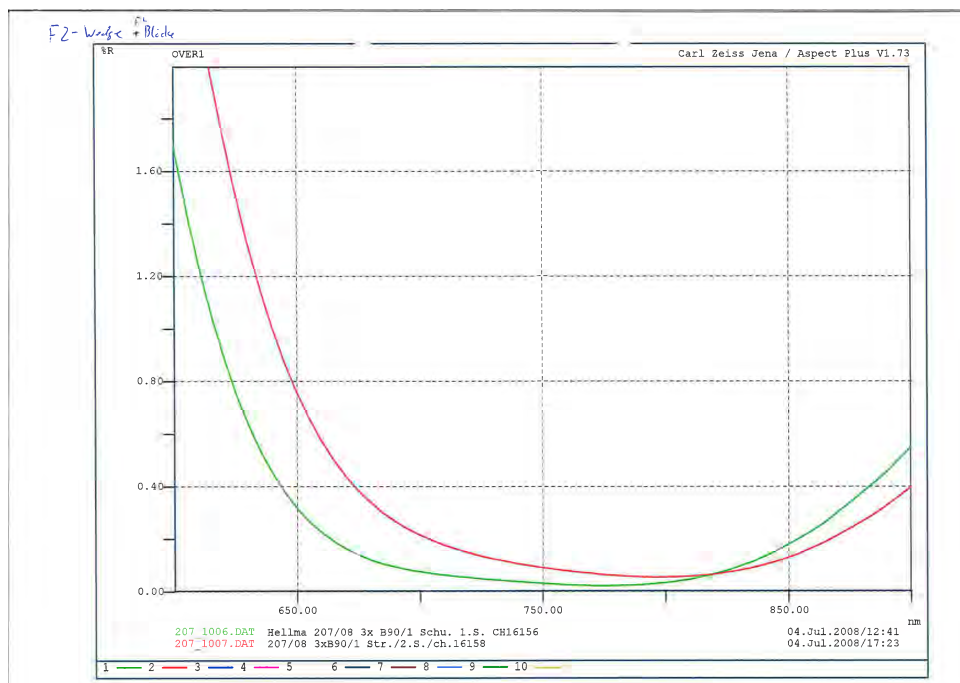


Figure B.3: AR-coating on F2 glass block

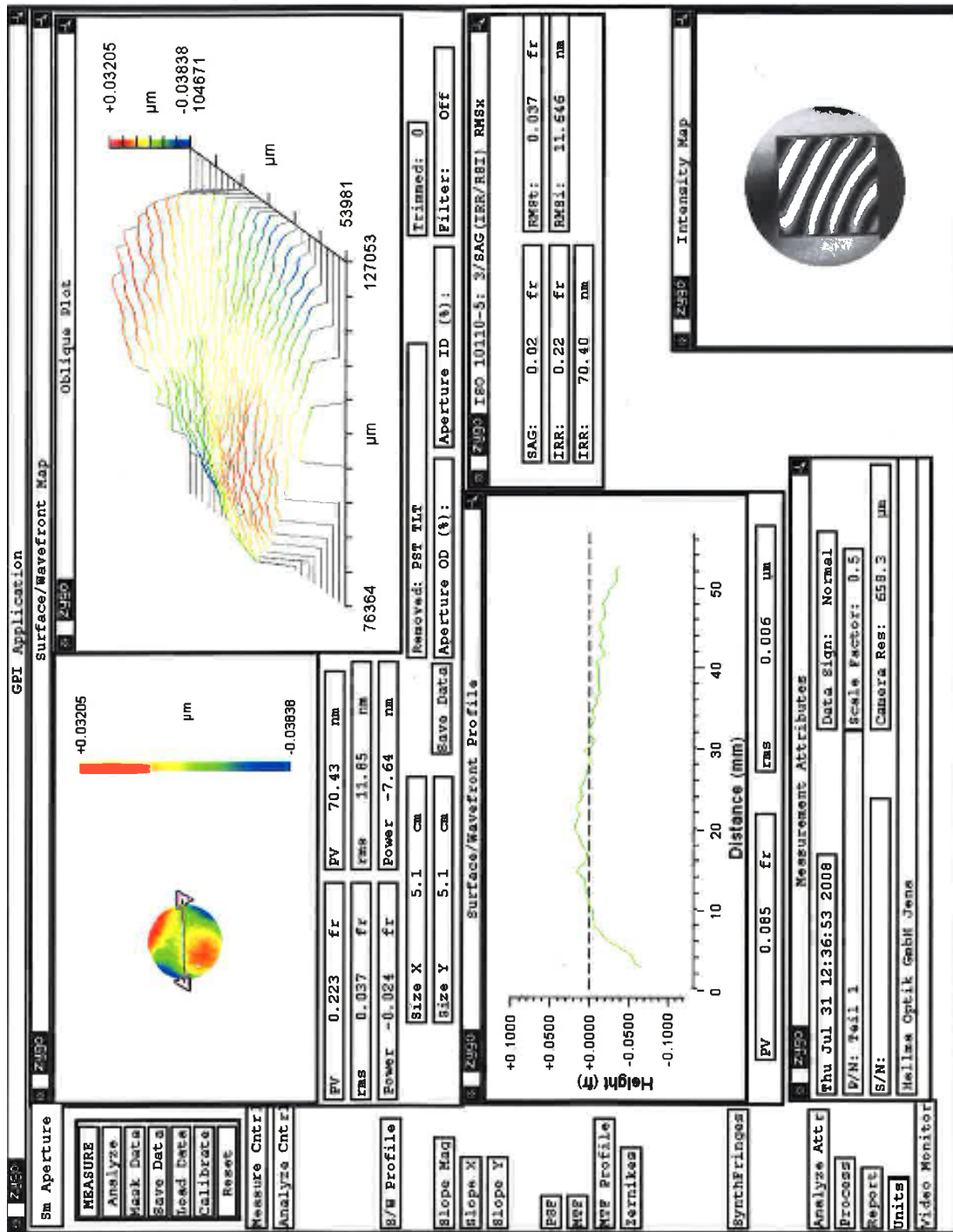


Figure B.4: Fused silica glass block surface flatness

Appendix B. Glass Block Data

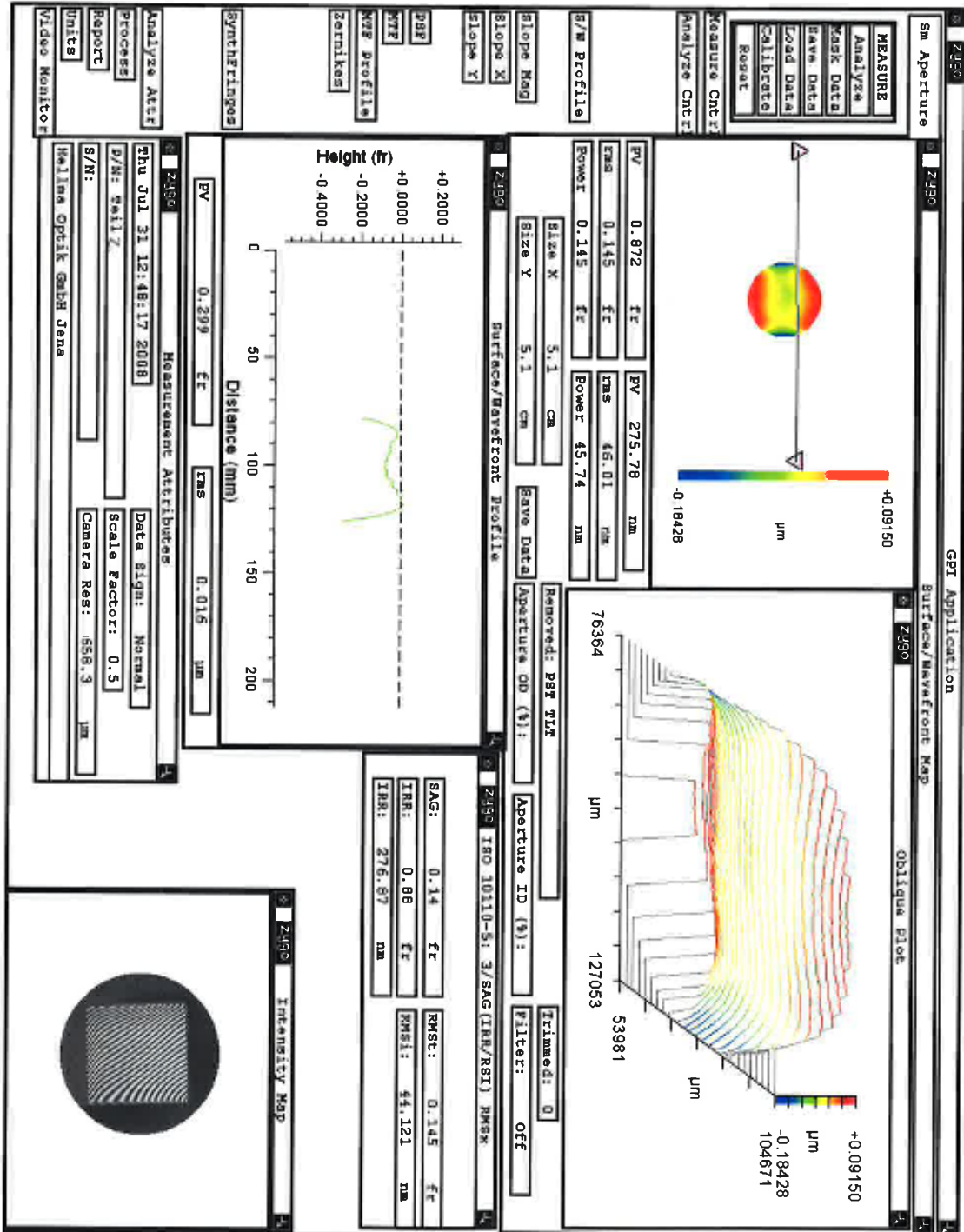


Figure B.5: SF57 glass block surface flatness

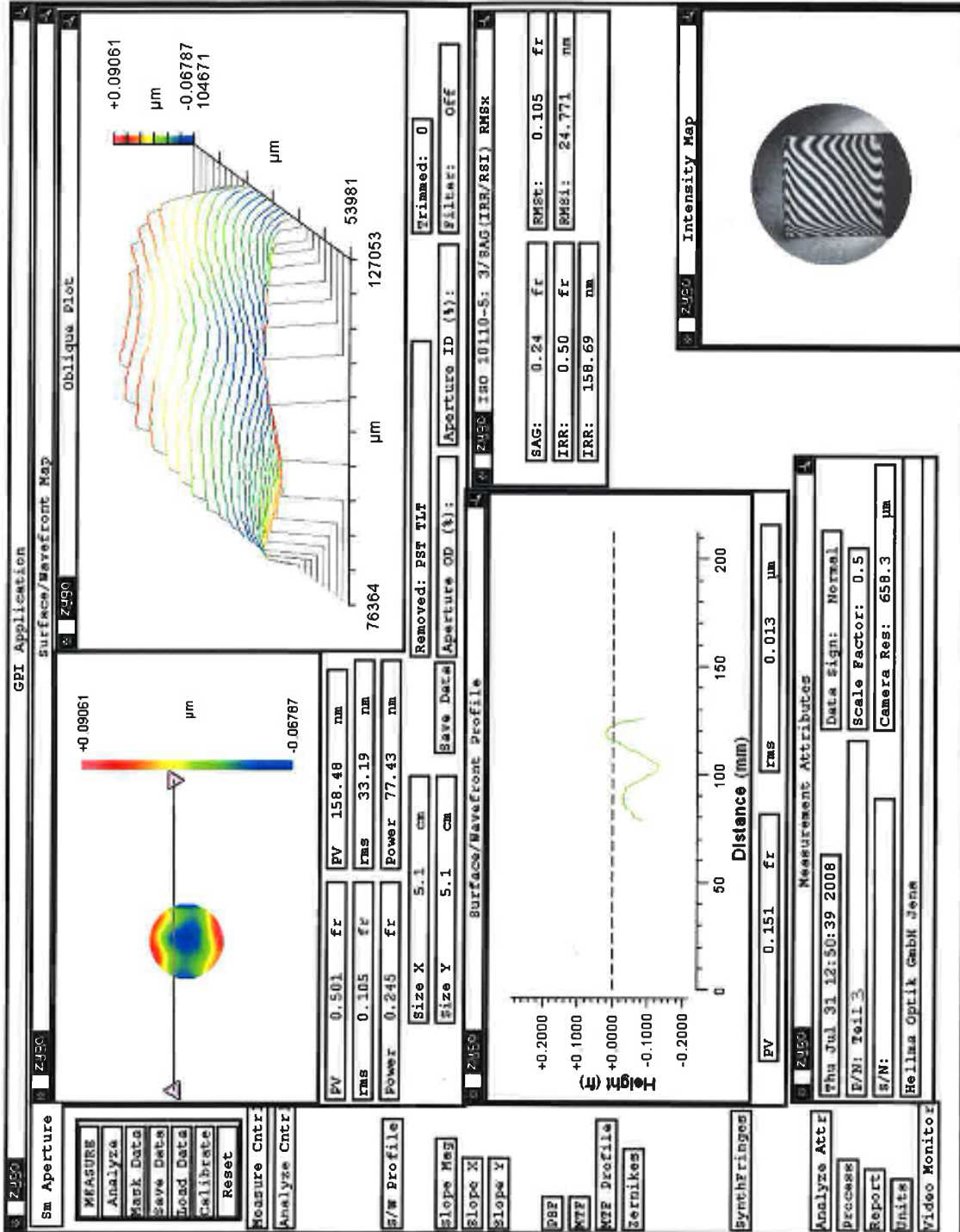


Figure B.6: SF57 glass block surface flatness

Appendix B. Glass Block Data

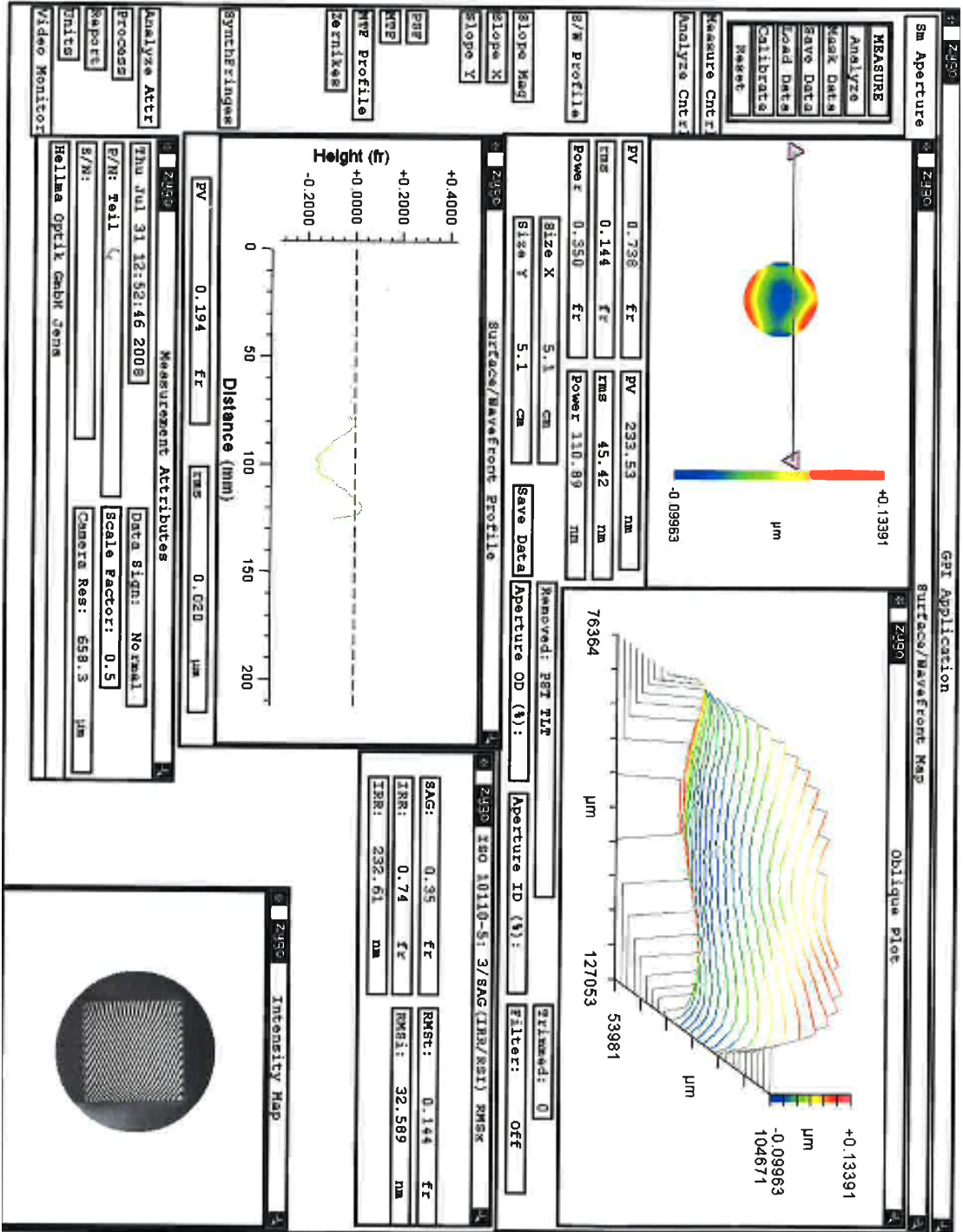


Figure B.7: SF57 glass block surface flatness

Appendix C

Dielectric Chirped Mirrors

Using intense ultrafast laser pulses makes it necessary to compress optical pulses with huge bandwidths at high intensities. Dielectric chirped mirrors have been very successful in providing the last step for the compressed pulse. Here, the two designs used with the developed laser system are presented. These two were used for experiments. A couple of other designs were tested but with unsatisfying results.

Both designs are meant to compress the dispersion of glass and air in the spectral range of 550-1050 nm (PC70 are slightly blue shifted). The design curves of the GDD and the reflectivity for both cases are shown in Fig. C.1. The most significant difference is the scale of the oscillation of the GDD which is twice as high in the case of PC70, but these are the calculated values. The reflectivity is very high, more than 99 %, for both in the supported spectrum. The big difference of the two setups is that PC5 consists of two sets of mirrors used at the same angle of incidence (AoI) of 9° whereas PC70 uses one kind of mirror only but under different AoIs (5° and 19°).

Although the design shows smaller oscillations for the PC5 setup this isn't necessarily true for the used mirrors. As the fabrication process is not always as precise as assumed in the calculation. For two coating runs these variations can go into different directions and add up resulting in much bigger oscillations. In the case of PC70 the whole run suffers the same variations which compensates some of its negative effects. This means that the realized phases for PC70 are typically closer to the design as PC5, however the optimal design is better for PC5. For two well matched runs the result for PC5 will be better. It should also be considered that making one coating run only is cheaper.

From the experimentalists point of view it is a bit easier to use the pairs (PC5) as the angle on all the optics is the same which makes it easier to change the number

Appendix C. Dielectric Chirped Mirrors

of mirrors. Some designs of double angle mirrors (like PC70) didn't result in a nice compression but seemed, according to FROG traces, have some phase distortions in the center of the spectrum. It is not certain what the cause of this is but tests concerning this feature are ongoing. Both mirrors sets compressed the pulse below 5 fs and even close or under 4 fs occasionally unfortunately it is not clear what causes this difference.

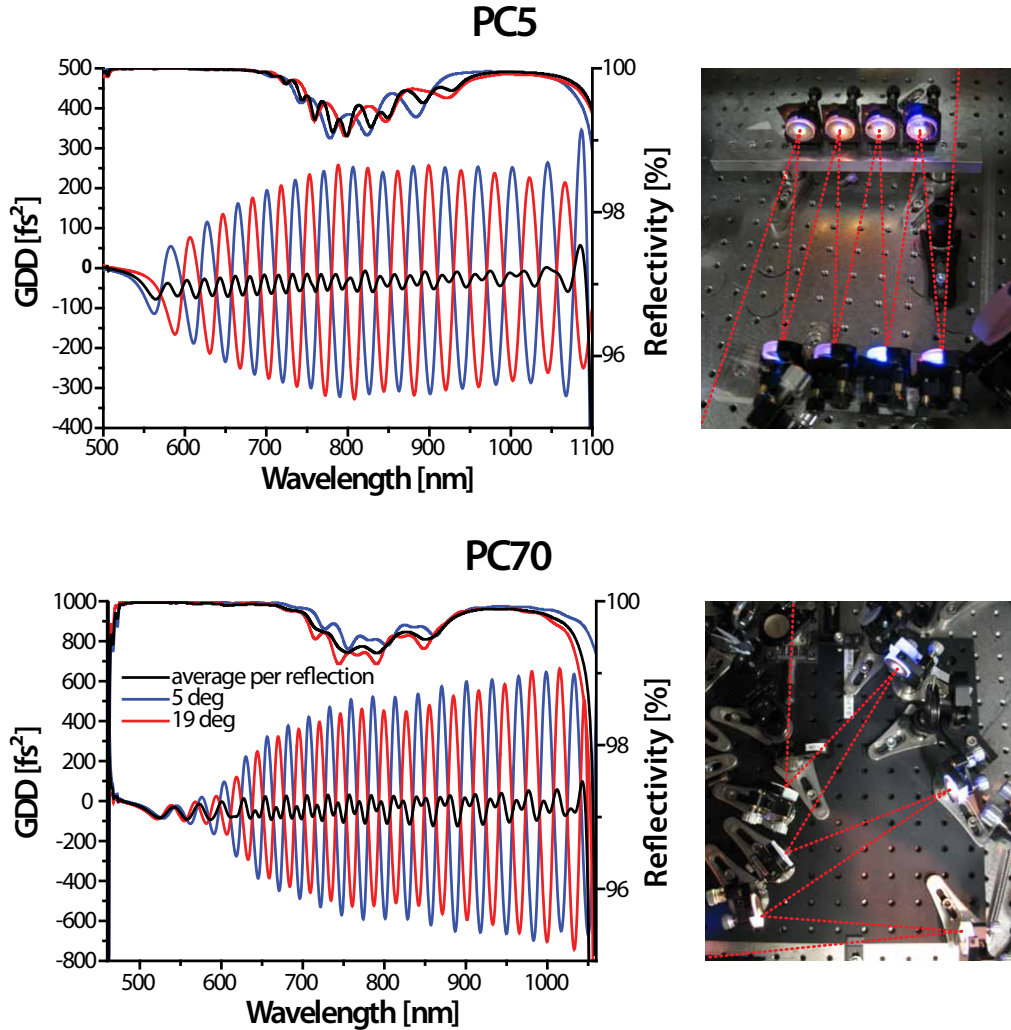


Figure C.1: Design curves of two different sets of chirped mirrors. PC5 is a complementary pair design at the AoI of 9° and PC70 is a double angle design utilizing the phase shift of different AoIs to compensate the oscillations by using just one kind of mirror. The introduced GDD per bounce is $\approx -40 \text{ fs}^2$. On the right are the physical setups of both mirror sets. For PC5 eight bounces all with the same AoI and two times three bounces for PC70 with 19° on the left and 5° on the right side.

Danksagung

Zu guter Letzt möchte ich mich noch bei Allen bedanken, die zum Gelingen dieser Arbeit beigetragen haben.

Allen voran gilt mein Dank meinem Doktorvater Professor Ferenc Krausz für seine Vision und Möglichkeit daran Teil zu nehmen. Seine Beharrlichkeit und Zuversicht haben das Projekt durch die steinigere Passagen gebracht. Die hervorragenden Bedingungen welche er im Rahmen des Instituts jungen Forschern zur Verfügung stellt können nur lobend erwähnt werden.

Mein außerordentlicher Dank gilt auch Professor Reinhard Kienberger, der zum einen mit seiner ruhigen und fröhlich gelassenen Art ein Licht außerhalb des Labors darstellt und zusätzlich noch über Jahre die Finanzierung des Projekts und die Jonglage der Budgets bewerkstelligte. Zum anderen möchte ich herzlich für die Möglichkeit bedanken bei den Experimenten am LCLS beizutragen.

Den Postdocs Adrian Cavaliere, Martin Schultze und Nick Karpowicz möchte ich für ihrer tatkräftige Unterstützung, als auch ihren Beitrag was Methodik und Wissen angeht einen herzlichen Dank aussprechen und auch für die gelegentlich notwendige Führung. Des Weiteren möchte ich mich bei allen bedanken mit denen ich im Labor, auch an anderen Projekten, zusammen arbeiten durfte: Ulrich Graf, Ivanka Grguraš, Florentin Reiter und Eleftherios Goulielmakis bei den UV-Generations-Experimenten; den anderen Laserbauern im Reinraum Alexander Schwarz, Hanieh Fattahi, Thomas Metzger, Xun Gu, Yunpei Deng, Moritz Üffing, Lazlo Veisz, Alexander Buck, Daniel Rivas; bei den Kollegen des Attosekunden beam-lines Stefan Neppel, Peter Feulner, Agustin Schiffrin und besonders bei Elisabeth Bothschafter, Annkatrin Sommer, Markus Fieß, Michael Jobst und Tobias Latka, Clemens Jakubeit und Simon Holzner; den Spiegelherstellern Vladimir Pervak, Olga Razskazovskaya, Michael Hofstetter und Alexander Guggenmos; die Teams von ATLAS und PFS haben mir auch öfters ausgeholfen und sollten auch hier kurz erwähnt sein.

Allen genannten möchte ich für das Arbeitsklima und die zumeist gute Laune trotz

nicht seltener schwieriger Umstände danken. Das gilt auch für meine noch nicht erwähnten Bürokollegen Andreas Henig, Daniel Kiefer, Antonia Popp, Antoine Moullet, Trung Luu, Manish Garg und Sabine Keiber. Ebenfalls herzlich danken möchte ich Patrick Heißler und Julia Mikhailova.

Neben dem wissenschaftlichen Personal möchte ich mich für die technische Unterstützung, bei Harald Haas, Anton Horn, Alois Böswald, Manfred Fischer und Tobias Kleinhenz bedanken. Gleiches gilt auch für alle Mitglieder der Werkstatt welche unzählige Bauteile für uns hergestellt haben allen voran natürlich die Chefs, Thomas Strobl und Michael Rogg. Für Diskussionen zum tieferen Verständnis möchte ich neben Prof. Krausz und Nick Karpowicz insbesondere Vladislav Yakovlev danken, der mir bei den Simulationen zu Xenon sehr unter die Arme gegriffen hat.

Ganz am Schluss möchte ich mich auch noch, für die Unterstützung der eigenen Familie bedanken.